

STELLINGEN

behorend bij het proefschrift

Measurement and modeling of cluster formation

Michiel van Drunen

1. Homogene nucleatie in oplossingen is op dit moment niet direct experimenteel te volgen, omdat de kritische clusters te klein zijn en hun concentratie te laag.
2. Clusters in veel geconcentreerde oplossingen zijn geen voorstadia van kristallen. Daarom zijn kristallisatietheorieën met kristalparameters zoals grensvlakenergie en oplosbaarheid, ongeschikt om clustereigenschappen te beschrijven.
3. Optische vezels hebben het werkkerrein van fotoncorrelatiespectroscopie sterk verbreed, maar de bewering van Ricka (*Applied Optics* 32 (1993) 2860) dat bij het gebruik van een single-mode optische-vezeldetector een hogere signaal-ruisverhouding resulteert terwijl de signaalsterkte blijft, is onjuist.
4. Door de 'juiste' data-analysemethode te kiezen kan een onderzoeker vrijwel elke gewenste deeltjesgrootteverdeling krijgen uit zijn ruwe PCS-data. Daarom moet in publikaties met PCS-resultaten altijd de data-analysemethode worden vermeld.
5. Het vak *Chemie en Samenleving* zou overbodig moeten zijn, omdat het bedrijven van wetenschap en technologie bij uitstek een maatschappelijke bezigheid is.
6. De meeste mensen, inclusief wetenschappers, denken dat verworvenheden van wetenschap en technologie waardenvrij zijn en dat de samenleving de keuze heeft deze verworvenheden te implementeren. Beide gedachten berusten op een misvatting.
7. Het overmatig gebruik van Engelse woorden in het Nederlands getuigt van een gebrek aan creativiteit en een minachting voor de Nederlandse taal en cultuur.
8. Steeds meer instanties en bedrijven zeggen duurzame ontwikkeling na te streven onder verwijzing naar *Our common future* van de commissie-Brundtland. Helaas bedoelen ze hiermee veelal hun *eigen* ontwikkeling, terwijl de commissie Brundtland toch vooral dacht aan een grotere welvaart voor ontwikkelingslanden. Met duurzaamheid bedoelde ze ook niet dat een situatie moest blijven voortduren.
9. Kringlooppapier heeft het imago dat het inferieur is, maar dit proefschrift bewijst dat het voor veel toepassingen uitstekend voldoet.
10. Door moderne selectiemethoden denken multinationals een slagvaardige en flexibele organisatie te creëren. Maar doordat zij selecteren op een specifiek type manager, zijn zij juist kwetsbaar als externe omstandigheden veranderen. (Zie ook Charles Darwin (1859) *On the origin of species by means of natural selection or the preservation of favoured races in the struggle for life*)
11. Hockeyers staan niet bekend als bijzonder progressief. Maar in hun sport zijn ze dit wel degelijk: in tegenstelling tot voetballers zijn ze niet bang om spelregels te wijzigen of nieuwe materialen toe te passen.

642181

3190591

TR diss 2705

**TR diss
2705**

Measurement and modeling of cluster formation

Het meten en modelleren van clustervorming

Michiel van Drunen

Measurement and modeling of cluster formation

Het meten en modelleren van clustervorming

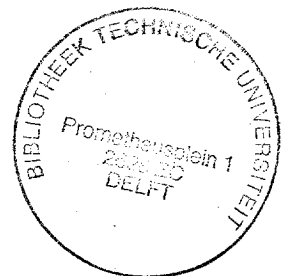
PROEFSCHRIFT

ter verkrijging van de graad van doctor
aan de Technische Universiteit Delft,
op gezag van de Rector Magnificus Prof. ir. K.F. Wakker,
in het openbaar te verdedigen ten overstaan van een commissie,
door het College van Dekanen aangewezen,
op dinsdag 16 januari 1996 te 16.00 uur
door

Michiel Adriaan VAN DRUNEN

doctorandus in de scheikunde

geboren te Zwijndrecht



Dit proefschrift is goedgekeurd door de promotoren:

Prof. B. Scarlett M.Sc.
Prof. dr. ir. G.M. van Rosmalen

Samenstelling promotiecommissie:

Rector Magnificus, Voorzitter
Prof. B. Scarlett M.Sc., Technische Universiteit Delft, promotor
Prof. dr. ir. G.M. van Rosmalen, Technische Universiteit Delft, promotor
Drs. H.G. Merkus, Technische Universiteit Delft
Prof. dr. R. Finsy, Vrije Universiteit Brussel, België
Prof. dr. G. Fréns, Technische Universiteit Delft
Prof. dr. R. Louw, Rijksuniversiteit Leiden
Dr. ir. A.A. van Well, Technische Universiteit Delft
Prof. ir. J. Grievink, Technische Universiteit Delft, reservelid

CIP-DATA KONINKLIJKE BIBLOTHEEK, DEN HAAG

Van Drunen, Michiel Adriaan
Measurement and modeling of cluster formation / Michiel van Drunen
Thesis Delft University of Technology. - With ref. - With summary in Dutch
ISBN 90-9009059-2

NUGI 813

Subject headings: crystallization / particle characterization / light scattering /
photon correlation spectroscopy

Parts of this material are allowed to be reproduced or utilized as long as their
source is mentioned.

All the modern things
like cars and such
have always existed.

They have just been waiting in a mountain
for the right moment.

Listening to the irritating noises
of dinosaurs and people
dabbling outside.

All the modern things
like cars and such
They have just been waiting

To come out
and multiply
and take over.

Björk Gmundsdottir
The modern things (Post - 1995)

Voor mijn ouders

Omslagfoto: 'Ontkieming' door Jan Remmert Fröling

Dit proefschrift is opgemaakt met Word 2.0 voor Windows. De illustraties zijn, met uitzondering van de foto's, gemaakt met CorelDraw! 4, Excel 5.0 voor Windows en ChemWindow 1.35. De vergelijkingen zijn getypt met de Microsoft Equation Editor 2.0. Het gebruikte lettertype is New Century Schoolbook.

Het is gedrukt bij CopyPrint 2000 in Enschede op Nautilus kringlooppapier.

Het werk dat is beschreven in dit proefschrift is mogelijk gemaakt door financiering uit het fonds van de Stimuleringsruimte ('Commissie Beek') van de Technische Universiteit Delft.

Contents

Summary	xii
1. General introduction	
1.1 Cluster formation and nucleation	1
Nucleation	1
Thesis goal	2
1.2 Measurement techniques	2
Fluctuations	3
1.3 Scope of this thesis	4
References	5
2. Nucleation from solution	
Abstract	7
2.1 Introduction	7
2.2 Thermodynamics	9
2.2.1 Basics	9
2.2.2 Free energy change for cluster formation	10
Nucleation of a homogeneous droplet	11
Formation of a homogeneous crystal	11
Crystal growth: a disk on a substrate of the same composition	12
2.2.3 Thermodynamics involved in formation of critical clusters	12
Assumptions in the classical thermodynamic theory	14
2.3 Kinetics	14
2.3.1 The steady state approach	14
2.3.2 The real cluster size distribution	15
2.3.3 Steady state - detailed balance	17
2.3.4 The kinetic approach	18
2.3.5 Simplified expressions for the nucleation rate	21
2.4 Heterogeneous nucleation	22
Effect on energetics	23
Effect on pre-exponential factor C_0	24
Effect on kinetics	24
Total effect of heterogeneous nucleation	24
2.5 Example: calculation of the nucleation rate	24
2.6 Conclusions	27
References	27
3. Particle size determination by photon correlation spectroscopy	
Abstract	29
3.1 Introduction	29
3.2 Physical background	30
3.3 Analysis of the autocorrelation function	34
3.3.1 Cumulants	34
3.3.2 Contin	35
3.4 The average particle size	36
3.5 PCS measurements of aerosols	37
3.6 Conclusions	38

viii Measurement and modeling of cluster formation

Appendix	40
3.A Optics and coherence areas	40
3.B The autocorrelation procedure	41
References	42
4. Cluster formation in concentrated solutions	
Abstract	45
4.1 Introduction	45
Earlier work	45
Neutron scattering	46
Sucrose and potassium nitrate	46
Scope	47
4.2 Theory	47
4.2.1 Theory of cluster formation	47
4.2.2 PCS in concentrated systems	49
4.2.3 Neutron scattering	49
4.3 Materials and methods	50
4.3.1 PCS-experiments	50
Citric acid	50
Sucrose and potassium nitrate	51
4.3.2 Neutron diffraction	51
4.4 Results and discussion	52
4.4.1 PCS measurements in citric acid	52
Volume fraction	54
Interactions	55
Cluster size	55
4.4.2 PCS measurements in sucrose and potassium nitrate solutions	57
Sucrose	57
Potassium nitrate	59
4.4.3 Neutron diffraction of deuterated citric acid solutions	59
4.5 Conclusions	60
Appendix	63
4.A Correction sample attenuation and self shielding	63
References	66
5. Gas to particle conversion. Homogeneous nucleation and coagulation	
Abstract	67
5.1 Introduction	67
Ceramics	67
Growth by coagulation	68
PCS and aerosols	68
5.2 Theory	69
5.2.1 Particle diffusion in gases	69
5.2.2 Coagulation of silicon nitride particles	70
5.3 Experimental	73
5.3.1 The setup	73
5.3.2 The measuring system	74
5.3.3 Modeling	76
5.4 Results and discussion	77

5.5 Conclusions	79
References	80
6. In-line measurements of monodisperse sulfur sol formation	
Abstract	83
6.1 Introduction	83
6.2 Theory	84
6.2.1 Sulfur precipitation	84
Reactions	85
6.2.2 Mie profiles of single sulfur particles	86
6.3 Experimental	86
6.4 Results and discussion	87
Concentration profiles	88
6.5 Conclusions	93
6.A Appendix	94
References	95
7. Barium sulfate precipitation: Crystallization kinetics and the role of the additive PMA-PVS	
Abstract	97
7.1 Introduction	97
PCS and conductivity	98
Model	98
Aim	98
7.2 Theory	98
7.2.1 Photon correlation spectroscopy	98
7.2.2 Electric conductivity in ionic solutions	99
7.2.3 Precipitation from solution	100
7.2.4 Effect of PMA-PVS on crystallization kinetics	101
7.2.5 The population balance equation	102
7.2.6 The forward approach	103
7.3 Experimental	103
7.3.1 Precipitation experiments	103
7.3.2 Modeling of the population balance	105
7.4 Results	105
7.5 Discussion	108
7.6 Conventional analysis methods	112
7.7 Conclusions	113
References	114
Symbol list	115
Samenvatting	119
Nawoord	123
Curriculum vitae	125

Summary

Measurement and modeling of cluster formation

Michiel van Drunen

Introduction

Crystallization, the transition from a melt or a dissolved phase into a solid crystalline phase is an important unit operation in industry, e.g. for purification or for manipulating the crystal size distribution (CSD). Many products, such as silver halides used for photographic materials, are crystallized or precipitated from solution. For most products, the CSD must satisfy narrow specifications.

Crystallization is generally a two step process. In the first step, nuclei are formed and in the second step the crystal growth takes place. Hence, before crystal growth can occur, nuclei must be formed.

The main goal of the work described in this thesis is to follow experimentally the nucleation phenomena, preferably on-line. The data thus obtained can be useful for two reasons. The first is to obtain a better insight in the nucleation process itself. The second reason is that measurements of nucleation phenomena in actual processes can improve the control of the crystal size distribution.

Nucleation theory

Chapter 2 of this thesis outlines the theory of nucleation from solution. It starts with an introduction of the basic physics of nucleation phenomena. The focus of the chapter concerns the kinetics of nucleation. Because of its complexity some assumptions must be made in order to derive an equation for the nucleation rate and the cluster size distribution. Three theories are compared, *the detailed balance theory, the purely kinetic theory, and the simplified equation.*

From classical thermodynamics, it is possible to obtain the equilibrium cluster size distribution as a function of supersaturation. The detailed balance theory considers a semi-equilibrium and by using the principle of steady state, the real cluster size distribution is expressed in terms of the equilibrium cluster size distribution and the forward reaction rate.

The purely kinetic theory uses a kinetic argument to obtain expressions for the nucleation rate and cluster size distribution. Thus, at equilibrium the backward reaction rate equals the forward reaction rate.

The semi-empirical equation is a simplification of the detailed balance theory. It uses the equilibrium cluster size distribution instead of the real distribution.

At the end of this chapter results of model calculations on nucleation rates in barium sulfate solutions are given. Apart from the value of the interfacial energy, the homogeneous nucleation rates predicted by the different theories coincide quite well.

Measurements

Since the experimental section of this thesis largely relies on one particle size analysis technique, namely photon correlation spectroscopy (PCS), the third chapter is entirely devoted to a discussion of its background and of its strengths and weaknesses. PCS measures the fluctuations of scattered laser light from an assembly of dispersed particles undergoing Brownian motion. By quantifying these intensity

xii Measurement and modeling of cluster formation

fluctuations in diluted liquid dispersions of narrowly distributed, non-interacting spherical particles, their diffusion coefficient can be determined. In such cases the diffusion coefficient can be used to accurately calculate the average of the intensity weighted hydrodynamic particle diameter.

In all other cases several precautions must be taken in order to obtain reliable information about the particle size distribution. It must be stressed that, without prior knowledge of the sample, only a limited amount of information, roughly two information units (e.g. average size and variance of the size distribution), can be extracted from the measured autocorrelation function.

Cluster formation in highly concentrated solutions

The fourth chapter describes investigations by means of photon correlation spectroscopy of aqueous solutions of citric acid, potassium nitrate and sucrose at high volume fractions and low supersaturation or at undersaturation. The formation of small clusters of molecules or ions is the subject, rather than nucleation. From the time dependence of the scattered light the collective diffusion coefficient was obtained. Interactions between the solute molecules result in a concentration dependence of the diffusion coefficients. From this, the attractive interaction parameter has been estimated. It appears that strong attractive forces between the molecules play a dominant role in the solutions of sucrose and citric acid. Even below the saturation concentration, clusters of 2-3 molecules develop. This is much smaller than the critical cluster size of crystalline sucrose and citric acid. The clusters are presumed to be aggregates of solute molecules which are not precursors of the crystalline compounds, but form a different phase. Alternatively, solute molecules might be forced into small clusters by surrounding water molecules. Potassium nitrate appears not to form clusters, since the diffusion coefficient does not change significantly as a function of concentration.

Neutron diffraction experiments of deuterated citric acid in heavy water give qualitative support for the formation of clusters in solution. The intensity spectrum shows a 'shoulder' at short q -values. This is attributed to larger scattering units which can be clusters.

Homogeneous nucleation

In the rest of the thesis attention moves away from a molecular description of cluster formation and nucleation. Kinetics now plays a dominant role. Chapter 5 discusses homogeneous nucleation from the gas phase. The supersaturation is very high whilst the concentration of reactants is relatively low. Aerosols with a sufficiently high particle concentration in flames can be monitored by photon correlation spectroscopy (PCS). In this study the growth of silicon nitride particles in an aerosol reactor was monitored using this method. The particles are formed by heating silane and ammonia in a strong infrared laser beam. A flame results in which the particles grow mainly by coagulation. Thus, a coagulation model is used to predict the development of the particles in the flame. A single mode optical fiber in combination with a polarization filter and an interference filter significantly reduced the strong background light from the flame.

The silicon nitride particles grow in less than 1 ms from 30 to 240 nm. The characteristic sintering time was found from matching the coagulation model to the experimental results. It is $3 \cdot 10^{-12} T d_p^3 \exp(53.65/T)$ ($\pm 20\%$) [s], where T is the temperature [K] and d_p the primary particle diameter [nm].

Chapter 6 deals with homogeneous nucleation from solution. The supersaturation was very high and the concentration of the reactants very low. The system was the formation of a monodisperse sulfur sol by chemical reaction, i.e. by acidifying thio-sulfate solutions. The rate of sol formation is determined by the reaction rate of the sulfur formation and not by nucleation or by growth. The experiments were performed as a pilot study for PCS measurements of crystallization from solution. It is shown that the particle growth can be followed in-line and with reasonable precision, and that information on the particle number concentration can be obtained as long as the size distribution is narrow. The growth rate obtained from the measurements, $d[S]/dt = 0.44 [H^+]_0 [S_2O_3^{2-}]_0^2$ [mol l⁻¹s⁻¹], resembled the one mentioned in the literature.

Contrary to the literature data, the induction time, which is defined as a period in which nothing can be measured by PCS, was found to be several hundreds of seconds. This was expected since in this work only colloidal particles were measured, whereas in literature all of the sulfur molecules were monitored, dissolved or not. In the induction stage, the molecularly dissolved sulfur is expected to be formed.

Heterogeneous nucleation

Barium sulfate has a low solubility and a very high specific interfacial energy. Therefore, at the relatively low supersaturation of 24.5, nucleation takes place exclusively heterogeneously. Precipitation of barium sulfate was investigated and reported in chapter 7 by photon correlation spectroscopy (PCS) measurements of the growing crystals combined with electrical conductivity measurements of the mother solution.

In order to avoid the ill-conditioned inversion of the raw measured data, that is the autocorrelation functions, a population balance model was used to calculate these functions with the help of a kinetic model taken from literature. The measured and the calculated autocorrelation functions should coincide and adjustable parameters were found from a least square fit. Thus, the model acted as an *observer* for the precipitation process.

The measurements revealed that nucleation is strongly enhanced by PMA-PVS (polymaleic acid - polyvinyl sulfonic acid). Thus, more crystals are formed, resulting in a smaller average crystal size of the end product. But once the crystals are formed, their growth rate is retarded. The mechanism for this is adsorption of the polymer molecules on the crystal surface. However, a simple model which assumes Langmuir adsorption did not describe the kinetics very well.

From the measured data, the nucleation rate was found to be, $J = 1.3 \cdot 10^{10} \exp(-27 / \ln^2 S)$ [m⁻³s⁻¹], while the growth rate was $G = 2.6 \cdot 10^{-8} (S-1)^{2/3} S^{1/3} \exp(-29 / 3 \ln S)$ [m s⁻¹]. These results match the literature results quite well.

General introduction

1.1 Cluster formation and nucleation

First order phase transitions belong to nature's least understood and most interesting phenomena. Crystallization, the transition from a melt or a dissolved phase into a solid crystalline phase is an important process in a wide range of scientific disciplines including chemistry, physics, biology, geology and materials science. In addition, it is an important unit operation in industry, which is used for purification or for manipulating the crystal size distribution (CSD) of a product. Many products, such as silver halides used for photographic materials, are directly crystallized from solution. Other products which are synthesized or purified by crystallization processes are base materials such as sucrose, sodium chloride, fertilizers and specialties such as pharmaceuticals, pigments and catalysts.

Usually, the crystal size distribution must satisfy narrow specifications. Thus, fertilizer crystals must be small enough to be able to spread them over the land, but they must not be too small because then they are dusty. On the other hand, crystals used in photographic materials must be very small in order to obtain high resolution.

Nucleation

Crystallization is generally a two step process. In the first step, nuclei are formed. The nucleation rate is usually given in terms of number of nuclei per volume per time unit. In the second step the crystal growth takes place. The growth rate is usually characterized in length units per time unit. Hence, before crystal growth can take place, nuclei must have been formed. Therefore, if two experiments have the same initial conditions except for the nucleation rate, the one with the highest nucleation rate will produce more but smaller crystals.

The study of nucleation kinetics has been mainly the domain of chemical engineers, because they were confronted with considerable losses if they did not deliver crystalline products within narrow size specifications. However, more and more attention is currently given to this subject by (bio-)organic chemists, for example, who try to investigate interfacial processes on a molecular scale (Mann et al. 1993) and some authors have successfully combined kinetic and molecular theories to understand nucleation phenomena (e.g. Van der Leeden 1991).

The kinetic theory of nucleation was already formulated between 1926 and 1949 and since then only minor improvements have been suggested (Baraké 1994). At least two types of nucleation can be distinguished: homogeneous and heterogeneous. The first type is nucleation directly from the fluid phase and is associated with high levels of supersaturation, whereas the latter is nucleation on foreign surfaces. In this thesis, both types will be encountered.

Nature is very good at controlling nucleation processes. Organic molecules, e.g. proteins, are capable of influencing interfacial properties, resulting in well defined complex structures such as bones, shells and teeth. Some fish are capable of surviving enclosure in ice because biological inhibitors kinetically prevent ice crystal

2 Measurement and modeling of cluster formation

formation in their tissues (Mann et al. 1993). In order to make crystals with a well defined morphology and size distribution on an industrial scale, attempts have been made to design additives which affect crystal nucleation and growth. Van der Leeden (1991) demonstrated the effects of poly-electrolytes on the precipitation of barium sulfate.

Thesis goal

The main goal of the work described in this thesis is to follow experimentally nucleation phenomena from solutions, preferably in-line or on-line (fig. 1.1). The data thus obtained can be useful for two reasons. The first is to obtain a better insight in the nucleation process itself. Here, not only the reaction kinetics are important, but also the molecular process of cluster formation. The second reason is that measurements of nucleation phenomena in actual chemical processes can improve the operating conditions which control the crystal size distribution. Since measuring techniques play a dominant role in this, they will be discussed briefly in the next section.

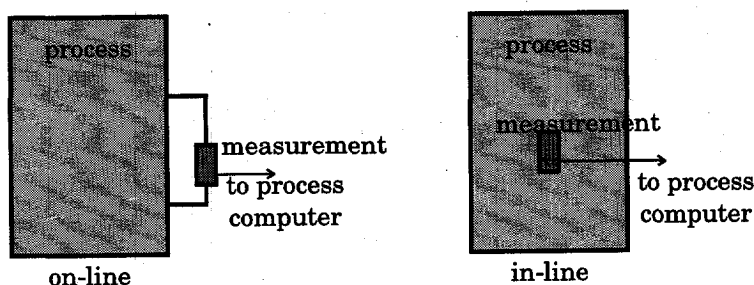


Fig. 1.1. On-line measurements take place by extracting a small fraction of the contents, making a measurement and feeding the sample back. In-line measurements are made directly in the process vessel.

1.2 Measurement techniques

For measuring submicrometer particles, where particles can be clusters, very small crystals or macromolecules, several techniques are available. The difference between clusters and crystals is that crystals exceed the critical cluster size and clusters do not, i.e. thermodynamically, crystals are stable. This will be further explained in chapter 2. Since the particle size is of the order of the wavelength of visible light (0.4-0.7 μm), or even smaller, normal light microscopes are unsuitable for submicrometer particles. However, by using electrons with a much smaller wavelength than visible light, it is possible to investigate these particles. The main drawback of electron microscopy is that sample preparation is rather elaborate and that the measurements must take place in vacuum. Thus, for on-line measurements, electron microscopy cannot be used.

Static light scattering methods are very well suited to perform on-line measurements, as has been shown in the Delft laboratory by Boxman (1992), Heffels (1995) and Eek (1995). However, for measurements of submicrometer particles, static light scattering cannot be used because particles smaller than the wavelength of the scattered light, have almost the same angular scattered intensity pattern (fig. 1.2). To overcome this, radiation with shorter wavelengths can be used such as X-rays or thermal neutrons. Unfortunately, it is not a trivial problem to generate such waves

under normal laboratory or industrial conditions because complicated or potentially dangerous devices are needed. For example, for generating neutrons a nuclear reactor is required.

Fluctuations

In this thesis, therefore, most of the measurements have been performed by dynamic light scattering. With this technique, it is not the *angular* pattern of the light scattered by an assembly of particles which is probed, but rather the *fluctuations* of the intensity in *time* at a certain angle (fig 1.2).

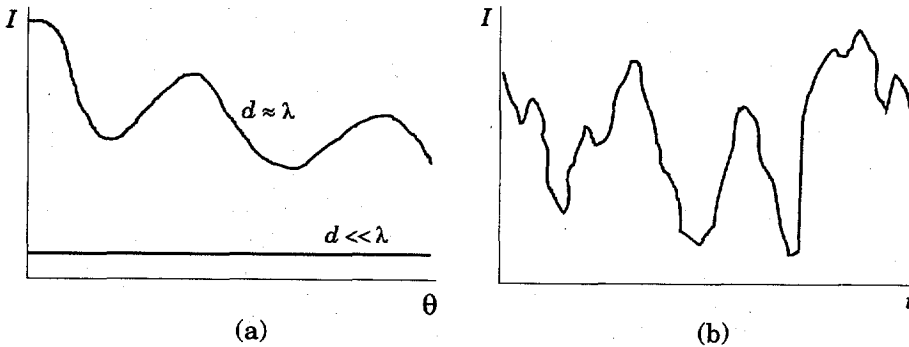


Fig 1.2. For particles with a diameter much smaller than the wavelength, the scattered light intensity I is independent of the scattering angle θ (a). Thus, for these particles, the time dependence (b) of the scattered light is monitored.

Nowadays these fluctuations, which are caused by the Brownian motion of the particles investigated, are quantified with a mathematical procedure called autocorrelation, the technique is therefore often referred to as Photon Correlation Spectroscopy (PCS).

The technique of dynamic light scattering was developed thirty years ago in the laboratory of H.Z. Cummins and co-workers (Weiner 1992, Cummins et al. 1964). Among the subjects studied in the early years were mobile micro organisms and sperm cells. Because dead cells are subjected to Brownian motion and the living cells move by themselves, the percentage of living organisms or the fertility could be estimated from the dynamic light scattering signal.

Originally, only highly diluted samples could be probed with PCS because the theory is based on single scattering, i.e. every photon is scattered by only one particle before it reaches the detector. But the development of extremely thin (several μm) optical fibers and optical fiber couplers make it possible to measure also in concentrated dispersions as well (Finsy 1994, Wiese and Horn 1991, Dhadwal and Chu 1990).

However, nucleation usually takes place at low particle concentrations and, therefore, only the conventional type of measurements which can only be performed in samples with a low scattering intensity, are described in this thesis. In addition to the data obtained by PCS, information on the systems investigated has been gathered by neutron scattering and scanning electron microscopy.

1.3 Scope of this thesis

This thesis can be subdivided in four parts. The first part consists of chapters 2 and 3. They discuss the theories of nucleation (chapter 2) and of photon correlation spectroscopy (chapter 3), which are both used extensively in the following chapters. In *chapter 2* it is explained that clusters develop in solutions. These clusters can grow into critical clusters which are also referred to as nuclei if they reach a certain size. If the clusters reach this size they will not redissolve at the prevailing supersaturation. The nucleation rate is the number of clusters which reach this size per volume per unit time. In an example three theories are discussed and compared.

Chapter 3 discusses the theoretical background of photon correlation spectroscopy, the measuring technique which is used most in the following chapters. PCS indirectly probes the diffusion coefficient of the sample particles which, for monodisperse and very dilute samples, can be converted into the particle size. In all other cases, additional information about the sample properties is required. Nevertheless, PCS is a fast technique which is suited for on-line and even in-line measurements if it is customized for the purpose for which it is used.

This is shown in the following three parts of this thesis which are schematically drawn in fig. 1.3.

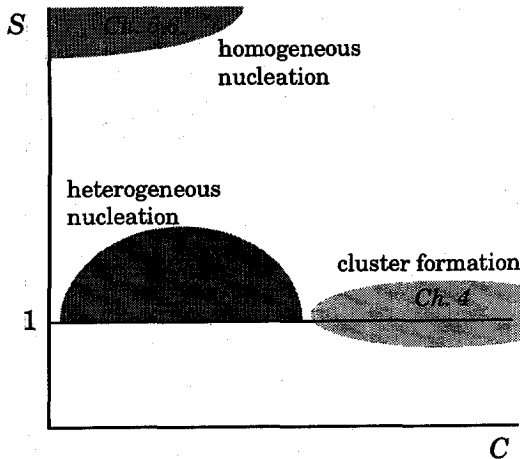


Fig. 1.3. This thesis is subdivided into four parts. After a theoretical part, three other parts are presented, which constitute one of the nucleation regimes shown here schematically. The supersaturation is shown as function of concentration. $S=1$ represents equilibrium.

The second part which contains *chapter 4*, deals with the formation of subcritical clusters in concentrated (30 to 60 volume percent) solutions of easily soluble compounds. Here, homogeneous nucleation does not take place, because the supersaturation is far too low. Chapter 4 shows that very small clusters are identified by PCS measurements in concentrated sucrose and citric acid solutions, even if they are undersaturated.

The third part of this thesis deals with the homogeneous nucleation of compounds with relatively low concentration but with very high supersaturation. *Chapter 5* reports the results of a process which starts with homogeneous nucleation

from the gas phase. In an aerosol reactor, the growth of silicon nitride was monitored by PCS. Nucleation occurs almost instantaneously and particles grow by coagulation. The average particle size and the laminar velocity of the particles which were formed in a flame were deduced from PCS and compared with the results obtained by an agglomeration model. *Chapter 6* discusses the precipitation of sulfur, an example of a process which starts with homogeneous nucleation and is controlled by chemical reaction. Colloidal sulfur precipitates if thiosulfate solutions are acidified. Under certain conditions monodisperse colloids form, whose growth can be appropriately followed by PCS. The kinetic data and the induction times found are compared with theory.

The last part consists of *chapter 7* and discusses heterogeneous nucleation from solution. The subject is the batch precipitation of barium sulfate from solution which starts with heterogeneous nucleation on seeds. Because the kinetic data of this process are relatively well documented, it was possible to model the evolution of the crystal size distribution with a population balance model. With this model the autocorrelation functions, reflecting the raw data of the PCS measurements, could be calculated and then compared to the functions obtained by the real measurements. Thus, by adjusting the parameters needed for the population balance equation, by fitting both autocorrelation functions, the kinetics for this system were resolved and compared to the literature data.

References

- M.L. Baraké (1994) *Homogeneous Nucleation from Solution. A Modelling Approach*. Dutch equivalent of M.Sc. Literature Thesis, Delft University of Technology.
- A. Boxman (1992) *Particle Size Measurement for the Control of Industrial Crystallizers*, Ph.D. thesis Delft University of Technology.
- H.Z. Cummins, N. Knable and T. Yeh (1964) *Phys. Rev. Lett.* **12**, 150.
- H.S. Dhadwal and B.Chu (1990) A Fiber Optic Laser Light Spectrometer, *Review of Scientific Instruments*, **60**, 845-853.
- R. Eek (1995) *Control and Dynamic Modeling of Industrial Suspension Crystallizers*, Ph.D. thesis Delft University of Technology.
- R. Finsy (1994) Particle Sizing by Quasi-Elastic Light Scattering, *Advances in Colloid and Interface Science*, **52**, 79-143.
- C.M.G. Heffels (1995) *On-line Particle Size and Shape Characterization by Narrow Angle Light Scattering*, Ph.D. thesis Delft University of Technology.
- M.C. van der Leeden (1991) *The Role of Polyelectrolytes in Barium Sulphate Precipitation*, Ph. D. Thesis, Delft University of Technology.
- S. Mann, D.D. Archibald, J.M. Didymus, T. Douglas, B.R. Heywood, F.C. Meldrum and N.J. Reeves (1993) Crystallization at Inorganic-Organic Interfaces: Biominerals and Biomimetic Synthesis, *Science*, **261**, 1286-1292.
- B.B. Weiner (1992) Twenty Seven Years of QELS: A Review of the Advantages and Disadvantages of Particle Sizing with QELS, in N.G. Stanley-Wood and R.W. Lines (eds) *Particle Size Analysis*, The Royal Society of Chemistry, Cambridge, 173-185.
- H. Wiese and D. Horn (1991) Single-mode fibers in fiber-optic quasielastic light scattering: A study of the dynamics of concentrated latex dispersions, *J. Chem. Phys.*, **94**, 6492.

6 *Measurement and modeling of cluster formation*

Nucleation from solution

2

Abstract

This chapter is an outline of the theory on nucleation from solution. Because of its complexity some assumptions must be made in order to derive an equation for the nucleation rate and the cluster size distribution. Three theories are compared, *the detailed balance theory, the purely kinetic theory, and the simplified equation.*

From classical thermodynamics, it is possible to obtain the equilibrium cluster size distribution as a function of supersaturation. The detailed balance theory considers a semi-equilibrium and by using the principle of steady state, the real cluster size distribution is expressed in terms of the equilibrium cluster size distribution and the forward reaction rate.

The purely kinetic theory also uses the equilibrium cluster size distribution, but instead of assuming a detailed balance it uses a kinetic argument to obtain expressions for the nucleation rate and cluster size distribution, i.e. at equilibrium the backward reaction rate equals the forward reaction rate.

The semi-empirical equation is a simplification of the detailed balance theory. It uses the equilibrium cluster size distribution in stead of the real distribution.

At the end of this chapter the results of model calculations on nucleation rates in barium sulfate solutions are given. The homogeneous nucleation rates predicted by the different theories coincide quite well but different interfacial energies must be chosen in order to achieve this. In addition, the effect of heterogeneous nucleation is clearly demonstrated.

2.1 Introduction

Crystallization and precipitation processes start with the formation of very small clusters which precede the actual macroscopic crystals. To control nucleation processes, therefore, detailed knowledge about these clusters is needed. In particular, such knowledge about the nucleation rate and the size of the critical cluster is necessary.

In this thesis, the term 'cluster' is used for assemblies of chemically bonded molecules or ions. In solutions, they are continuously forming and redissolving. The size at which clusters have grown sufficiently to become macroscopic crystals is called the *critical cluster size*. The number of these critical clusters which form per unit time and unit volume is, by definition, the nucleation rate. Therefore, in literature, this critical cluster size is sometimes referred to as a 'nucleus', but since this term is sometimes also used for subcritical clusters, it has not been adopted in this thesis in order to avoid confusion. Additionally, the term 'embryo' is sometimes used for a cluster or a critical cluster.

The critical cluster is not a physical entity, but is defined in terms of energy. Its size is the size above which clusters develop into a crystal. The critical cluster size is determined by thermodynamic parameters including the supersaturation and the interfacial tension. Clusters can grow by coalescence or by the addition of solute molecules one at a time to form a critical cluster.

8 Measurement and modeling of cluster phenomena

As outlined in the General Introduction, nucleation is a widespread phenomenon in nature. Examples are cloud and fog formation, bubble formation in boiling liquids, crystallization from melts and precipitation from solutions. In principle, all these phenomena can be described by the same set of equations but this chapter concentrates on primary nucleation from solutions.

Nucleation mechanisms are commonly lumped into one of two categories - primary and secondary nucleation - and can be classified further as shown in fig. 2.1 (Rawlings et al. 1993).

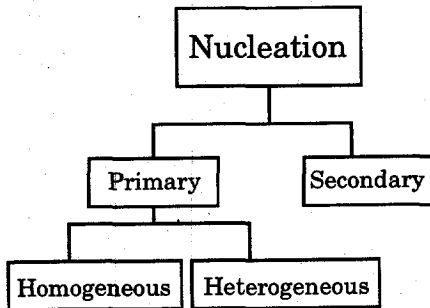


Fig. 2.1. Nucleation mechanisms according to Randolph and Larson (1988). Primary nucleation is characterized by the absence of a participating crystallizing phase, such as crystal fragments in a solution. Heterogeneous nucleation takes place on foreign surfaces, whereas homogeneous nucleation occurs in the bulk.

A basic criterion for this distinction is the presence or absence of the nucleating phase. Mechanisms of crystal formation which occur irrespective of the presence of other suspended crystals of the same material are classified as *primary* or *spontaneous nucleation*. Primary nucleation is often partitioned into *homogeneous nucleation*, which occurs in the pure bulk solution and is usually associated with high levels of supersaturation, and *heterogeneous nucleation*, which is induced by foreign surfaces, like vessel walls, colloids, dust and other impurities. Foreign surfaces and particles often promote nucleation as a result of an ordering or templating process caused by interactions across the interface between the heterogeneous particles and the mother phase. In macroscopic terms, heterosurfaces have the effect of lowering the interfacial tension and as a result primary, heterogeneous nucleation can occur at supersaturations significantly lower than those required for homogeneous nucleation. Thus, it is the dominant mechanism for primary nucleation at low supersaturations. The thermodynamics and kinetics of nucleation are discussed in sections 2.2 and 2.3, respectively. Section 2.4 deals with heterogeneous nucleation.

Secondary nucleation describes the nucleation which takes place due to the presence of other solute crystals. The secondary nuclei are generally formed by the attrition of large crystals in a crystallizer.

In principle, the same theories are applicable for both sparingly soluble salts such as barium sulfate as well as for well-soluble compounds such as citric acid and sucrose. However, in solutions of highly soluble salts (e.g. 70 mass percent in water) high supersaturations cannot develop easily. Hence, the cluster size distribution can be calculated and measured, but since homogeneous nucleation only occurs at high supersaturation, the nucleation rate derived has no practical meaning. On the

other hand, in sparingly soluble compound solutions, the cluster concentration is so low that it cannot be monitored experimentally. In addition, the critical cluster size approaches one monomer at the high supersaturations which are easily attained for sparingly soluble compounds. In such cases, homogeneous nucleation takes place and can be modeled with the theory derived.

Despite the fact that homogeneous nucleation is a relatively rare event, its basic principles form the necessary background for the understanding of numerous processes in science and technology as well as in nature when phase transitions are involved. This chapter is an outline of the nucleation theory, based on classical insights. It follows closely Kashchiev (1969, 1970, 1990) and Chiang et al. (1988), but the theoretical framework was already established in the years 1926-1949. References to this work can be found in Zettlemoyer (1969).

In section 2.3, three theories are compared, *the detailed balance theory*, *the purely kinetic theory*, and *the simplified equation*. They have been chosen from many other nucleation theories because they are useful for quantifying the kinetics and thermodynamics of nucleation from solution and because they contain only one or two parameters which cannot be determined experimentally. Section 2.4 discusses heterogeneous nucleation.

In section 2.5, the nucleation rate is calculated for barium sulfate in water, using the three different theories. The chapter finishes with some conclusions.

2.2 Thermodynamics

2.2.1 Basics

The formation of a solid phase from solution is an example of a first order phase transition. Hence, at the phase transition, the first derivatives of the chemical potentials are discontinuous,

$$\left(\frac{\partial \Delta\mu}{\partial p}\right)_T = \Delta V_m \neq 0 \quad \text{and} \quad \left(\frac{\partial \Delta\mu}{\partial T}\right)_p = \Delta S_m \neq 0, \quad (2.1)$$

$$\text{where } \Delta\mu = \mu_s - \mu_c. \quad (2.2)$$

μ_s is the chemical potential of the solvated ions or molecules, μ_c is the chemical potential of the crystal phase, p is the pressure, V_m is the molecular volume, T is the temperature and S_m the molecular entropy (Atkins 1986). For crystallization from solutions the driving 'force', or the free energy change, equals

$$\Delta\mu = \delta(\mu_s(a) - \mu_s(a_{eq}) + \mu_c(a) - \mu_c(a_{eq})), \quad (2.3)$$

where a is the activity of the ion and δ is the number of ions in the formula unit (Van der Leeden 1991, p. 183).

$$\text{Since } \mu_s = \mu_s^* + kT \ln a \quad \text{and} \quad \mu_c = \delta kT \ln a_{eq} \approx \text{constant}, \quad (2.4)$$

$$\Delta\mu = \delta kT \ln \left(\frac{a}{a_{eq}}\right) = \delta kT \ln S, \quad \text{where } S \equiv \left(\frac{\Pi}{\Pi_{eq}}\right)^{\frac{1}{\delta}}. \quad (2.5)$$

The asterisk denotes the reference state and Π and Π_{eq} are the ionic activity product and the solubility product respectively. S is the supersaturation. This expression for the free energy change is central to all of the theories concerning crystallization phenomena.

2.2.2 Free energy change for cluster formation

As explained in the introduction, homogeneous nucleation is the formation of new particles from a solution as a result of only supersaturation. For the process to be spontaneous, there must be a reduction in free energy. In solutions, clusters of solute molecules are continuously forming and redissolving. Their free energy consists of two parts, a volume free energy gained from bond or crystal lattice formation and a surface free energy needed for the formation of a new surface. In crystallization processes the surface free energy is always positive. For nucleation to occur, the volume free energy must be sufficiently negative to overcome the positive surface free energy so that the cluster will not decompose spontaneously. As the cluster size increases, the net free energy passes through a maximum value called the critical free energy of nucleation. In a sufficiently supersaturated solution this barrier to nucleation can be overcome and stable critical clusters are produced. Subsequent growth of these clusters can further reduce the free energy of the system. Classical (non-quantum) nucleation theory is based on these free energy considerations (Loehman 1992).

Kashchiev (1990) gave a general quantitative method for calculating the free energy change involving the formation of clusters. The free energy change, ΔG , equals the work involved at isothermal conditions in a closed system.

The free energy change can be calculated as follows. Take two states, I and II , containing a surface area A and N molecules. In state II n particles from N have formed a different phase on surface area A or in the bulk.

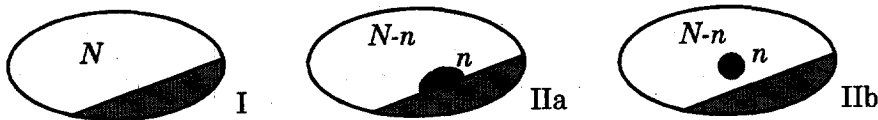


Fig. 2.2. In state II n molecules out of N have formed a cluster on the surface A (IIa , heterogeneous nucleation) or in the bulk (IIb , homogeneous nucleation).

In state I the free energy is

$$G_I = N\mu_s + G_0 + \phi_I, \quad (2.6)$$

where ϕ is the interfacial energy and G_0 the solvent free energy. This becomes in state II ,

$$G_{II}(n) = (N-n)\mu_s + n\mu_c + G_0 + \phi_{II}(n). \quad (2.7)$$

Hence,

$$\Delta G(n) = -n(\mu_s - \mu_c) + \phi_{II}(n) - \phi_I. \quad (2.8)$$

This equation can be rewritten into,

$$\Delta G(n) = -n\Delta\mu + \phi(n), \quad (2.9)$$

$$\text{where } \phi(n) \equiv \phi_{II}(n) - \phi_I \quad (2.10)$$

$$\text{and } \phi_I = A_I \sigma_A, \quad (2.11)$$

while $\phi_{II}(n)$ is unknown. σ is the specific interfacial energy. However, in the classical capillary approximation, which is valid for large n , $\phi_{II}(n)$ can be estimated by,

$$\phi_{II}(n) = A_{II}(n) \sigma_A + \sum_k A_k(n) \sigma_k, \quad (2.12)$$

where $A_{II}(n)$ equals the original surface area, A_I , minus the surface area on which the new cluster has been formed. Of course, in case *IIb*, A_I equals A_{II} . In case *IIa*, one of the crystal faces, k , is attached to the original surface, A_I , with a corresponding interfacial tension, σ_k . In the classical approximation, the free energy change becomes,

$$\Delta G(n) = -n\Delta\mu + \sum_k A_k(n) \sigma_k + [A_{II}(n) - A_I] \sigma_A. \quad (2.13)$$

In the next subsections this equation is worked out for three different types of phase transition.

Nucleation of a homogeneous droplet

The simplest case concerning nucleation is the formation of one spherical droplet or spherical solid particle from the gas phase (case *IIb* in fig. 2.2). Classically,

$$A_I = A_{II}(n) \text{ and } \sum_k A_k \sigma_k = A(n) \sigma = A_m \sigma n^{\frac{2}{3}}. \quad (2.14)$$

Thus,

$$\Delta G(n) = -n\Delta\mu + A_m \sigma n^{\frac{2}{3}}, \quad (2.15)$$

where A_m is the monomer surface area. This equation is often used, but it should be noted that it is only valid for large n , because the capillary approximation was used in the derivation. Therefore, it can be used at low supersaturation, since at high supersaturation the critical cluster size generally consists of only a few monomers.

Formation of a homogeneous crystal

This case is very similar to the former, but the shape of the cluster is incorporated with the help of the shape factors k_a and k_v ,

$$\sum_k A_k \sigma_k = \bar{\sigma} \sum_k A_k = \bar{\sigma} A(n) = \bar{\sigma} \frac{k_a}{k_v^{\frac{2}{3}}} V_m^{\frac{2}{3}} n^{\frac{2}{3}}, \quad (2.16)$$

where,

$$\bar{\sigma} = \frac{\sum_k A_k \sigma_k}{\sum_k A_k} \text{ and} \quad (2.17)$$

$$A = k_a r^2 \text{ and } V = k_v r^3. \quad (2.18)$$

Then,

12 Measurement and modeling of cluster phenomena

$$\Delta G(n) = -n\Delta\mu + \bar{\sigma} \frac{k_a}{k_v^3} V_m^{\frac{2}{3}} n^{\frac{2}{3}}. \quad (2.19)$$

Crystal growth: a disk on a substrate of the same composition

The last example concerns the formation of a two-dimensional disk with radius r on a surface that is made out of the same material as the cluster itself. A schematic view is drawn in fig. 2.3.

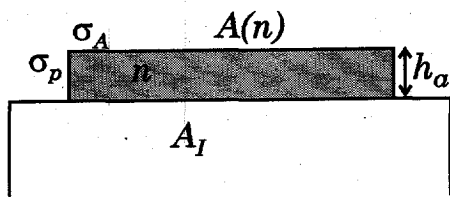


Fig. 2.3. Schematic view of a cluster of n monomers on a surface A_I . The height of this two-dimensional cluster is h_a and its surface area $A(n)$. σ_A and σ_p are the specific free energies of the surface and of the side, respectively.

In this case, the surface area in state I is diminished by the formation of the disk shaped cluster,

$$A_{II}(n) = A_I - A(n) = A_I - \pi r^2. \quad (2.20)$$

The total surface energy created by the clusters is

$$\sum_k A_k \sigma_k = \pi r^2 \sigma_A + 2\pi r h_a \sigma_p + \pi r^2 \cdot 0 = \pi r^2 \sigma_A + 2\pi r h_a \sigma_p. \quad (2.21)$$

This leads to

$$\Delta G(n) = -n\Delta\mu + 2\pi r h_a \sigma_p = -n\Delta\mu + \kappa b \sqrt{n}, \quad (2.22)$$

where $\kappa \equiv h_a \sigma_p$ and $b \equiv 2\sqrt{\pi V_m / h_a}$.

κ is the specific edge energy. The two-dimensional formation of critical clusters is an important growth mechanism for many compounds, e.g. for barium sulfate it is the rate determining step for crystal growth in a broad supersaturation range (Chiang et al. 1988, Van der Leeden 1991). Therefore, this model is used in chapter 7, where barium sulfate precipitation is investigated.

2.2.3 Thermodynamics involved in formation of critical clusters

Quantitatively, the expressions for the free energy change for cluster formation (eq. 2.14, 2.19 and 2.22) follow the same trend. For small n , ΔG increases as n increases, but at some point a maximum is reached. The cluster size at this maximum is called the critical cluster size. The free energy change at this point is the free energy, or the work, associated with critical cluster formation. As an example, this has been calculated for an aqueous solution of barium sulfate (fig. 2.4).

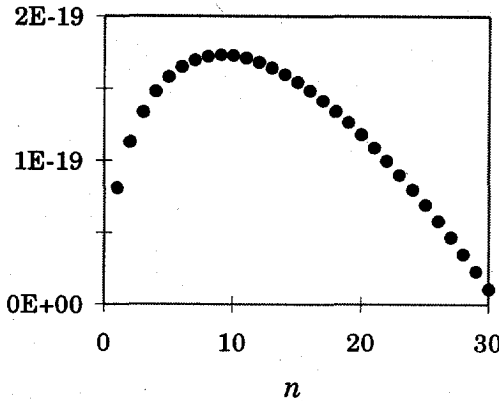


Fig. 2.4. Free energy change $\Delta G(n)$ [J] for cluster formation in an aqueous barium sulfate solution as a function of the cluster size n at supersaturation $S = 100$, using eq. (2.15). The critical cluster size is 9. Due to this low number the use of this equation is questionable. Spherical clusters are assumed and an interfacial energy of 126 mJm^{-2} .

If a cluster reaches this critical size it will grow into a crystal, because this is energetically more favorable than dissolving. On the average, smaller clusters dissolve. The critical cluster size n^{crit} can be found by calculating the maximum of the free energy change,

$$\left(\frac{d\Delta G}{dn} \right)_{n=n^{crit}} = 0. \quad (2.23)$$

Using these equations, the expressions for the critical values can be evaluated easily. Some of them are summarized in table 2.1.

Table 2.1. Expressions for the interfacial energy, the critical cluster size and the critical Gibbs free energy for homogeneous formation of a sphere (3D), and for formation of a disk on a flat surface of the same composition (2D).

	3D nucleation (sphere)	2D growth (disk)
$\phi(n)$	$\sigma A_m n^{\frac{2}{3}}$	$\kappa b \sqrt{n}$
n^{crit}	$\left(\frac{2A_m \sigma}{3\Delta\mu} \right)^3$	$\left(\frac{b\kappa}{2\Delta\mu} \right)^2$
r^{crit}	$\left(\frac{3n^{crit} V_m}{4\pi} \right)^{\frac{1}{3}} = \frac{2\sigma V_m}{\Delta\mu}$	$\left(\frac{n^{crit} V_m}{h_a 4\pi} \right)^{\frac{1}{2}} = \frac{\kappa V_m}{2h_a \Delta\mu}$
ΔG^{crit}	$\frac{4A_m^3 \sigma^3}{27\Delta\mu^2}$	$\frac{b^2 \kappa^2}{4\Delta\mu}$

Assumptions in the classical thermodynamic theory

In the theory outlined above several postulates and approximations are made (Peters et al. 1990, Kashchiev 1990). They are:

- The phase boundary is a density discontinuity. Clusters are present with the geometry of the lowest total specific surface area. Additionally, their shape is independent of $\Delta\mu$ and both phases are ideal and incompressible.
- Equilibrium thermodynamic equations of state can be used to represent non-equilibrium states.
- Thermodynamics remain relevant as phase dimensions are reduced to a molecular scale, e.g. $\phi(n)$ is defined via the macroscopic quantities σ and κ . These values are assumed to be independent of n and $\Delta\mu$.
- $G(n)$ is a continuous function of n . Especially for small n_{crit} , the discontinuity results in a pronounced difference with the continuous classical expression.
- Clusters are sufficiently dilute that interactions among clusters may be neglected. The system is in contact with a material reservoir which instantaneously replenishes molecules depleted by the growing cluster.

Despite these assumptions, the classical theory is a good approximation for dilute systems at low supersaturations. However, at high supersaturation, the critical cluster size contains only a few monomers. The use of properties such as interfacial tension is questionable in these cases.

2.3 Kinetics

In literature, the theory concerning kinetics of nucleation, is often confusing because inherently thermodynamic aspects and inherently kinetic aspects are mixed in the equations. Kashchiev (1986) and Chiang et al. (1988) showed that it is possible to obtain equations for the nucleation rate without making assumptions which do not seem valid. Central in their approximations is the steady state equilibrium cluster size distribution. Kashchiev (1986) uses thermodynamic arguments to obtain the equilibrium distribution whilst Chiang et al. (1988) employ only kinetic arguments.

In this section both methods are explained and compared with the semi-empirical equation for the nucleation rate which is often used in practice.

2.3.1 The steady state approach

In order to obtain the nucleation rate in the steady state approach, the cluster size must be evaluated in equilibrium and non-equilibrium conditions. Therefore, this section starts with the derivation of the equilibrium cluster size distribution. From this, the real distribution and the nucleation rate are obtained.

The equilibrium cluster size distribution can be recovered from Boltzmann statistics for true equilibrium thermodynamics. Boltzmann statistics give,

- that the probability for a fluctuation is proportional to
- $$\exp\left(-\frac{\text{energy cost for fluctuation}}{kT}\right),$$
- and that the probability is proportional to the concentration.
- Thus, the cluster size distribution in solutions C_{eq} becomes,

$$C_{eq}(n) = C_0 \exp\left(-\frac{\Delta G(n)}{kT}\right). \quad (2.24)$$

C_0 is usually considered to be the number of nucleation sites per volume provided that the number of clusters is much smaller than the number of monomers. In this approximation, for homogeneous nucleation, C_0 equals $1/V_m$.

The equilibrium cluster size distribution is needed to obtain the real cluster size distribution as a function of supersaturation. This will be dealt with in the next section.

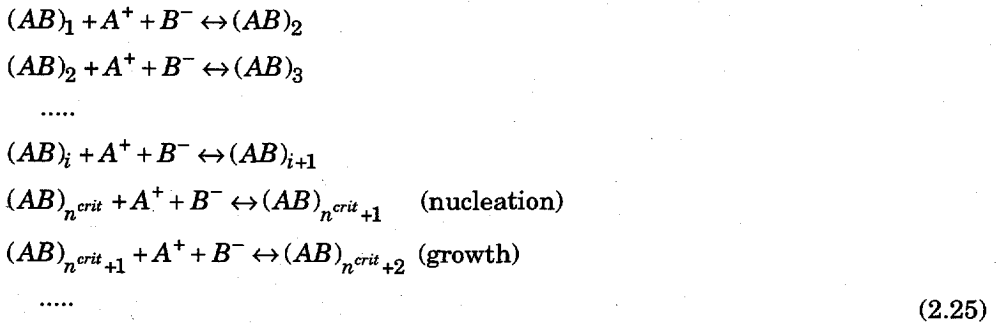
2.3.2 The real cluster size distribution

The master equation for cluster formation can be written down easily if three assumptions are made:

1. In solution, clusters of different size n exist.
2. The transition of size n to size m occurs with a known frequency f_{nm} .
3. All clusters have the same shape.

The possible transitions are visualized schematically in fig. 2.5.

From a kinetic point of view the cluster formation takes place in the following way,



The phase change takes place by single 'molecules' becoming attached to clusters of various sizes; these processes predominate slightly over the reverse processes in which the various clusters loose single 'molecules'. The size distribution of clusters changes, the number of the larger ones increase with time. The formation of critical clusters forms the bottleneck of the phase change. If the clusters achieve this critical size there is a high probability that they will grow, relatively unhindered, to macroscopic size.

By imagining some mechanism which removes clusters above a certain size, dissociates them and returns the single molecules to the system, a stationary reaction state results (S is constant in time). In this state, the numbers of the various species remain constant and there is a steady flux through the species. This flux is the steady state or stationary nucleation rate.

Using the scheme shown in fig. 2.5, the cluster size distribution $Z(n,t)$ can be written as (Kashchiev 1984),

$$\frac{dZ(n,t)}{dt} = \sum_{m=1}^N [f_{mn}(t)Z(m,t) - f_{nm}(t)Z(n,t)] + K(n,t) - L(n,t),
 \tag{2.26}$$

where $K(n,t)$ and $L(n,t)$ are the rates at which clusters are introduced and taken out of the system, respectively. $N(t)$ is the total number of units (e.g. molecules). For a closed system $K(n,t) = L(n,t) = 0$, eq. (2.26) assumes the form of a continuity equation,

$$\frac{dZ(n,t)}{dt} = J(n-1,t) - J(n,t), \quad (2.27)$$

with $J(n,t)$ defined as

$$J(n,t) = \sum_{i=n+1}^N \sum_{m=1}^n [f_{mi}(t)Z(m,t) - f_{im}(t)Z(i,t)]. \quad (2.28)$$

$J(n,t)$ is the rate of appearance of $(n+1)$ -sized clusters at time t , or the n,t -dependent flux of clusters along the size axis.

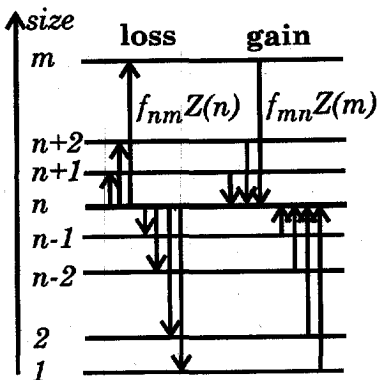


Fig. 2.5. Schematic view of all possible changes of cluster size. Consider the population of clusters that contains n monomers. This population loses its members with the frequencies $f_{nm}Z(n)$ and gains its members with $f_{mn}Z(m)$. Using this scheme, it is a straightforward procedure to write down the master equation for cluster formation.

In the nucleation stage, it is probable that the cluster size changes by gaining only one monomer at a time, because the cluster concentration is usually much lower than the monomer concentration and, therefore, the chance of cluster coalescence is negligible. The energy involved for a cluster to lose more than one monomer at a time is assumed to be so high that this does not occur. Hence, $f_{nm} = 0$ for $|n - m| \geq 2$.

With this assumption the master equation (2.26) reduces to,

$$\frac{dZ(n,t)}{dt} = f(n-1,t)Z(n-1,t) - b(n,t)Z(n,t) - f(n,t)Z(n,t) + b(n+1,t)Z(n+1,t), \quad (2.29)$$

where $f(n) = f_{n,n+1}$ (forward) and $b(n) = f_{n,n-1}$ (backward), are the frequencies of monomer joining and leaving, respectively,



The expression for the appearance rate of $(n+1)$ -sized clusters, eq. (2.28) reduces to,

$$J(n,t) = f(n,t)Z(n,t) - b(n+1,t)Z(n+1,t). \quad (2.31)$$

Eqs (2.29) and (2.31) are extensively used in nucleation kinetics. In equilibrium ($Z(n,t) = C_{eq}(n,t)$), eq. (2.31) equals 0. Using this, $b(n,t)$ can be expressed in terms of $f(t)$, and $C_{eq}(n,t)$. By eliminating $b(n,t)$ from eq. (2.29) one obtains,

$$\begin{aligned} \frac{dZ(n,t)}{dt} = & f(n-1)Z_{eq}(n,t) \left[\frac{Z(n-1,t)}{Z_{eq}(n-1,t)} - \frac{Z(n,t)}{Z_{eq}(n,t)} \right] \\ & - f(n)Z_{eq}(n,t) \left[\frac{Z(n,t)}{Z_{eq}(n)} - \frac{Z(n+1,t)}{Z_{eq}(n+1)} \right]. \end{aligned} \quad (2.32)$$

If n is regarded as a continuous variable this transforms into

$$\frac{\partial Z(n,t)}{\partial t} = \frac{\partial}{\partial n} \left\{ f(n)Z_{eq}(n,t) \frac{\partial Z(n,t)}{\partial n} \right\}. \quad (2.33)$$

This is the Zeldovich equation (Zettlemoyer 1969) which describes the nucleation at time independent¹⁾ supersaturation. Accordingly, eq. (2.31) becomes

$$J(n,t) = -f(n,t)Z_{eq}(n,t) \frac{\partial Z(n,t)}{\partial n} \frac{1}{Z_{eq}(n,t)}. \quad (2.34)$$

2.3.3 Steady state - detailed balance

In the metastable zone, where solutions are supersaturated but do not yet crystallize, a steady state develops. In a steady state, the term $dZ(n,t)/dt$ in eq. (2.32) equals 0, and with boundary conditions $Z(1) = C_{eq}(1)$ and $Z_{\infty} = 0$ one finds,

$$Z(n) = C_{eq}(n) \left\{ 1 - \frac{\int_1^n \frac{dn}{f(n)C_{eq}(n)}}{\int_1^{\infty} \frac{dn}{f(n)C_{eq}(n)}} \right\}. \quad (2.35)$$

Using this *method of detailed balance*, the average number of molecules in a cluster can be calculated using

$$\bar{n} = \frac{\int_1^{\infty} nZ(n)dn}{\int_1^{\infty} Z(n)dn}. \quad (2.36)$$

Furthermore, the stationary nucleation rate J (eq. 2.34) can be calculated from eq. (2.35). It is $J(n)$ for $n=n^{crit}$,

$$J = -f(n)C_{eq}(n^{crit}) \frac{\partial}{\partial n} \left\{ 1 - \frac{\int_1^{n^{crit}} \frac{dn}{f(n)C_{eq}(n)}}{\int_1^{\infty} \frac{dn}{f(n)C_{eq}(n)}} \right\}. \quad (2.37)$$

¹⁾ If small steps are taken this is also valid for time dependent supersaturation.

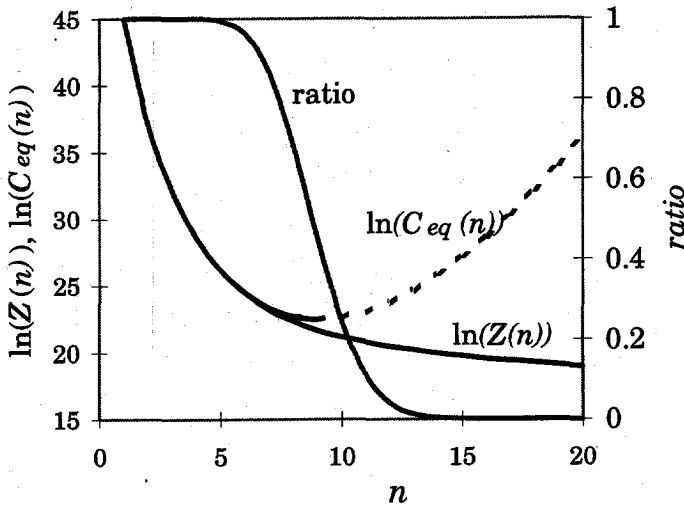


Fig. 2.6. The equilibrium cluster size distribution $C_{eq}(n)$ and the steady state cluster size distribution $Z(n)$ for an aqueous barium sulfate solution at $S=25$, calculated using eqs (2.24) and (2.35). The slope of their ratio at the critical cluster size is proportional to the nucleation rate, according to eq. (2.34). Spherical clusters are assumed. The critical cluster size is 9 units.

2.3.4 The kinetic approach

Chiang, Donohue and Katz (1986) showed that $b(n)$ in eq. (2.29) can be excluded with the aid of a purely kinetic argument. They defined a recursive relationship for the reactions given in eq. (2.25),

$$Y(n+1) = \frac{Y(n)b(n+1)}{f(n+1)} \quad \text{for } n > 1 \quad (2.38)$$

with $Y(1) = 1$.

$Y(n)$ is the cluster size distribution by number, normalized to 1 for $n = 1$. This relation can be solved yielding,

$$Y(n) = \prod_{j=1}^n \frac{b(j)}{f(j)}. \quad (2.39)$$

By multiplying the time-independent equivalent of eq. (2.31) with $Y(n)$ an equation with two terms on the right hand side of similar appearance is obtained,

$$J(n)Y(n) = f(n)Z(n)Y(n) - f(n+1)Z(n+1)Y(n+1). \quad (2.40)$$

Thus on summing, successive terms cancel resulting in,

$$\sum_{j=1}^n J(j)Y(j) = f(1)Z(1) - f(n)Z(n)Y(n). \quad (2.41)$$

Because $Z(n)$ goes to zero for high n (fig. 2.6), it is sufficient to carry out the summation to a high value of n to obtain the simple expression,

$$\sum_{j=1}^{\bar{n}} J(j)Y(j) = f(1)Z(1) - f(\bar{n})Z(\bar{n})Y(\bar{n}) = f(1)Z(1). \quad (2.42)$$

For a pseudo-steady state the nucleation rate, J , can be factored out of the summation, resulting in the formula of Becker and Döring (Kashchiev 1984),

$$J = \frac{f(1)Z(1)}{1 + \sum_{j=2}^{\bar{n}} \prod_{i=2}^j \frac{b(i)}{f(i)}}. \quad (2.43)$$

Chiang et al. (1986) argued that diffusion does not determine the reaction rate in nucleation because the clusters are very small and thus diffuse rapidly. Hence, by finding expressions for the forward and backward frequencies $f(n)$ and $b(n)$, the nucleation rate, J , can be obtained.

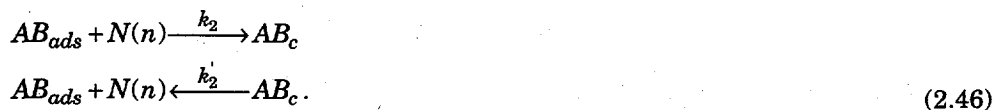
For compounds like barium sulfate, crystal or cluster growth takes place in the following way (Chiang et al. 1988),



$N(n)$ is the number of vacant positions on the crystal surface. The other mechanism considered by Chiang et al. is the integration of ions, after adsorption, into the crystal surface (sequential ionic integration). For the surface reaction - molecule integration mechanism they considered two possible rate determining steps. The first is the surface reaction,



The second is the molecular integration of the adsorbed 'molecules',



The reaction rates are,

$$\begin{aligned} f_1(n) &= k_1 [A_{ads}^+][B_{ads}^-] \\ b_1(n) &= k_1' [AB_{ads}] \\ f_2(n) &= k_2 [AB_{ads}][N(n)] \\ b_2(n) &= k_2' [N(n)][A^+][B^-]. \end{aligned} \quad (2.47)$$

In the reaction constant k'_b , not only incorporates k'_2 , but also other reaction and equilibrium constants.

Depending on the rate determining steps, four combinations of $f(n)$ and $b(n)$ are possible. In order to relate these rates to macroscopic properties such as the overall growth rate and the supersaturation, expressions for the concentration of the adsorbed species must be obtained. Chiang and Donohue (1988) considered several

adsorption isotherms. For example, for the sparingly soluble salt barium sulfate the Langmuir isotherm can be used. Furthermore, reactions $f_1(n)$ and $b_2(n)$ are rate determining. Hence, $f_1(n)$ can be rewritten into,

$$f_1 = k_1 k_{AL} k_{BL} [A^+] [B^-], \quad (2.48)$$

where k_{AL} and k_{BL} are Langmuir adsorption constants. Chiang and Donohue (1988) argued that $b_2(n)$ is independent of the concentration of the solute if the interaction between the molecules (or ions) leaving the crystal and the solute molecules can be neglected. This is the case since the number of solvent molecules largely exceeds the number of solute molecules. Consequently, if the backward reaction can be determined at some arbitrary concentration it is known at any concentration.

Fortunately this backward reaction rate can be determined at the saturation concentration. Since it then equals the forward rate,

$$f_1(n) = b_2(n). \quad (2.49)$$

In addition, the equilibrium concentrations are defined at $[N(n)] = [N_\infty]^2$, i.e. the number of vacancies on an infinitely large surface.

Thus,

$$k_1 k_{AL} k_{BL} [A_{eq}^+] [B_{eq}^-] = k_b [A_{eq}^+] [B_{eq}^-] [N_\infty] \Rightarrow$$

$$k_b = \frac{k_1 k_{AL} k_{BL}}{N_\infty} \quad (2.50)$$

and $b_2(n)$ becomes

$$b_2(n) = \frac{k_1 k_{AL} k_{BL}}{N_\infty} [A_{eq}^+] [B_{eq}^-] [N(n)]. \quad (2.51)$$

The number of growth sites $N(n)$ is obtained from the equation which relates its energy to the number of sites on an infinitely long crystal surface,

$$[N_\infty] = \exp\left(-\frac{\Delta G_\infty}{kT}\right). \quad (2.52)$$

Here, ΔG_∞ is the energy required for a molecule to move to a position in the surface layer. For small spheres this energy becomes,

$$\Delta G(r) = \Delta G_\infty - \frac{2\sigma V_m}{r}. \quad (2.53)$$

This is the *Freundlich equation*. For spheres r can be related to n via,

$$r(n) = \sqrt[3]{\frac{3nV_m}{4\pi}}. \quad (2.54)$$

Combining eqs. (2.52) and (2.53) one obtains,

2) This equation is not given by Chiang et al. (1988), but has been derived from their eqs. (20) and (22). In their equation (22.1c) it seems that a term N_∞ is missing in the denominator.

$$\ln \frac{[N(r)]}{[N_\infty]} = \frac{2\sigma V_m}{r kT} \quad (2.55)$$

Eq. (2.55) suggests that the cluster surface is smooth, which is, especially for small clusters, a rather crude approximation. This result is similar to the Kelvin equation for homogeneous droplet formation in a gas. It was modified for ions formed by the dissociation of a growth site by (Hiemenz 1986, p. 305)³⁾,

$$\ln \frac{[N(r)]}{[N_\infty]} = \frac{2\sigma V_m}{\delta r kT} \quad (2.56)$$

where δ is the number of ions formed from the dissociation of a molecule.

Using eqs. (2.48), (2.51) and (2.56) the ratio of the backward to the forward reaction is obtained,

$$\frac{b(r)}{f} = \frac{[A_{eq}^+][B_{eq}^-]}{[A^+][B^-]} \exp\left(\frac{2\sigma V_m}{\delta r kT}\right) \quad (2.57)$$

Substituting eqs (2.54) and (2.57) into eq. (2.43) gives an expression for the nucleation rate, derived using only kinetic arguments

$$J = \frac{f(1)Z(1)}{1 + \sum_{j=1}^{\infty} \prod_{i=1}^n \left\{ \frac{[A_{eq}^+][B_{eq}^-]}{[A^+][B^-]} \exp\left(\frac{2\sigma V_m}{\sqrt[3]{3jV_m/4\pi} \delta kT}\right) \right\}} \quad (2.58)$$

Using this equation, the nucleation rate can be obtained if expressions for $f(1)$ and $Z(1)$ are obtained. f can be found from the linear growth rate which can be derived relatively easily from growth experiments. The net growth rate is the forward minus the backward rate, but eq. (2.57) shows that f is much larger for large crystals. $Z(1)$, the monomer concentration, can be calculated (Chiang et al. 1988) or the equilibrium constant can be found from experimental data.

The critical cluster size in this terminology can be found by calculating the cluster size for which f equals $b(n)$. At this point, the chance for a cluster to gain a monomer is larger than that of losing one.

2.3.5 Simplified expressions for the nucleation rate

Rewriting the kinetic expression for J in eq. (2.43) results in an equation with the thermodynamically defined $C_{eq}(n)$ instead of $Y(n)$ and the kinetically derived f .

$$J = \frac{f(1)Z(1)}{1 + \sum_{j=2}^{N-1} \prod_{i=2}^{N-1} \frac{b(j)}{f(j)}} \quad (2.59)$$

The denominator of the right hand side can be rewritten into,

³⁾ Chiang et al. (1988) give another equation which they took from a paper that could not be traced by the present author, because the reference given by Chang et al. did not contain the equation required. Because of this, their equivalent of δ appears in the numerator of eq. (2.55) instead of the denominator.

$$1 + \sum_{j=2}^{N-1} \frac{b(2)b(3)b(4)\dots b(j)}{f(2)f(3)f(4)\dots f(j)} = f(1) \left(\frac{1}{f(1)} + \sum_{j=2}^{N-1} \frac{1}{f(1)f(2)f(3)f(4)\dots f(j-1)} \frac{b(2)b(3)b(4)\dots b(j)}{f(j)} \right) =$$

$$f(1) \left(\frac{1}{f(1)} + \sum_{j=2}^{N-1} \frac{Z(1)}{f(j)Z(j)} \right) = f(1)Z(1) \left(\frac{1}{f(1)Z(1)} + \sum_{j=2}^{N-1} \frac{1}{f(j)Z(j)} \right) = f(1)Z(1) \sum_{j=1}^{N-1} \frac{1}{f(j)Z(j)},$$
(2.60)

where the principle of detailed balance is used. With this assumption, the rate of formation of clusters with size j (eq. 2.31) equals zero and therefore,

$$Z(j) = Z(1) \frac{f(1)f(2)\dots f(j-1)}{b(2)b(3)\dots b(j)}. \quad (2.61)$$

Thus, the following expression is obtained for the nucleation rate,

$$J = \frac{1}{\sum_{j=1}^{N-1} \frac{1}{f(j)Z(j)}}. \quad (2.62)$$

In a supersaturated system $Z_{eq}(n)$ has a minimum value of $Z(n^{crit}) \approx Z_{eq}(n^{crit})$ at $n = n^{crit}$, so the largest term in the sum of eq. (2.62) is $1/f(n^{crit})Z_{eq}(n^{crit})$. This allows this equation to be expressed in the form,

$$J = z f^{crit} Z_{eq}^{crit}, \quad (2.63)$$

where $f^{crit} = f(n^{crit})$, $Z_{eq}^{crit} = Z_{eq}(n^{crit})$ and z is the Zeldovich factor. This factor lies typically between 0.01 and 1 and can be approximated (Zettlemoyer 1969) by,

$$z = \sqrt{\frac{\left[\frac{-d^2 \Delta G(n)}{dn^2} \right]_{n=n^{crit}}}{2\pi kT}} \quad (2.64)$$

For 3D homogeneous nucleation, eq. (2.63) can be written with the help of eq. (2.24) and table 2.1 into the familiar form,

$$J(\Delta\mu) = A(\Delta\mu) \exp\left(-\frac{\Delta G^{crit}(\Delta\mu)}{kT}\right) = kS \exp\left(\frac{4A_m^3 \sigma^3}{27kT\Delta\mu^2}\right). \quad (2.65)$$

The pre-exponential kinetic factor k is usually considered to be independent of $\Delta\mu$, since the exponential term strongly dominates.

2.4 Heterogeneous nucleation

As outlined in the introduction, heterogeneous nucleation often dominates over homogeneous nucleation at low supersaturation, because the free energy for critical cluster formation is lower in the case of heterogeneous nucleation. This effect is quantified in the following section. The treatment adopted here is based on that due to Kashchiev (1990), who used the approach by Hirth and Pound (1963), Toschev (1973) and Zettlemoyer (1969).

Effect on energetics

If the energetics associated with the effect of a substrate are considered, it soon becomes clear that the substrate wetting must play an important role. The Young equation gives the relationship between the contact angle of a droplet on a flat surface and the interfacial energy.

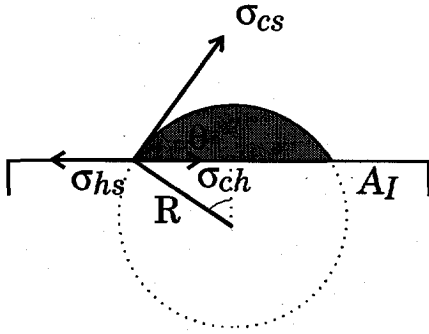


Fig. 2.7. Components of interfacial tension used in the Young equation. σ_{cs} is the interfacial tension between the crystal and the solution, σ_{ch} between the crystal and the heterogeneous surface, and σ_{hs} between the heterogeneous surface and the solution.

The Young equation is given by (Hiemenz 1986),

$$\sigma_{hs} = \sigma_{ch} + \sigma_{cs} \cos \theta. \tag{2.66}$$

According to eqs. (2.9), (2.10) and (2.11) the interfacial tension in state IIa (fig. 2.2) is given by,

$$\phi_{II}(n) = \sigma_{hs} (A_I - \pi \sin^2 \theta R^2) + \sigma_{ch} \pi \sin^2 \theta R^2 + \sigma_{cs} 2\pi(1 - \cos \theta)R^2. \tag{2.67}$$

Hence,

$$\begin{aligned} \phi(n) &= 2\pi(1 - \cos \theta)\sigma_{cs}R^2 + \pi \sin^2 \theta (\sigma_{ch} - \sigma_{hs})R^2 \\ &= \psi(\theta) 4\pi \sigma_{cs} R^2, \end{aligned} \tag{2.68}$$

where

$$\psi(n) = \frac{1}{2}(1 - \cos \theta) - \frac{1}{4} \sin^2 \theta \cos \theta. \tag{2.69}$$

From fig. 2.8 it is clear that $0 \leq \psi(n) \leq 1$. Furthermore, it can be shown that from geometrical considerations that,

$$\frac{V_m n}{\frac{4}{3} \pi R^3} = \frac{V_{segment}}{V_{sphere}} = \psi(\theta). \tag{2.70}$$

Using this it is clear that the interfacial tension for heterogeneous cluster formation is always smaller than that for homogeneous nucleation,

$$\phi(n)_{het} = \psi^{\frac{1}{3}}(\theta) \sigma A_m n^{\frac{2}{3}} \leq \phi(n)_{hom}. \tag{2.71}$$

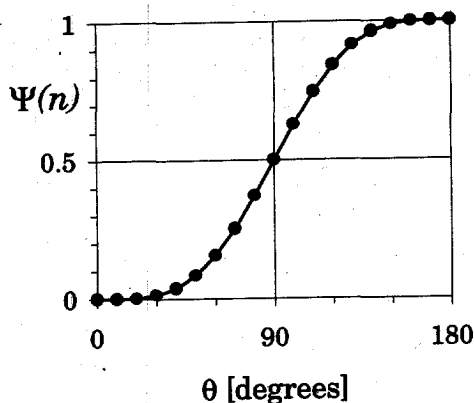


Fig. 2.8. The function $\psi(n)$ varies between 0 and 1, depending on the contact angle θ .

Effect on pre-exponential factor C_0

The pre-exponential factor C_0 in eq. (2.24) denotes, for heterogeneous nucleation, the concentration of heteroparticles or the concentration of active sites in the solution. In practice, this value is lower than the homogeneous pre-exponential factor and the nucleation rate is, therefore, lowered.

Effect on kinetics

The forward reaction rate, $f(n)$, is decreased by the presence of heteroparticles or active sites. This can be understood from the fact that the rate is proportional to the surface area of the clusters which are present. Fig. 2.7 shows that only a part of the imaginary sphere is accessible for monomers

$$f(n) \propto A_m n^{\frac{2}{3}} = A_m n_{hom}^{\frac{2}{3}} \psi^{\frac{2}{3}}(\theta). \quad (2.72)$$

Hence, the forward reaction rate is decreased by a factor $\psi^{2/3}(\theta)$.

Total effect of heterogeneous nucleation

Thus, if sufficient foreign surface is present, *heterogeneous* nucleation dominates at low supersaturation. Only at higher supersaturations does homogeneous nucleation become important, due to the lower value of the interfacial energy, which appears in the exponential term. The general equation for heterogeneous nucleation is,

$$J_{het}(\Delta\mu) = A_{het}(\Delta\mu) \exp\left(-\frac{\psi(\theta)\Delta G^{crit}(\Delta\mu)}{kT}\right), \quad (2.73)$$

An example of this has been worked out in the next section.

2.5 Example: calculation of the nucleation rate

The homogeneous nucleation rate has been calculated using the kinetic expressions derived by Chiang et al. (1988) and Kashchiev (1984). They have been compared with the experimental data found by Van der Leeden (1991, 1992). She found that

heterogeneous nucleation dominated under the experimental conditions. Thus, the effect of heterogeneous nucleation was demonstrated.

The unknown factor in the detailed balance, the kinetic and the semi-empirical equations, is the interfacial energy, σ . In addition, the simplified equation contains a pre-exponential factor which is difficult to obtain. For σ , the value 126 mJm^{-2} was taken from literature (Nielsen 1964). This value was used for the detailed balance equation and for the semi-empirical equation. The pre-exponential factor was chosen to be $10^{30} \text{ s}^{-1}\text{m}^{-3}$. This is a relatively small number for this factor compared to many other nucleation processes, but is similar to the value mentioned by Chiang et al. (1988, p. 264). In principle, the three homogeneous nucleation equations should give the same results but in order to achieve this the interfacial tension needs to be 155 mJm^{-2} in the kinetic expression. The forward rate was calculated from the crystal growth rate constant. Hotomsky et al. (1981) found this rate constant, k_G , to be $4 \cdot 10^{-8} \text{ m s}^{-1} \text{ m}^6 \text{ mol}^{-2}$. It can be transformed into terms of concentration using,

$$k_1 = \frac{k_G A_m n^{\frac{2}{3}} \rho N_A}{M} \quad (2.74)$$

The kinetic expression also uses the concentration of molecules. For the equilibrium



Van der Leeden (1991, p. 191) gives an equilibrium constant K_{AB} of $0.22 \text{ m}^3 \text{ mol}^{-1}$. All the constants used in the models are shown in table 2.2.

The results of the model calculations are visualized in fig 2.9. For the kinetic expression, in order to find approximately the same curves as the empirical expression and the detailed balance expression a rather different value for the interfacial energy had to be chosen. Chiang et al. (1988) mentioned 140 mJm^{-2} , and in this work the value 155 mJm^{-2} was taken. This difference is mostly due to the shape that was assumed. Chiang et al. (1988) assumed cubes whilst here spheres were assumed. It is difficult to obtain reliable values for the interfacial tension directly from experiment, and they are usually calculated from solubility data. Hence, it is not easy to decide which value is closer to the real one.

In the calculations, the supersaturation S is defined as,

$$S \equiv \sqrt{\frac{[\text{Ba}^{2+}][\text{SO}_4^{2-}]}{K_{eq}}}, \quad (2.76)$$

where K_{eq} is the solubility product.

Fig. 2.9 also shows the effect of heterogeneous nucleation. According to the models used, homogeneous nucleation is not likely to occur at supersaturations lower than about 100. Nielsen (1964) reported 600 for this value. However, the heterogeneous nucleation rate is strongly influenced by the number and characteristics of the foreign particles or surfaces present in the experimental setup.

Table 2.2. List of variables used in the different expressions for the nucleation rate for barium sulfate in water.

var.	Empirical (eq. 2.65)	Detailed Balance (eq. 2.34)	Kinetic (eq. 2.43)	Heterogeneous (eq. 2.73)
V_m	$8.61 \cdot 10^{-29} \text{ m}^3$	<i>id.</i>	<i>id.</i>	<i>id.</i>
A_m	$9.43 \cdot 10^{-19} \text{ m}^2$	<i>id.</i>	<i>id.</i>	<i>id.</i>
ρ	4500 kg m^{-3}	<i>id.</i>	<i>id.</i>	<i>id.</i>
M	$0.23339 \text{ kg mol}^{-1}$	<i>id.</i>	<i>id.</i>	<i>id.</i>
T	298 K	<i>id.</i>	<i>id.</i>	<i>id.</i>
k_G	-	$4 \cdot 10^{-8} \text{ ms}^{-1} \text{ m}^6 \text{ mol}^{-2}$	<i>id.</i>	-
K_{AB}	-	-	$0.22 \text{ m}^3 \text{ mol}^{-1}$	-
K_{eq}	$1.04 \cdot 10^{-4} \text{ mol}^2 \text{ m}^{-6}$	<i>id.</i>	<i>id.</i>	<i>id.</i>
A	$10^{30} \text{ s}^{-1} \text{ m}^{-3}$	-	-	$4 \cdot 10^9 \text{ S}$
β	$16\pi/3$	-	-	<i>id.</i>
δ	2	<i>id.</i>	<i>id.</i>	<i>id.</i>
σ	0.126 Jm^{-2}	0.126 Jm^{-2}	0.155 Jm^{-2}	0.040 Jm^{-2}

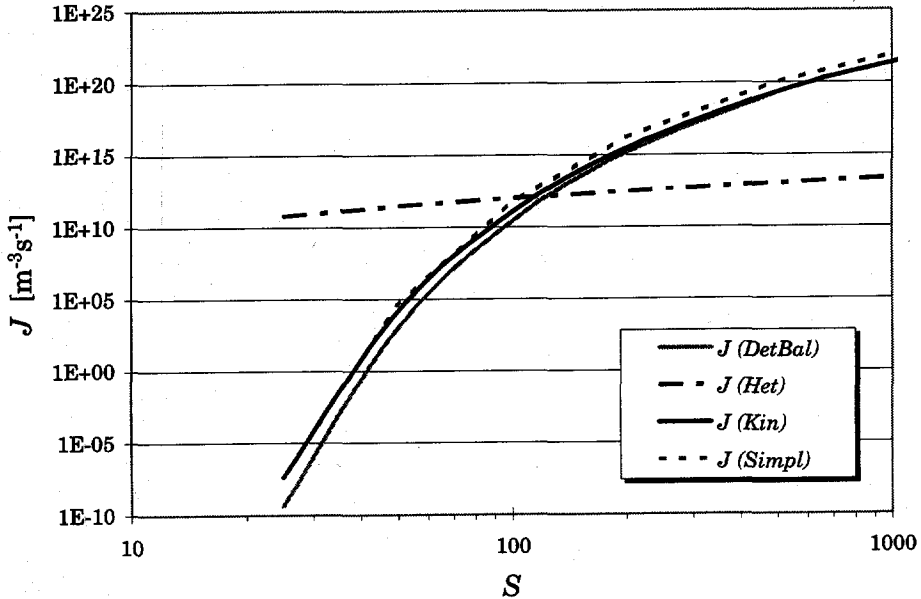


Fig. 2.9. The nucleation rate J as a function of the supersaturation for aqueous barium sulfate precipitation. It has been calculated with the equations obtained from the detailed balance (eq. 2.34) and the kinetic (eq. 2.43) theories, together with the simplified expression given in eq. (2.65) and the expression found by Van der Leeden (1992) for heterogeneous nucleation.

For barium sulfate precipitation, the results of the relatively elaborate calculations involved in the detailed balance and the kinetic expressions for the nucleation rate look very similar to the semi-empirical equation that is often used. This can be understood if it is noticed that the real cluster size distribution closely resembles the equilibrium cluster size distribution at $n = n^{crit}$. All three equations use an expression that relates the interfacial energy to the cluster size. Although in the kinetic theory another point of view is taken, this energy plays an important role via its presence in the Kelvin-like equation.

It is remarkable that the calculated nucleation rate is similar to the experimentally measured value (Chiang 1988), since the critical cluster size is far too small for the equation that relates the Gibbs free energy change to the critical cluster size. Nevertheless, this equation (2.14) appears to be useful, although it proves to be no more than a rough approximation for small n .

2.6 Conclusions

In this chapter a number of homogeneous nucleation theories have been evaluated which have a theoretically sound basis and require the lowest number of input parameters. Remarkably, for barium sulfate precipitation, the results of the relatively elaborate calculations involved in the detailed balance and the kinetic expressions for the nucleation rate appear to be very similar to the simplified equation which is often used. The advantage of the first two expressions is that only one unknown parameter needs to be fitted, namely the interfacial energy, while in the semi-empirical equation there is also an unknown pre-exponential factor.

The weakest point in the nucleation theory is that the clusters are assumed to have the same characteristics as the macroscopic crystals. It is plausible that they do not have the same shape if they are very small (less than approximately 100 monomers). In addition, the interfacial tension is only defined if a distinct interface is present. This, however, is probably not the case for very small clusters. It is possible that these effects are hidden in the value for the interfacial tension which has to be fitted anyway.

Heterogeneous nucleation dominates as the first step in crystallization phenomena, especially at low supersaturations. The surface properties and the number of heteroparticles or nucleation sites determine the difference between the homogeneous nucleation rate and the heterogeneous nucleation rate. For barium sulfate, homogeneous nucleation only occurs at supersaturations higher than 100- 600.

References

- M. Angerhöfer (1993) *Untersuchungen zur Kinetik der Fällungskristallisation von Bariumsulfat*, Thesis Technischen Universität München (in German).
- P.W. Atkins (1986) *Physical Chemistry*, Third Edition, Oxford University Press, Oxford, 145
- P.P. Chiang and M.D. Donohue (1988) A Kinetic Approach to Crystallization from Ionic Solution. I. Crystal Growth, *Journal of Colloid and Interface Science*, **122**, 230-250.
- P.P. Chiang, M.D. Donohue and J.L. Katz (1988) A Kinetic Approach to Crystallization from Ionic Solution. II. Crystal Nucleation, *Journal of Colloid and Interface Science*, **122**, 251-265.
- J.P. Hirth and G.M. Pound (1963) *Condensation and Evaporation*, Pergamon, Oxford.
- P.C. Hiemenz (1986) *Principles of Colloid and Surface Chemistry*, Second Edition, Dekker, New York.
- D. Kashchiev (1969) Nucleation at Variable Supersaturation, *Surface Science*, **18**, 293-297.
- D. Kashchiev (1970) Nucleation at Time-Dependent Supersaturation, *Surface Science*, **22**, 319-324.

28 *Measurement and modeling of cluster phenomena*

- D. Kashchiev (1984) The Kinetic Approach to Nucleation, *Crystal Res. and Technology* **19**, 1413-1423.
- D. Kashchiev (1990) *Theory of Nucleation and Growth of New Phases*, course book Delft University of Technology.
- M.C. Van der Leeden (1991) *The Role of Polyelectrolytes in Barium Sulphate Precipitation*, Thesis, Delft University of Technology.
- M.C. Van der Leeden, D. Kashchiev, G.M. Van Rosmalen (1992) Precipitation of Barium Sulphate: Induction Time and the Effect of an Additive on Nucleation and Growth, *Journal of Colloid and Interface Science*, **152**, 338.
- R.E. Loehman (ed.) (1992) *Characterization of Ceramics*, Butterworth-Heinemann, London, Chapter 1.
- A.E. Nielsen (1964) *Kinetics of precipitation*, Pergamon Press, Oxford.
- G.H. Peters, J. Eggebrecht, M.A. Larson (1990) in: *AIChE Symposium Series 438*, American Chemical Society.
- A.D. Randolph and M.A. Larson (1988) *Theory of Particulate Processes*, second edition, Academic Press, New York.
- S. Toshev (1973) in *Crystal Growth: an Introduction*, P. Hartman (ed.), North-Holland, Amsterdam, 1.
- A.C. Zettlemoyer (ed.) (1969) *Nucleation*, Chapter 5, A.G. Walton, *Nucleation in liquids and solutions*, Dekker, New York, 225-305.

Particle size determination by photon correlation spectroscopy

3

Abstract

Since the experimental section of this thesis largely relies on one particle size analysis technique, namely photon correlation spectroscopy (PCS), this chapter is entirely devoted to discussions of its background and its strengths and weaknesses. PCS measures the fluctuations of scattered laser light from an assembly of dispersed particles in Brownian motion. By quantifying these intensity fluctuations in diluted liquid dispersions of narrowly distributed, non-interacting spherical particles, their diffusion coefficient can be determined. In such cases the diffusion coefficient can be used to accurately calculate the intensity weighted hydrodynamic average particle diameter.

In all other cases several precautions must be taken in order to obtain reliable information about the particle size distribution. It must be stressed that usually only a limited amount of information, roughly two information units (e.g. average and variance), can be extracted from the measured autocorrelation function.

In laminarly flowing media, it is possible to obtain both the diffusion coefficient and an estimation of the laminar velocity of the particles. In this chapter, it is shown that it is possible to extract this information from the PCS data with a conventional analysis technique. The possibility for making measurements in flows is especially useful for aerosol characterization.

3.1 Introduction

Photon correlation spectroscopy (PCS) has become a standard technique for measuring diffusion coefficients and particle sizes in liquid dispersions of macromolecules and submicrometer particles. This is achieved by measuring the fluctuations of scattered laser light from an assembly of dispersed particles in Brownian motion. The fluctuations are quantified by autocorrelation. The measuring technique is also referred to as intensity fluctuation spectroscopy or dynamic light scattering, since the scattered light intensity is followed in time, or as quasi-elastic light scattering (QELS), because the frequency of the scattered light is (slightly) Doppler shifted due to the particle motions.

PCS is often used for characterizing colloids, emulsions, micro-organisms and cells. It plays an important role throughout this thesis because it is the most important measuring technique that has been used in this thesis for following cluster formation and crystallization processes. Therefore, this chapter discusses the background and the practical advantages and disadvantages of this technique.

In addition, the effect of a laminarly flowing medium on the measured autocorrelation functions is discussed, because this is dealt with in the measurements performed in an aerosol reactor, which are described in chapter 5.

In the short history of PCS (it was first developed in the laboratory of H.Z. Cummins in the early sixties (Weiner 1992, Cummins et al. 1964)) not only confusion arose about its name, but also about its terminology. Physicists, who were familiar with neutron scattering, called the autocorrelation function the *intermediate scattering function*, and generally used different symbols compared to physical chem-

ists. In addition, in Europe and in the United States, the same terms were used for different types of experiments¹⁾.

In this chapter, a short outline is given in order to be able to interpret measuring results obtained in the following chapters. An excellent introduction can be found in the series of papers by the members of the Belgian Particle Size Analysis Group (De Jaeger et al. 1991, Finsy and De Jaeger 1991, Finsy et al. 1991^a, Finsy et al. 1991^b and Finsy 1994). For more details, the reader is referred to Chu (1991) and Berne and Pecora (1976). Pusey (1991, 841-881) gives an overview of the effect of interactions among particles on autocorrelation functions obtained in PCS measurements.

3.2 Physical background

A schematic view of a typical light scattering experiment is shown in fig. 3.1. A laser light beam illuminates a sample volume which contains an assembly of scatterers. This can be a liquid, a liquid dispersion or an aerosol. A detector, usually a photomultiplier tube (PMT), is positioned at an angle θ . It detects the light scattered by the illuminated part of the sample with a small solid angle Ω (see appendix 3.A for more details). The detected signal is processed by a pulse amplifier discriminator (PAD) and fed into a digital correlator.

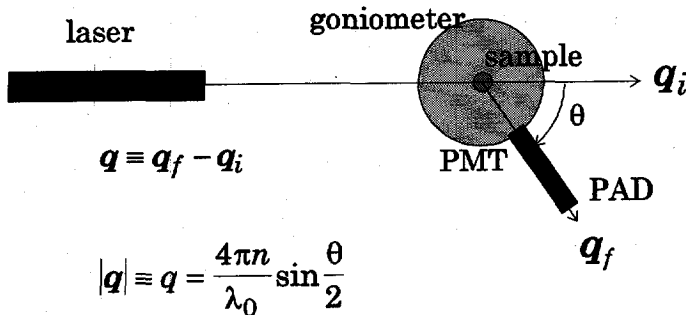


Fig. 3.1. A schematic representation of the light scattering setup which has been used in most of the experiments described in this thesis. q is the scattering vector, n the refractive index of the medium, θ the scattering angle and λ_0 the laser wavelength in vacuum.

In order to evaluate the scattered light signal the following assumptions must be made: i) the intensity of the light scattered by the medium is negligible compared to that scattered by the particles; ii) the light scattered by one particle is not scattered by a second one, i.e. multiple scattering does not occur (Born approximation); iii) the incident light is vertically polarized.

¹⁾ The experiment in which the scattered light is *not* mixed with the incident laser beam (the local oscillator) is called the *homodyne* method in Europe (e.g. Wiese and Horn 1991) and the *self-beating* method in the United States (Chu 1991). To confuse the novice in the field even more, the Americans reserve the term *homodyne* for a certain type of mixing experiment (the scattered light is mixed with a beam of the same wavelength), where the Europeans always speak about a *heterodyne* experiment if the scattered light is mixed with any local oscillator, irrespective of its wavelength. In this work, the European terminology is used.

When coherent light (i.e. one frequency and waves are in phase) is scattered by a randomly orientated assembly of particles, such as a colloidal fluid, the far-field pattern of the scattered radiation constitutes a random diffraction or speckle pattern of dark and light regions. The area of such a region, the coherence area, can be estimated by λ^2/Ω , where λ ($=\lambda_0/n$) is the wavelength of the incident light. In PCS experiments the signal to noise ratio is closely related to the number of coherence areas detected. The smaller this number, the higher the signal to noise ratio (Berne and Pecora 1976, 46). In appendix 3.A more details are given.

The instantaneous intensity of a speckle is $I(t) = |E(t)|^2$. Here $E(t)$ is the scattered electric field strength,

$$E(t) = \sum_{j=1}^N b_j(q) \exp\{i\mathbf{q} \cdot \mathbf{r}_j(t)\}, \quad (3.1)$$

where \mathbf{q} the scattering vector defined in fig. 3.1, $i^2 = -1$ and b_j the scattering amplitude of the j th particle. Vector properties are denoted in a bold italic typeface. As the particle positions $\mathbf{r}_j(t)$ change by Brownian motion, the phase relationships determining the speckle pattern change as well, and the pattern evolves through a sequence of random configurations (Pusey 1991, 842).

In PCS, a single detector having a sensitive area roughly equal to the size of one speckle, is placed in the far-field. Here, *far* means far compared to the characteristic dimensions of the measuring volume (approximately 100 μm). The detector area is generally reduced by a pinhole lens system (Chu 1991). The signal registered is proportional to the fluctuating intensity and is fed to a correlator which constructs its time correlation function. Mathematically, this autocorrelation function is,

$$G(\tau) = \langle I(0)I(\tau) \rangle. \quad (3.2)$$

This means that the intensity at an arbitrary time 0 is multiplied with the intensity a short delay time τ later. The brackets denote averaging over time. Thus, the autocorrelation function is a measure for the rate at which the signal fluctuates. See appendix 3.B for more details on autocorrelation. Intuitively, it is plausible that small particles will show fast fluctuations and therefore a rapidly decaying autocorrelation function. Large particles diffuse slower, show relatively slow intensity fluctuations and a slowly decaying autocorrelation function. It will be shown in the following sections that the decay constant of the measured autocorrelation function is directly related to the diffusion coefficient of the Brownian particles in the measuring volume.

Under the conditions i) that the scattering volume contains a large (>100) number of particles (*Gaussian approximation*), ii) the particles are much smaller (about 100 times) than the characteristic size of the scattering volume and (iii) that, given enough time, the particles can diffuse throughout the dispersion (the system is *ergodic*), the measured time intensity autocorrelation function can be related to the electric field autocorrelation function by the Siegert relationship:

$$G(\tau) = \langle I(0)I(\tau) \rangle = \langle I \rangle^2 \left(1 + A \frac{\langle E(0)E^*(\tau) \rangle^2}{\langle I \rangle^2} \right). \quad (3.3)$$

Here, A denotes an instrumental factor in the order of 1, which is related to the number of coherence areas probed, and the asterisk $*$ denotes the complex conjugate.

gated. This is dependent on optical geometrics of the setup, which is further explained in appendix 3.A. The factor $\langle I \rangle^2$ can be found from the average light intensity (*calculated baseline*) or from the value of the autocorrelation function found after long delay time τ . It is then called the *measured baseline*. In ideal circumstances both baselines are equal:

$$\langle I(0)I(\tau) \rangle_{\tau \rightarrow \infty} = \langle I \rangle \langle I \rangle = \langle I \rangle^2. \quad (3.4)$$

Since,

$$\langle I(0)I(\tau) \rangle_{\tau \rightarrow 0} = \langle I(0)^2 \rangle = \langle I^2 \rangle, \quad (3.5)$$

it is clear that the autocorrelation function decays from $\langle I^2 \rangle$ to $\langle I \rangle^2$ (see fig. 3.2).

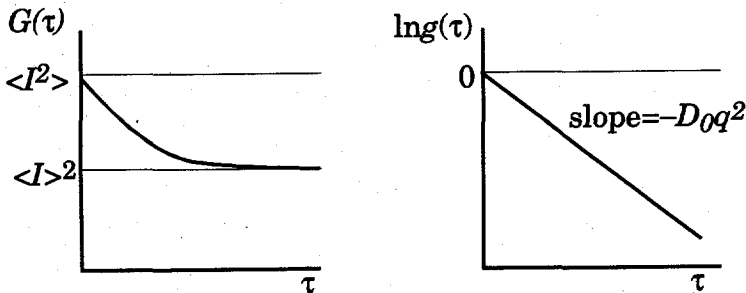


Fig. 3.2. The autocorrelation function $G(\tau)$ decays exponentially from $\langle I^2 \rangle$ to $\langle I \rangle^2$. The logarithm of normalized autocorrelation function $g(\tau)$ is for monodisperse samples a straight line with slope $-D_0q^2$.

The square root of the second term on the right-hand side of eq. (3.3) is defined as the normalized autocorrelation function $g(\tau)$,

$$g(\tau) \equiv \frac{\langle E(0)E^*(\tau) \rangle}{\langle I \rangle}, \quad (3.6)$$

which can be rewritten with eq. (3.1) into the dynamic structure factor $S(\mathbf{q}, \tau)$,

$$S(\mathbf{q}, \tau) \equiv \frac{\sum_{j=1}^N \sum_{k=1}^N \langle \exp\{i\mathbf{q} \cdot (\mathbf{r}_j(0) - \mathbf{r}_k(\tau))\} \rangle}{\sum_{j=1}^N \sum_{k=1}^N \langle \exp\{i\mathbf{q} \cdot (\mathbf{r}_j(0) - \mathbf{r}_k(0))\} \rangle}. \quad (3.7)$$

The field (eq. 3.1) can be recognized as the amplitude of the Fourier component, having wave vector \mathbf{q} , of the refractive index fluctuations in the dispersion (or, if all particles consist of the same material, number density fluctuations). The speckle pattern therefore constitutes a section of the structure in reciprocal space, that is related to the instantaneous configuration in real space. Each speckle corresponds to a single Fourier component and PCS follows the evolution in time of its squared amplitude (Pusey 1991, 842).

For non-interacting Brownian particles the denominator in eq. (3.7), which is the static structure factor, equals 1, and the cross terms ($j \neq k$) in the numerator average and therefore cancel. Hence eq. (3.7) reduces to,

$$S(\mathbf{q}, \tau) = \langle \exp\{i\mathbf{q} \cdot (\mathbf{r}(0) - \mathbf{r}(\tau))\} \rangle, \quad (3.8)$$

where \mathbf{r} is the position coordinate of an arbitrary Brownian particle.

In order to connect the dynamic structure factor, which can be obtained from experiment, to the diffusion properties of the particles investigated, one has to realize that $S(\mathbf{q}, t)$ is the Fourier transform of the probability function $P(\Delta \mathbf{r}, t)$. This function is the probability density for a particle to undergo a displacement $\Delta \mathbf{r}$ within a time period t (Dhont 1985, Dhont 1988, Ricka 1993) and therefore, must satisfy the diffusion equation,

$$\frac{\partial}{\partial t} P(\Delta \mathbf{r}, t) = D_0 \nabla^2 P(\Delta \mathbf{r}, t), \quad (3.9)$$

where $\Delta \mathbf{r} \equiv \mathbf{r}(0) - \mathbf{r}(t)$ and D_0 the diffusion coefficient at infinite dilution (no interactions). In addition,

$$S(\mathbf{q}, t) = \int P(\Delta \mathbf{r}, t) \exp\{i\mathbf{q} \cdot \Delta \mathbf{r}\} d\Delta \mathbf{r} \equiv \tilde{P}(\mathbf{q}, t). \quad (3.10)$$

Fourier transformation of the diffusion equation gives,

$$\frac{\partial}{\partial t} \tilde{P}(\mathbf{q}, t) = -D_0 q^2 \tilde{P}(\mathbf{q}, t). \quad (3.11)$$

Therefore, the dynamic structure factor equals,

$$\tilde{P}(\mathbf{q}, t) \equiv S(\mathbf{q}, t) = \exp(-D_0 q^2 t). \quad (3.12)$$

Here, q is the length of the scattering vector,

$$q = \frac{4\pi n}{\lambda_0} \sin \frac{\theta}{2}, \quad (3.13)$$

with n the refractive index of the fluid, λ_0 the wavelength of the incoming laser beam in vacuum and θ the scattering angle.

Combining eqs (3.2), (3.3), (3.8) and (3.12) and writing τ in stead of t results in a relationship between the measured autocorrelation function and the diffusion coefficient for non interacting particles (see also fig. 3.2),

$$G(\tau) = \langle I \rangle^2 \{1 + A [g(\tau)]^2\}, \text{ where } g(\tau) = \exp(-D_0 q^2 \tau). \quad (3.14)$$

This equation plays a central role in PCS, but it is unfortunately often used when it is not allowed. Generally it can be used for submicrometer particles at extremely low concentrations (usually less than 0.01 volume percent) (De Jaeger et al. 1991). Multiple scattering, number fluctuations in the measuring volume and particle interactions are the main causes that lead to the fact that eq. (3.14) cannot be applied.

To calculate the particle size from the diffusion coefficient, the Stokes Einstein equation which is valid only for non-interacting spherical particles, is frequently used,

$$d = \frac{kT}{3\pi\eta D_0}, \quad (3.15)$$

where k denotes Boltzmann's constant, T the absolute temperature, η the fluid viscosity and d the diameter of the particle. For non-spherical particles which have a compact shape, such as cubes, the Stokes-Einstein diameter gives a good estimate of the particle 'size' which can be denoted as the spherical equivalent diameter. Of course for e.g. rods or disks these spherical equivalent diameters have little practical meaning, especially if the particles are oriented in the measuring volume due to e.g. flow or gravitation.

3.3 Analysis of the autocorrelation function

As shown in the former section (eq. 3.15), it is relatively straightforward to find the diffusion coefficient of an assembly of equally sized particles from the measured autocorrelation function. Unfortunately, in nature particle size distributions are rarely monodisperse. Therefore, the autocorrelation function consists of a sum of exponentially decaying functions, i.e. one for each size class. This is not the only complication. Due to finite measuring times, laser intensity fluctuations, small amounts of dust²⁾ in the samples and imperfections of the detection system, the measured autocorrelation function always contains noise. These two factors lead to what is known in literature as an ill-conditioned problem. In practice, this means that in principle an infinite number of particle size distributions can be fitted to the measured autocorrelation function. Only if additional information is available, such as a size range or a maximum number of modals, this number can be limited. Several methods have been developed that use additional information. This section discusses two of them: the Cumulant fit which assumes a unimodal size distribution, and CONTIN which performs a least square fit and assumes parsimony, a minimum of 'peakedness'. These two analysis methods and many more are discussed further by Chu (1991).

The cumulant method and CONTIN are discussed here, since both methods are complementary for analyzing autocorrelation functions obtained by PCS. The first gives reliable results for the average particle size for unimodal narrow particle size distributions, while CONTIN gives good estimates for bimodal or broad distributions. Furthermore, these two methods are used in the following chapters of this thesis.

3.3.1 Cumulants

Generally, for polydisperse systems, the normalized autocorrelation function $g(\tau)$ can be written as,

$$g(\tau) = \int_0^{\infty} Z(\Gamma) \exp(-\Gamma\tau) d\Gamma, \quad (3.16)$$

²⁾ In PCS, dust is the most important enemy of the experimentalist. Dust particles are solid impurities at low concentration that come from the solvent or from the air. They are usually bigger than the particles to be measured ($> 1 \mu\text{m}$). Hence, they scatter the light much better. That is why they seriously distort the measured autocorrelation function and lead to large errors in the obtained particle size distribution. Symptoms of dust are: A strongly fluctuating measured intensity, sudden jumps in the autocorrelation function and a large difference ($> 1\%$) in the measured (long time) and the calculated (average intensity) baselines.

where $Z(\Gamma)$ is the distribution function of decay rates Γ , where $\Gamma \equiv Dq^2$ (see fig. 3.2). In principle, $Z(\Gamma)$ can be recovered by inverse Laplace transformation of $g(\tau)$. As outlined in section 3.3 this is, however, impossible due to the ill-conditioning of this problem.

In PCS the most common analysis method is the cumulant analysis derived by Koppel (1972). A power expansion leads to the following equation,

$$\ln g(\tau) = -\bar{\Gamma}\tau + \frac{\mu_2}{2}\tau^2 - \frac{\mu_3}{6}\tau^3 + \dots \quad (3.17)$$

where the first cumulant is defined as,

$$\bar{\Gamma} = \int_0^{\infty} \Gamma Z(\Gamma) d\Gamma, \quad (3.18)$$

and the cumulants μ_j are,

$$\mu_j \equiv \int_0^{\infty} (\Gamma - \bar{\Gamma})^j Z(\Gamma) d\Gamma. \quad (3.19)$$

The cumulants are the exponential equivalents of the moments of the distribution. From the average decay constant, $\bar{\Gamma}$, the average intensity weighted particle size can be calculated with the Stokes Einstein equation (3.15),

$$d_{PCS,avg} = \frac{kTq^2}{3\pi\eta\bar{\Gamma}}. \quad (3.20)$$

μ_2 is related to the relative variance, the polydispersity index, $P.I.$, of the particle size distribution,

$$P.I. = \frac{\mu_2}{\bar{\Gamma}^2}. \quad (3.21)$$

The third and fourth cumulants are related to the skewness and the kurtosis of the distribution respectively. Cumulant analysis is valid for monomodal distributions with relatively small polydispersities ($P.I. < 0.1$). In general, the first cumulant can be obtained accurately, but the second cumulant is strongly influenced by noise in the autocorrelation function. Higher order cumulants can be calculated, but Koppel (1972) already pointed out that in a good measurement with a third order fit the first cumulant can be obtained within 1%, the second within 20% and nothing more than the sign of the third cumulant can be determined. Hence, the third and fourth cumulant are not useful for the reconstruction of the particle size distribution.

3.3.2 CONTIN

Since particle diameters are always positive and their number cannot be negative either, any distribution containing negative values can be discarded. This is the basis of the non-negatively constrained least-squares fitting method (NNLS). It performs a least square fit of a set of calculated particle size distributions, limited by a lower and an upper size limit, on the measured autocorrelation function. While NNLS contributes a great deal to finding the correct solution, the upper particle limit and the number of particle classes still have profound influence on the results. Therefore, more prior knowledge is needed.

Provencher (1982) considered that, besides using positive constraints, choosing the solution that yields the least amount of new information is to be preferred. This concept, known as the *parsimony principle* limits the detail obtained about the distribution function, but also discards many extreme or even non-physical solutions.

Both non-negativity and parsimony can be achieved by *constrained regularization*, which is a smoothing technique. Provencher (1982) developed a programming package, called CONTIN, which implements regularization procedures, as well as some other useful techniques.

3.4 The average particle size

As discussed in the last section it is impossible to reconstruct the exact particle size distribution from the measured autocorrelation function. Due to the ill-condition inversion, particle size distributions containing more than two or three classes, measured by PCS, always should be judged with suspicion. Generally, only an average particle size and a polydispersity index for unimodal distributions, or the position of the two peaks in bimodal distributions, can be given accurately.

Realizing this, the question remains what this average size means. This is not trivial since the data are obtained by a light scattering experiment in which Mie theory is valid for the scattering profile of the particles. Mie theory is developed for light scattering by *spherical* single particles. It is the solution of the Maxwell equations, and is therefore, generally valid (Van de Hulst 1957). Because the Mie calculations are not easy to perform it is fortunate that for particles much smaller than the wavelength of the incoming light, the scattering profile can be approximated by Rayleigh scattering. Here, the scattered intensity is not dependent on the scattering angle and the scattered intensity is proportional to the sixth power of the particle size. In PCS experiments the wavelength of the incoming laser light is usually around 500 nm, since the often used Helium Neon lasers usually generate 633 nm and Argon ion lasers 488 or 514 nm. Hence, particles with a diameter smaller than approximately 50 nm can be called Rayleigh scatterers. Finsy and De Jaeger (1991) argued that the average particle size obtained by PCS is for Rayleigh scatterers the harmonic *z*-average of the particle size distribution,

$$d_{PCS} = \frac{\sum_j n_j d_j^6}{\sum_j n_j d_j^5}, \quad (3.22)$$

where d is the diameter of the spherical particle and n_j the number of particles in size class j . This means that d_{PCS} is, for very small particles due to the sixth power in the numerator of eq. (3.22), always larger than the weight average (obtained from e.g. sieving), volume weighted average (from e.g. certain light scattering techniques) or the number average particle size (e.g. from counting particles from electron microscopy photographs).

For particles with sizes comparable to the wavelength of the incoming light, the relationship between d_{PCS} and the corresponding average becomes dependent on the refractive index of the particles, the particle diameter and the wavelength of the incoming laser light (Finsy and De Jaeger 1991).

Furthermore, by using the Stokes Einstein equation (3.15), the hydrodynamic diameter is obtained. This diameter is generally larger than the 'pure' particle di-

ameter, since in liquids, water molecules and ions attach to the particle surface and slow down its diffusion.

3.5 PCS measurements of aerosols

There is no fundamental difference in measuring in liquid dispersions or in aerosols (dispersions of droplets or particles in gases). However, in aerosols usually two problems arise. The first is that the number concentration is often too low to prevent number fluctuations in the measuring volume. This, however, can be overcome at the expense of accuracy of the particle sizes found. A method to realize this is discussed by Weber et al. (1993). They concluded that at certain combinations of number concentration, diameter and flow velocity it is possible to successfully analyze the measured autocorrelation function. They performed a fit to this measured function with the derived theoretical autocorrelation function in flowing media with number fluctuations.

The second problem is that particles dispersed in gases usually settle if their size is larger than approximately 100 nm. Therefore, they can best be probed in an upward laminar gas flow to prevent this settling. If PCS is chosen as a measuring technique, this motion results in a second decay of the normalized autocorrelation function, which is proportional to the square of the delay time (Chowdhury et al. 1984).

Mathematically the normalized autocorrelation function for monodisperse Brownian particles in a uniform translational motion perpendicular to the scattering plane gets the form,

$$\ln g(\tau) = -Dq^2\tau - \frac{v^2}{2w^2}\tau^2, \quad (3.23)$$

where v is the convective velocity of the particles and w is the laser beam waist radius. The beam waist radius can be calculated using Gaussian optics. For a lens mounted close to the laser outlet the beam waist radius in the focus of the lens is (O'Shea 1985),

$$w = \frac{1}{2}f \cdot \phi. \quad (3.24)$$

Here f is the focal length of the lens and ϕ the full divergence of the laser beam in rads. It must be stressed that eq. (3.23) is only valid for laminarly flowing assemblies of particles. Experiments showed that for submicrometer particles in water, the diffusion coefficient is largely affected by turbulent eddies. Typical for turbulence is that the decay constants found by PCS cover a much broader range compared to decay times of Brownian systems.

Comparing equations (3.17) and (3.23), it is obvious that the cumulant fit can be used to analyze autocorrelation functions obtained from flowing systems, if only the first to terms are taken into account. For a monodisperse sample in motion, the second cumulant becomes negative. Hence,

$$\mu_2 = -\frac{v^2}{w^2}. \quad (3.25)$$

For a polydisperse sample, μ_2 contains both a velocity component and a polydispersity index. However, if $|-v^2/w^2|$ is much larger than $P.I.\bar{\Gamma}$, the polydispersity

component is negligible. Thus, in this case, the cumulant fit is perfectly suitable for analyzing autocorrelation functions obtained from flowing systems. In other words, two conditions must be met: The flow must be laminar and the absolute polydispersity must be relatively small compared to the flow velocity squared over the beam waist radius squared. In gases, this can be realized easier compared to liquids, because the particles in gases have higher diffusion coefficients in gases than particles of the same size in liquids.

Chowdhury et al. (1984) defined a function in order to compare autocorrelation data in a convenient way,

$$Y(\tau) = -\frac{1}{\tau} \ln \{g(\tau)\} = Dq^2 + \frac{v^2}{2w^2} \tau. \quad (3.26)$$

Plotting $Y(\tau)$ versus τ gives a straight line with intercept Dq^2 and slope $v^2/2w^2$.

Hence, it can be concluded that the intensity weighted average diffusion coefficient of an assembly of particles in a flow can be obtained accurately from the measured autocorrelation function using standard PCS software. In addition, for small polydispersities, the particle velocity can be estimated from the correlation data.

The second step is to obtain the PCS-average particle size from the measured diffusion coefficient. Since small particles do not experience a continuum of surrounding gas molecules, since they are small compared to the gas mean free path ζ , the Stokes Einstein equation (3.15) as such cannot be used anymore. ζ can be calculated as follows (Friedlander 1976),

$$\zeta = \frac{\eta}{\rho} \sqrt{\frac{\pi M}{2RT}}, \quad (3.27)$$

where ρ is the gas density, M the gas molar mass and R the gas constant. In the free molecular regime, where the particle size is much smaller than the gas mean free path, the semi-empirical relationship between the diffusion coefficient and the particle diameter d is given by Fuchs (1964),

$$d = 2 \sqrt{\frac{1.154 kT\zeta}{6\pi\eta D}}. \quad (3.28)$$

If the particle size is much larger than the mean free path the Stokes Einstein equation is valid, and in the intermediate regime this equation is used together with the Cunningham correction factor. Expressions for this factor can be found in Fuchs (1964).

3.6 Conclusions

Photon correlation spectroscopy is a measuring technique for diffusion coefficients of submicrometer particles, which is well evaluated for diluted liquid dispersions of narrowly distributed, non-interacting spherical particles. For these samples, it is a fast and relatively accurate method to obtain from their diffusion coefficient the intensity weighted average of the hydrodynamic diameter of the dispersed particles.

For particles smaller than the incoming laser wavelength, the scattered intensity is proportional to the sixth power of their size and usually the hydrodynamic diameter is larger than the particle diameter itself, because particles in solution are

surrounded by attached water molecules or ions. Thus, PCS-diameters are generally larger than the diameters found by e.g. electron microscopy (number weighted distributions), or other light scattering techniques (surface or volume weighted distributions).

In non-ideal conditions several precautions must be taken in order to obtain reliable information about the particle size distribution. It must be stressed that only a limited amount of information, roughly two information units (e.g. average and polydispersity index, or average size and flow velocity), can be extracted from the measured autocorrelation function if no additional information on the sample is available. Often the dust contents of the samples ruins the measurement quality.

Knowing this, it is obvious that for research purposes, the experiment must be designed in such a way that the average diffusion coefficient gives the information desired from the experiment. If this is not the case, additional information on the expected particle size distribution is required.

Furthermore, it is shown in this chapter that it is possible to perform PCS experiments in laminarly flowing media which can be gases or liquids. In such systems, it is possible to extract the particle diffusion coefficient as well as an estimation of the particle velocity with the standard cumulant method.

Appendix

3.A Optics and coherence areas

When coherent light is scattered by an randomly orientated assembly of particles the far-field pattern of the scattered radiation constitutes a random diffraction or speckle pattern of dark and light regions. The area of such a region, the coherence area, can be estimated by λ^2/Ω , where λ is the wavelength of the incident light and Ω , the solid angle of the incoming beam. If several of these coherence area are projected on the surface of a detector, most of the fluctuations cannot be followed anymore, since the intensity is averaged over the total detector surface. Thus, the fluctuations of the scattered interference patterns can only be observed if the light receiving optics provide a sufficient angular resolution (fig. 3.A.1).

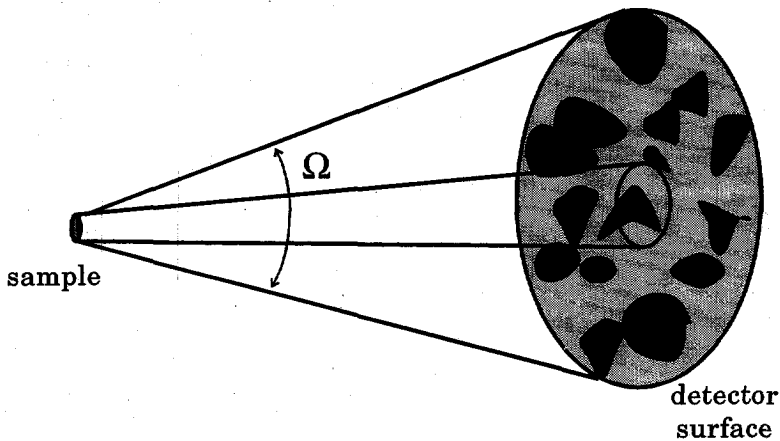


Fig 3.A.1. The diffraction pattern of the assembly of Brownian particles is projected on the detector surface, on which a fluctuating pattern of light and dark regions is formed. In order to be able to monitor the intensity changes, the detector surface or the solid angle Ω must be kept small.

Conventionally, in PCS a pinhole-lens setup (Chu 1991) is used in order to limit the number of coherence areas. The scattering volume is then determined by the detector optics and the diameter of the focused laser beam. Generally this scattering volume is only 10^{-6} cm^3 (De Jaeger et al. 1991) to achieve a typical value of about 0.6 to 0.8 for A in eq. (3.3).

Single-mode fibers with a graded index lens mounted on one of the ends can also be used as receivers for PCS measurements. In his excellent paper on this subject Ricka (1993) explained the features of these fiber optic receivers. To understand their significance for PCS measurements, one must realize that a single-mode fiber is not just a light pipe with a micrometer-sized entrance. The entrance is so small, typically $3.5 \mu\text{m}$, that it is comparable to the wavelength of visible light. Boundary conditions imposed on the electromagnetic field in a single-mode fiber are such that only a field of one certain transverse structure, only one *mode* of field is propagated. This mode is shown in fig. 3.A.2 together with two other modes which appear in multi-mode fibers.

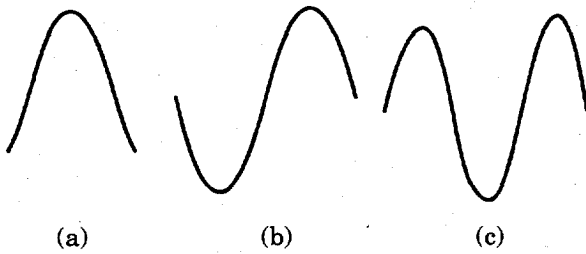


Fig. 3.A.2. In single mode optical fibers, only the zeroth order of any light source can be transmitted (a). Therefore, coherence is preserved through the optical fiber. Higher order modes contain nodes in their profiles, as shown in (b) and (c).

As a consequence, fluctuations of an external light source are perfectly correlated everywhere in the fiber cross section. Or, in other words, the propagated field is said to be perfectly transversely coherent. In conventional terms: a single mode fiber seems to select much less than one coherence area from the scattered field. Because it achieves a good angular resolution of the interference pattern, it acts as a spatial filter. As a result, A is typically larger than 0.95 in a PCS experiment with a single mode optical receiver.

Although Ricka (1993) stated that the very high signal to noise ratio does not result in a lower light collection efficiency, experiments showed that this does happen. However, for certain experiments fiber optics have great advantages, such as easy alignment, as will be shown in chapter 5.

3.B The autocorrelation procedure

Autocorrelation is a procedure to evaluate noisy signals. It can be explained using the following two figures. The digital procedure is used in all modern correlators. Usually, the delay times Δt are not linearly spaced as is shown in the example. Since exponentially decaying functions show the fastest changes at short times and decay slowly at large times, Δt increases at higher τ .

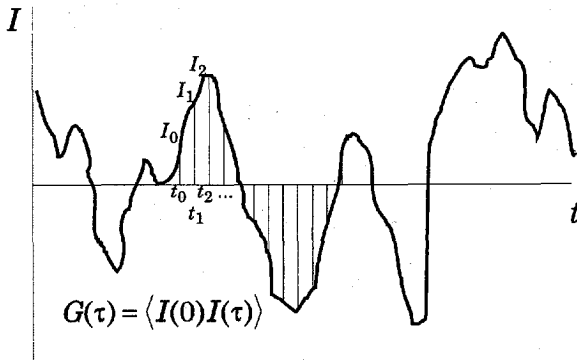


Fig. 3.B.1. The property $I(t)$, fluctuates in time as the molecules move around in the fluid. The time axis is divided into discrete intervals, Δt , and the time average $\langle I \rangle$ is assumed to be zero for convenience. The autocorrelation function is defined as $\langle I(0)I(\tau) \rangle$.

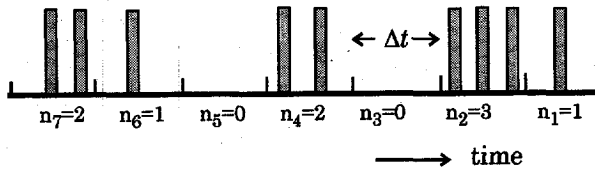


Fig. 3.B.2. Digital autocorrelation procedure: The small marks represent the sample time clock which divides time into small increments of Δt . So during time interval 2, the product $n_2 n_3 = 0$ is added to channel 1. $n_2 n_4 = 6$ to channel 2, $n_2 n_5 = 0$ to channel 3 and so on. After the multiplications the number of pulses in the count registers are shifted one place and the correlation starts again (Ford 1983).

References

- B. Berne and R. Pecora (1976) *Dynamic Light Scattering*, Wiley, New York.
- D.P. Chowdhury, C.M. Sorensen, T.W. Taylor, J.F. Merklin, T.W. Lester (1984) Application of PCS to Flowing Brownian Motion Systems, *Applied Optics*, **23**, 4149-4154.
- B. Chu (1991) *Laser Light Scattering. Basic Principles and Practice*, 2nd ed., Academic Press, San Diego.
- H.Z. Cummins, N. Knable and T. Yeh (1964) *Phys. Rev. Lett.* **12**, 150.
- J.K.G. Dhont (1985) *Light Scattering from Colloidal Systems in the Rayleigh-Gans-Debye Approximation*, Thesis Utrecht University.
- J.K.G. Dhont (1988) *Inleiding in de Statistische Mechanica van en Lichtverstrooiing aan Brownse Systemen*, Course book Utrecht University (in Dutch), 14-16.
- R. Finsy (1994) Particle Sizing by Quasi-Elastic Light Scattering, *Advances in Colloid and Interface Science*, **52**, 79-143.
- R. Finsy and N. de Jaeger (1991) Particle Sizing by Photon Correlation Spectroscopy. Part II: Average Values, *Part. Part. Syst. Charact.*, **8**, 187.
- R. Finsy, N. de Jaeger, R. Sneyers, E. Geladé, (1991^a) Particle Sizing by Photon Correlation Spectroscopy. Part III: Mono and Bimodal Distributions and Data Analysis, *Part. Part. Syst. Charact.*, **9**, 125.
- R. Finsy, L. Deriemaeker, N. de Jaeger, R. Sneyers, J. Vanderdeelen, P. van der Meeren, H. Demeyere, J. Stone-Masui, A. Haester, J. Clauwaert, W. de Wispelaere, P. Gillioen, S. Steyfkens, E. Geladé, (1991^b) Particle Sizing by Photon Correlation Spectroscopy. Part IV: Resolution of Bimodals and other Particle Sizing Methods, *Part. Part. Syst. Charact.*, **10**, 118.
- N.C. Ford (1983) Theory and practice of photon correlation spectroscopy, in: Dahneke, B.E. (ed), *Measurement of Small Particles by Quasi Elastic Light Scattering*, Wiley, New York.
- S.K. Friedlander (1976) *Smoke, Dust and Haze*, Wiley, New York, 6.
- N.A. Fuchs (1964) *The Mechanics of Aerosols*, Dover, New York, Chapter 2.
- H.C. van de Hulst (1957) *Light Scattering by Small Particles*, Wiley, New York.
- N. de Jaeger, H. Demeyere, R. Finsy, R. Sneyers, J. Vanderdeelen, P. van der Meeren, M. van Laethem (1991) Particle sizing by Photon Correlation Spectroscopy. Part I: Monodisperse Lattices: Influence of Scattering Angle and Concentration of Dispersed Material, *Part. Part. Syst. Charact.*, **8**, 179.
- D.E. Koppel (1972) Analysis of Macromolecular Polydispersity in Intensity Fluctuation Spectroscopy: The Method of Cumulants, *J. Chem. Phys.*, **57**, 4814.
- D.C. O'Shea (1985) *Elements of Modern Optical Design*, Wiley, New York, 239.
- S.W. Provencher (1982), A Constrained Regularization Method for Inverting Data Represented by Linear Algebraic or Integral Equations, *Computer Phys. Comm.*, **27**, 213.
- P.N. Pusey (1991) Colloidal suspensions, in J.P. Hansen, D. Levesque and J. Zinn-Justin (eds) *Liquids, Freezing and Glass Transition*, Les Houches, session LI 1989, North Holland, Amsterdam, 763-931.

- J. Ricka (1993) Dynamic light scattering with single-mode and multimode receivers, *Applied Optics*, **32**, 2860-2875.
- R. Weber, R. Rambeau, G. Schweiger, K. Lucas (1993) Analysis of a Flowing Aerosol by Correlation Spectroscopy: Concentration, Aperture, Velocity and Particle Size Effects, *J. Aerosol Sci.*, **24**, 485.
- B.B. Weiner (1992) Twenty Seven Years of QELS: A Review of the Advantages and Disadvantages of Particle Sizing with QELS, in N.G. Stanley-Wood and R.W. Lines (eds) *Particle Size Analysis*, The Royal Society of Chemistry, Cambridge, 173-185.
- H. Wiese and D. Horn (1991) Single-mode fibers in fiber-optic quasielastic light scattering: A study of the dynamics of concentrated latex dispersions, *J. Chem. Phys.* **94**, 6429.

Cluster formation in concentrated solutions¹⁾

Abstract

This chapter discusses investigations on aqueous solutions of citric acid, potassium nitrate and sucrose at high solute volume fractions and low supersaturation or at undersaturation by means of photon correlation spectroscopy. Not nucleation, but the formation of small clusters of molecules or ions is the subject. From the time dependence of the scattered light the collective diffusion coefficient was obtained. Interactions between the solute molecules resulted in a concentration dependence of the diffusion coefficients. From this, the attractive interaction parameter has been estimated. It appears that strong attractive forces between the molecules play a dominant role in the solutions of sucrose and citric acid. Even below the saturation concentration clusters of 2-3 molecules develop. They are much smaller than the critical cluster size of crystalline sucrose and citric acid. The clusters are presumed to be aggregates of solute molecules which are not precursors of the crystalline compounds, but form a different phase. Alternatively, solute molecules might be forced into small clusters by surrounding water molecules. Potassium nitrate appears not to form clusters, since the diffusion coefficient does not change significantly as a function of concentration.

Neutron diffraction experiments of deuterated citric acid in heavy water give qualitative support for the formation of clusters in solution. The intensity spectrum shows a 'shoulder' at short q -values, which is attributed to larger scattering units which can be clusters.

4.1 Introduction

As has been described in chapter 2, cluster formation is the first step in most crystallization studies. The reader is referred to this chapter for the theory behind cluster formation and nucleation. This chapter discusses systems at high concentration, but at low supersaturation or undersaturation. Thus, no nucleation occurred and measurements were often performed in metastable conditions, where the samples were supersaturated, but did not crystallize yet.

Many earlier attempts have been made to actually measure the formation of clusters in concentrated solutions, as is summarized in the next subsection.

Earlier work

Measurements of concentration gradients in vertical columns (Ginde and Myerson 1992) and measurements of obscuration (Kamskii 1989) indicate that subcritical clusters exist in supersaturated aqueous solutions of well soluble compounds such as urea and citric acid. Raman spectroscopy has shown that a structure develops in concentrated solutions of potassium nitrate (Hussmann et al. 1984) and dihydro-

¹⁾ Parts of this chapter have been published in the *Journal of Crystal Growth*. The full reference is: M.A. van Drunen, R. Finsy, H.G. Merkus, B. Scarlett and G.M. van Rosmalen (1993) Measurements of Cluster Formation in Aqueous Citric Acid Solutions by Photon Correlation Spectroscopy, *J. Crystal Growth*, 134, 196-202.

gen orthophosphates (Cerreta and Berglund 1987), and interferometric techniques have shown the same for concentrated solutions of urea (Sorrell and Myerson 1982).

The aim of this study is to seek evidence of cluster formation in aqueous citric acid solutions by probing its microscopic properties. Citric acid was chosen because it was also used by Ginde and Myerson (1992) for macroscopic measurements of density gradients in vertical columns. The measuring technique used here was photon correlation spectroscopy (PCS) which measures the light scattered by an assembly of dispersed particles as a function of time. Thus, it yields information on the microscopic dynamics of the system. This has been explained in detail in chapter 3. Using this technique, an average cluster size has been determined by investigating the dependence of the measured diffusion coefficient of the clusters on the concentration of citric acid. The experiments are described in section 4.4.

PCS together with static light scattering was also used by Bilgram and co-workers (Steiniger and Bilgram 1991) in order to study the solid-melt interface layer of several organic compounds as well as water. They found evidence for weakly bonded aggregates at the liquid side of the interface. However, they studied crystal growth from the melt. Here, we focus on cluster formation in stable or metastable solutions.

Our investigations included the influence of an additive on the cluster size. An interaction between calcium ions and citric acid in solution is suggested by nuclear magnetic resonance (NMR) studies (Vijverberg et al. 1980). Thus, calcium chloride was added to the citric acid solutions. Citric acid molecules coordinate, the calcium ions, which may lead to a different cluster size. In theory, the calcium ions can act as templates to form new clusters or they can withdraw the citric acid molecules from the clusters.

Neutron scattering

Structure in liquids and solutions can also be investigated by measuring the elastic scattering of thermal neutrons because the typical spaces between particles in liquids are in the same range as the wavelength of thermal neutrons (Hansen and McDonald 1976). In order to find more evidence for cluster formation in concentrated citric acid solutions, neutron diffraction measurements were performed at the Interfacultair Reactor Instituut (IRI) in Delft. Because hydrogen atoms yield a high *incoherent* background scattering intensity, which deteriorates the signal to noise ratio, heavy water (deuterium oxide) was used and partly deuterated citric acid instead of water and normal citric acid.

Sucrose and potassium nitrate

Experiments were also done with sucrose, to show that the PCS method to determine cluster size is not restricted to citric acid (fig. 4.1) alone, but is useful for other concentrated systems as well. For the same reason, potassium nitrate was chosen as a model compound. Although this compound is well soluble, the solutions are far less viscous, indicating that on a molecular scale, interactions are less strong.

Dynamics of sucrose solutions were investigated by Brown et al. (1994). They found a sudden decrease of the relative partial molar enthalpy of water in sucrose (fig 4.1) solutions if the molar ratio water to sucrose approaches the value 8. Physically, at this point the number of water molecules per sucrose molecule is insufficient to coordinate with all the hydroxy groups. Brown and co-workers suggested that 'clustering' of sucrose is a consequence of this limited hydration rather than

any intrinsic attraction between sucrose molecules. It is also possible that water molecules are simply trapped between sucrose molecules [...].

In this work, PCS experiments were done in order to investigate whether cluster formation can also be observed by following the dynamics of sucrose solutions.

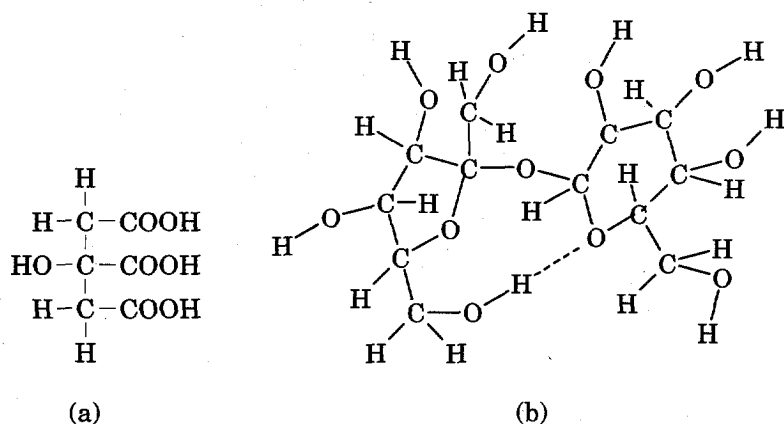


Fig. 4.1. Molecular formula of citric acid (a) and structure of sucrose (b). Sucrose is built up out of fructose (left ring) and glucose (right ring). It has 8 OH groups which can coordinate with water (Brown et al. 1994). For simplicity, no convention concerning chirality has been adopted.

Scope

The diffusion coefficients measured as a function of citric acid concentration are discussed in section 4.4, along with the influence of calcium ions and the supersaturation on the magnitude of the diffusion coefficients. In addition, the neutron scattering experiments and the results of the PCS measurements on sucrose and potassium nitrate are discussed. Finally, in section 4.5 conclusions are drawn.

4.2 Theory

4.2.1 Theory of cluster formation

The size distribution of clusters in supersaturated solutions has been derived in chapter 2 in sections 2.3.2 and 2.3.3. The steady state cluster size distribution $Z(n)$ (eq. 2.35) has been calculated for citric acid at supersaturations rating from 1.3 to 1.9. The clusters were assumed to be spherical and σ was taken to be 20 mJ/m² (Larson and Garside 1986). The transition frequency $f(n)$ was assumed to be constant in the n -range that determines the average cluster size ($n < 20$). The saturation concentration of citric acid is:

$$C_{sat} = \left(\frac{1}{0.5182 + 0.005748T} - 1 \right)^{-1} \quad (4.1)$$

C_{sat} is in g hydrated citric acid ($C_6H_8O_7 \cdot H_2O$) / g water and T is in °C (Mullin and Leci 1969). $Z(n)$ rapidly approaches zero as the number of molecules in a clusters

increases as can be seen in fig. 4.2. It will be clear that homogeneous nucleation at these low supersaturations is not likely to occur, since the concentration of the clusters approaching the homogeneous critical cluster size is extremely low.

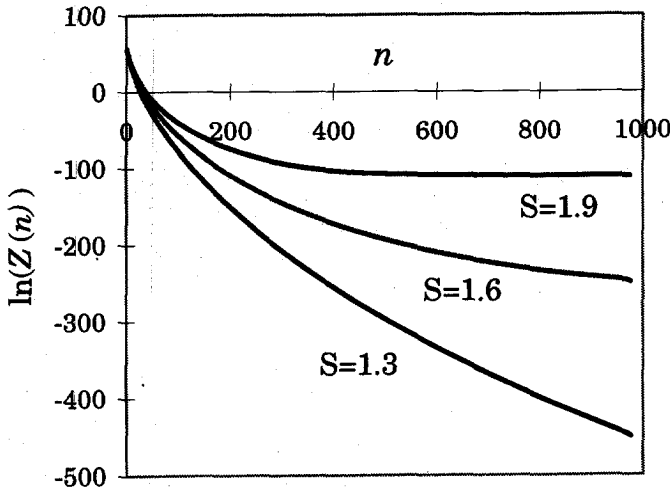


Fig. 4.2. Calculated concentration of citric acid clusters as a function of n (eq. 2.35) at supersaturations $S=1.3$, 1.6 and 1.9 . Note the logarithmic vertical scale. The critical cluster size is 7826, 1361 and 534 molecules, respectively.

The values for $Z(n)$ and the average number of molecules in a cluster (eq. 2.36) have been calculated numerically using the program Xplore. The calculated average cluster sizes are shown in fig. 4.3. The average values are low, because most of the molecules appear as monomers in the solution. Thus, by calculating the number average, the influence of dimers, trimers, etc., is rather limited. Of course, the scattered light intensity average (eq. 3.22) will show a more pronounced influence of the clusters.

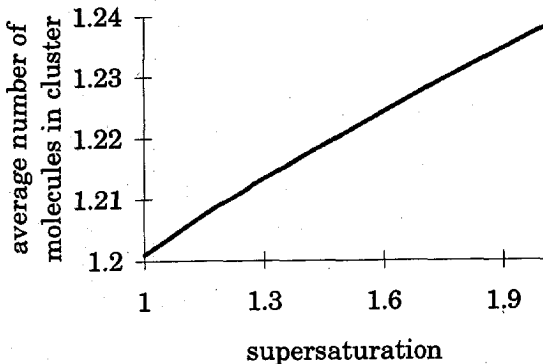


Fig. 4.3. Average number of citric acid molecules in a cluster, calculated using eq. (2.37).

4.2.2 PCS in concentrated systems

For concentrated systems, such as the system studied here, the diffusion coefficient is affected by particle-particle interactions and cannot be related to the particle size using the Stokes-Einstein equation. For interparticle distances which are small compared to the reciprocal scattering vector q^{-1} , PCS probes the collective diffusion coefficient D_C (Pusey 1991). Basically, two types of interactions affect D_C : attractive and repulsive ones. In the presence of the former D_C will decrease with concentration, whereas the latter will increase D_C . At zero concentration $D_C = D_0$. The effect of repulsive and attractive interactions can be approximated by a one parameter model. A model which assumes hard spheres and attractive interactions, quantified by an attraction parameter α , yields (Finsy et al. 1980, Finsy 1990),

$$D_C = D_0[1 + (1.45 - 0.56\alpha)\phi]. \quad (4.2)$$

The parameter ϕ is the volume fraction of the dispersed particles and the product $\alpha\phi$ can be interpreted as the average number of particles which surround another particle (coordination number). The coordination number can now be used to estimate the cluster size of the dispersed particles,

$$n(\phi) = \alpha\phi + 1. \quad (4.3)$$

In this derivation, the long-range repulsive forces have been neglected. For long range repulsive interactions, such as electrostatic interactions, eq. (4.2) can be modified as follows (Finsy et al. 1980, Finsy 1990),

$$D_C = D_0\{1 + [8(1 + \beta)^2 - 6(1 + \beta)^2 - 0.56\alpha]\phi\}. \quad (4.4)$$

The term β is a repulsive interaction parameter. In this model the effect of the repulsive interaction is approximated by an effective hard sphere interaction of range $d(1 + \beta)$, where d is the hard sphere diameter. As a first approximation $d\beta$ represents the distance, measured from the particle surface, at which the repulsive potential is comparable to the thermal kinetic energy of the particles. Thus, at a distance $d(1 + \beta)$ from the particle center the kinetic energy cancels, on the average, the effect of the repulsive interaction.

For particles which have sizes only slightly larger than the solvent molecules the normal Stokes Einstein equation needs to be modified. Rutten (1992) found for diffusion of polar organic compounds in water that,

$$D_0 = \frac{kT}{1.74\pi\eta d_j} \left(\frac{d_w}{d_j} \right), \quad (4.5)$$

where d_w is the diameter of a water-water cluster containing 2 molecules and d_j is the diameter of a solute molecule. Dimers of water are chosen because this appears to be a good description of the water diffusion behavior. The factor 1.74 is obtained from analyzing a large set of measured diffusion data. The diameter of the solute molecule is calculated from its volume increased with the volume of hydrogen bonded water molecules.

4.2.3 Neutron scattering

Thermal neutrons, with a wavelength in the order of 0.1 nm, can be used to determine the structure in condensed materials. The technique is complementary to X-

ray diffraction, because the scattering intensity is not determined by the electron density of the atoms involved as with X-ray scattering. Instead, neutrons interact with atomic nuclei via the very short-ranged strong nuclear force. Therefore, the scattering intensity is dependent on the nuclear spin state of the atoms involved. This nuclear spin state does not increase with the atomic number, but is randomly spread through the periodic table. For the experiments described here, it is important to know that deuterium, oxygen-16 and carbon-12 scatter thermal neutrons moderately well, and that hydrogen-1 incoherently, and thus independently of scattering angle, scatters thermal neutrons.

The measured property of a condensed sample is the static structure factor $S(q)$, the time independent equivalent of eq. (3.6). Here, $q = 4\pi/\lambda \sin \frac{1}{2}\theta$. The inverse Fourier transform of $S(q)$ gives the radial distribution function $g(r)$. $g(r)$ represents the probability density as a function of the distance from the center of a scattering entity. Thus for a crystal it shows sharp peaks at the lattice distances. In liquids smooth peaks appear at the average distance between the molecules.

In a crude approximation (De Schepper 1994), the first peak in the structure factor can be attributed to the particle size. Hence, this first peak provides information about cluster formation in solutions. The basis for this is that two particles cannot overlap, and that thus $g(r) = 0$ for $r < d$. This results in a peak in $S(q)$ at

$$q \approx \frac{2\pi}{d} \quad (4.6)$$

Information long range ordering and detailed information about the local structure around atoms can be obtained if the q -range which is probed is large enough to permit inverse Fourier transformation, or if a model is available which describes the structure well. Then, the calculated $S(q)$ can be compared with the measured one and parameters in the model can be adjusted. Unfortunately, these models are only available for spherical particles such as e.g. liquid argon molecules. Hence, in this work, only the first peak position of $S(q)$ is quantified.

4.3 Materials and methods

4.3.1 PCS-experiments

Citric acid

Aqueous solutions of citric acid monohydrate (Lamers en Pleuger, and Baker; the Netherlands) were studied in a system thermostated at 25°C. The solutions had been filtered through a 0.2 μm disposable filter at 30-40°C. The samples were allowed to equilibrate for at least one hour. The spectrometer was a Brookhaven Instruments BI-200SM and the correlator a Brookhaven Instruments BI-8000. Measurements of a saturated solution within an angular range of 20 to 90° with a 100 mW Ar⁺ laser power did not show a difference in the measured diffusion coefficient as a function of scattering angle. Thus an angle of 30° was selected because at small angles the scattered intensity is higher and the decay is slower (chapter 3). At a slower decay rate the sample time does not need to be very short and the measured autocorrelation function suffers less from afterpulsing effects from the photomultiplier tube (Ford 1983). Nevertheless, the content of the first

channel ($\langle I(0)I(0.5\mu s) \rangle$) was omitted in the calculations. The scattered intensity was 4,000 to 6,000 counts per second. Typically 20-60 repeated measurements, each of 10 minutes duration, were made on each sample. The autocorrelation functions of these different measurements were added, while those suffering notably from scattering by dust particles were discarded. This error could be identified as such from the absolute values and from the differences of the measured and calculated baselines of the autocorrelation functions. The total measuring time was about 6 hours for each concentration selected. The wavelengths used were 457.9 and 488 nm. At these wavelengths, the solutions do not absorb light.

Solutions were prepared solely with water and with a 11.6 mg/l and a 50.6 g/l aqueous CaCl_2 -solution (Merck). The molar ratio citric acid: Ca^{2+} is then approximately $10^8:1$ and $10^4:1$ respectively.

The saturation concentration in citric acid solutions strongly depends on the temperature as can be seen from eq. (4.1). To investigate whether the diffusion coefficient depends on the supersaturation or only on the concentration, additional experiments were done with the same sample that contained 2.0 g citric acid monohydrate /g water at $T=20, 30$ and 35°C . The supersaturation for these temperatures were 1.16, 0.90 and 0.78, respectively. The diffusion coefficients obtained were adjusted for the different temperatures and viscosities to those at 25°C using,

$$D_C \propto \frac{T}{\eta} \quad (4.7)$$

Sucrose and potassium nitrate

Sucrose is even better soluble than citric acid: the equilibrium concentration at 25°C is 2.0595 g/g water (interpolated from Freier 1987). The concentrations used in our experiments varied from 0.22 to 2.6 g/g. Sucrose was obtained from Baker in the Netherlands. The PCS measurements were done at 25°C and at $\theta = 30^\circ$, while the laser wavelength was 488 or 457.9 nm.

Potassium nitrate has a saturation concentration of 3.3045 mol l^{-1} (approximately 0.33 g/g) at 25°C (interpolated from Narayanan and Youngquist 1987). Several PCS measurements were done at $20\text{-}25^\circ\text{C}$, and at $\theta = 25$ or 30° , while the laser wavelength was 488 nm. Concentrations investigated were around 0.33 g/g. The measuring procedures for sucrose and potassium nitrate were the same as for citric acid.

4.3.2 Neutron diffraction

The liquids neutron diffraction ('VD'²⁾ set up at the IRI has been used for our experiments. The sample cell was made of two parallel quartz plates of 25 x 60 x 1 mm, 2 mm separated from each other. The cell was placed in the neutron beam at an angle of 45 degrees, so at $\theta=45^\circ$ the neutron beam followed the shortest path to the detector (fig. 4.4). The beam shape was formed by boron and cadmium plates to a rectangle of 40 mm high and 10 mm wide, except for the transmittance measurements where it was a 1 mm diameter circle. Here, the cell was placed perpendicular to the beam. The transmittance is needed to calculate the correction factors for self

²⁾ VD stands for Vloeistof Diffractometer, the Dutch words for liquids diffractometer.

shielding as shown in the appendix. The wavelength of the neutron beam was 0.131 nm.

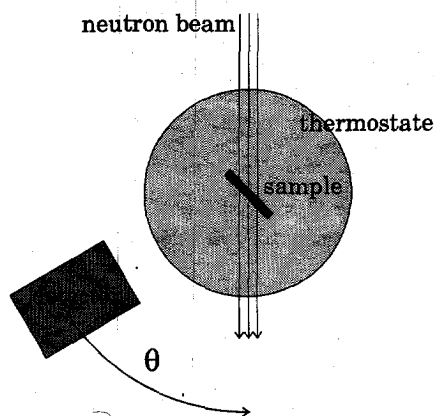


Fig. 4.4. Schematic view of the neutron scattering setup.

The cell was placed in a cylinder made of aluminum, which is nearly transparent for neutrons, with a coil in it containing water for cooling or heating. The temperature was controlled with a thermostat bath within 0.1°C and the temperature was measured with a thermocouple.

Firstly, the transmittance of the cell, the heavy water and the deuterated citric acid solution were measured by monitoring the difference in intensity with and without the sample.

Secondly, the scattering of the empty cell and the cell filled with heavy water was measured as a function of scattering angle. Finally the scattering of the deuterated citric acid solutions in heavy water was monitored at different temperatures and hence at different supersaturations. The angular range was $5\text{-}135^{\circ}$ with respect to the outgoing beam.

The deuterated citric acid solution was obtained as follows: Citric acid mono hydrate (Lamers en Pleuger, The Netherlands) was dissolved in deuterium oxide (99.8% D, Janssen Chimica, Belgium). A rapid exchange of acid and hydroxy H-atoms with deuterium oxide D-atoms takes place. In citric acid at the concentrations investigated the exchangeable *H:D*-ratio was about 1:10. After dissolving the D_2O was evaporated at 0.02 bar and 60°C . At $T > 36^{\circ}\text{C}$ the water free citric acid crystallizes (Freier 1987). This procedure was repeated 5 or 6 times to exchange most of the acid and hydroxy *H*-atoms by *D*-atoms. The more H-atoms are exchanged the less the attenuation of neutrons will be and the higher the signal to noise ratio in the scattering experiments will be.

4.4 Results and discussion

4.4.1 PCS measurements in citric acid

Some of the normalized measured autocorrelation functions $g(\tau)$ are shown on a semi-logarithmic scale in fig. 4.5. Since the horizontal axis is given in τq^2 units, the

slopes of the functions are directly related to the (cluster) diffusion coefficient distribution. The diffusion coefficients measured are shown in table 4.1. The intensity weighted average diffusion coefficients were obtained from the initial slopes of the autocorrelation functions by the method of cumulants (see chapter 3, eq. 3.17), which is implemented in the correlator software.

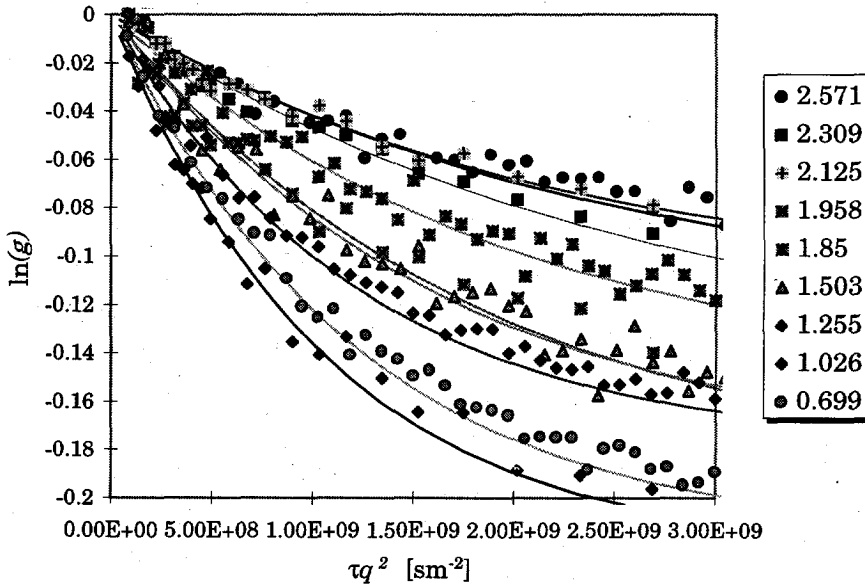


Fig. 4.5. Measured normalized autocorrelation functions of citric acid solutions with the cumulant fits (lines). The initial slopes of the lines are proportional to the diffusion coefficient; $q=9.47 \mu\text{m}^{-1}$. The legend gives the concentrations in gram citric acid monohydrate per gram water.

This method gives essentially an average decay constant of the autocorrelation function, which is directly related to the average collective diffusion coefficient D_C , and a polydispersity index, which is the relative variance of the intensity weighted diffusion coefficient distribution for low concentrations. The increase of this index with concentration can be caused by a broadening of the distribution, but also by non-Gaussian behavior of the particle movement as has been reported by others who measured at these high volume fractions (Wiese and Horn 1991). Here, non-Gaussian refers to the fact that particles cannot diffuse throughout the measuring volume during the total measuring time. The results are summarized in table 4.1 and fig. 4.6. The confidence intervals have been estimated from the cumulant fit quality.

Table 4.1. Calculated, intensity weighted, average diffusion coefficients (D_C) and polydispersity indices (P.I.) of the citric acid particles in water at different concentrations. The diffusion coefficients are adjusted to the temperature, $T=25^\circ\text{C}$. The water free citric acid density is 1.665 g/cm^3 . ϕ is the volume fraction and S the supersaturation. The errors are given for a 95% confidence interval. D_0 is found from the extrapolation to $\phi=0$ in fig. 4.6.

C [g/g]	ϕ	S	D_C [$10^{-10}\text{m}^2\text{ s}^{-1}$]	D_C/D_0	err (%)	P.I.
0.699	0.266	0.357	4.5	0.55	5.3	0.3
1.026	0.341	0.524	5.2	0.62	14.5	0.3
1.255	0.384	0.641	4.4	0.53	5.6	0.3
1.503	0.422	0.768	3.4	0.41	17.6	0.3
1.850	0.467	0.945	2.7	0.33	10.5	0.2
1.958	0.479	1.000	3.0	0.36	14.2	0.4
2.125	0.497	1.085	2.2	0.27	10.8	0.4
2.309	0.514	1.179	2.1	0.25	11.5	0.4
2.571	0.536	1.313	2.4	0.29	8.2	0.4
Ca²⁺ 1.6 mg/l						
1.170	0.369		3.8	0.45		0.4
1.700	0.449		1.9	0.23		0.5
2.000	0.484		1.8	0.22		0.6
2.205	0.505		1.7	0.20		0.4
Ca²⁺ 50.6 g/l						
1.706	0.450		2.1	0.25		0.5
2.020	0.486		2.2	0.26		0.4
T-exp (20, 30 en 35°)						
2.004	0.484	1.161	2.1	0.26		0.4
2.004	0.484	0.898	2.7	0.32		0.4
2.004	0.484	0.782	2.3	0.28		0.5

Volume fraction

The volume fraction is the volume of the citric acid molecules relative to the total volume of the sample. It can be calculated as follows if the volumes of water and citric acid are assumed to be additive,

$$\phi = \frac{C}{\rho_{Ci}} \frac{M_{Ci}}{M_{Ci \cdot H_2O}} \left(\frac{C}{\rho_{Ci}} \frac{M_{Ci}}{M_{Ci \cdot H_2O}} + \frac{C}{\rho_{H_2O}} \frac{M_{H_2O}}{M_{Ci \cdot H_2O}} + \frac{1}{\rho_{H_2O}} \right)^{-1}, \quad (4.8)$$

where C is the mass concentration (g citric acid mono hydrate/g water), M_{Ci} is the molecular weight of citric acid (192 g/mol), $M_{Ci \cdot H_2O}$ the hydrate molecular weight (210 g/mol), ρ_{Ci} the density of citric acid anhydrate (1.665 g/cm^3 (Landolt-Bornstein 1991)) and ρ_{H_2O} the water density. The average distance between the solute molecules can be estimated from,

$$x = \left(\frac{\phi}{\frac{1}{6} \pi d^3} \right)^{\frac{1}{3}} \quad (4.9)$$

In this system x is always smaller than 1 nm, much smaller than the inverse scattering vector q^{-1} ($\approx 0.1 \mu\text{m}$). Therefore, the collective motion of a large number of small particles is probed by PCS and the measured diffusion coefficient is the collective diffusion coefficient. As a result this diffusion coefficient cannot be related to the cluster size by the (modified) Stokes-Einstein equation (d_j in 4.5), but must be estimated from the attraction parameter, α , as defined by eq. (4.2) or (4.4).

Interactions

For solutions of citric acid molecules two kinds of interactions are to be expected: Electrostatic repulsive interactions between neighboring citrate ions and attractive Van der Waals interactions. The collective diffusion coefficient D_C is increased by repulsive interactions with increasing concentration and decreased by attractive interactions (Finsky 1990). The observed decrease of D_C with concentration, shown in fig. 4.6, already demonstrates that the effect of attractive interactions, which are responsible for the formation of citric acid clusters, is predominant in this system.

The observed decrease of D_C can be fitted by:

$$D_C = D_0(1 + k_d \phi), \quad (4.10)$$

with $D_0 = 8.3[\pm 0.9] \cdot 10^{-10} \text{m}^2/\text{s}$ and the interaction parameter $k_d = -1.38[\pm 0.25]$. Its negative value already indicates that attractive forces play an important role. D_0 can be related to the hydrodynamic diameter d_H by the modified Stokes-Einstein equation (d_j in 4.5). In this manner a value of $0.70[\pm 0.04]$ nm was obtained for d_H , where the number of coordinating water molecules had to be taken zero in order to match the diffusion coefficient obtained. Otherwise, the size would be unrealistically small. This suggests that intramolecular hydrogen bonds dominate in citric acid molecules at these high concentrations.

The derived size corresponds well to the molecular size of citric acid which can be obtained from a space filling model. In its energetically most favorable conformation its longest dimension is 0.8 nm and its shortest is about 0.4 nm, thus its corresponding hydrodynamic sphere diameter can credibly be 0.7 nm. Clearly for infinite dilution the cluster is just one molecule.

Cluster size

In order to estimate the cluster size at finite concentration the value of the parameter α must be calculated from k_d . Eq. (4.2) gives for the attraction parameter α the value 5. Thus, the values of the product of α and ϕ are between 1.5 and 2.5 in the ϕ -range investigated. Hence, a clusters consist of 2 to 4 molecules (eq. 4.3), depending on the volume fraction. The corresponding cluster size is then 0.9 to 1.2 nm if it is assumed to be spherical. This is smaller than most of the values from vertical column experiments obtained by Ginde and Myerson (1992), who found cluster sizes of 4 to 107 molecules, depending on the temperature and supersaturation. Repulsive

interactions would increase the cluster size found from our experiments, as can be derived from eq. (4.4). However, it is difficult to estimate a reliable value for β^3 .

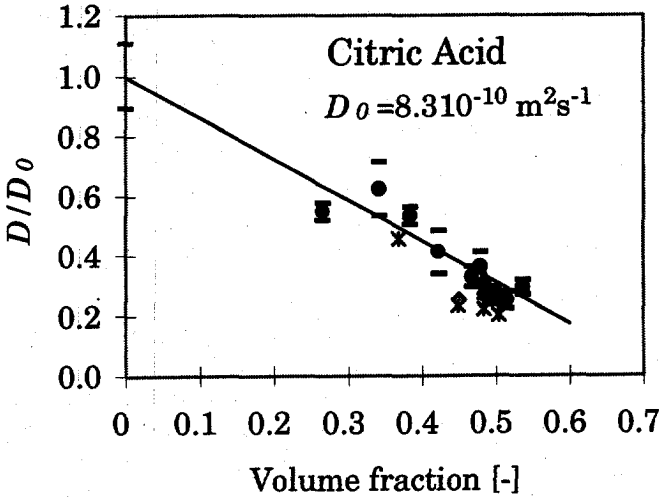


Fig. 4.6. Measured relative diffusion coefficients (●) with error bars (-) and calculated first order fit as function of the volume fraction, $\alpha=5$. Legend: $x=11.6$ mg/l and $\diamond=50.6$ g/l Ca^{2+} in water as solvent. Δ : measured points at different temperatures and different supersaturations $S=0.78-1.16$. The horizontal bars denote the statistical error ranges (95% confidence interval).

Fig. 4.6 also shows that calcium ions do not influence the cluster size significantly at the concentrations investigated. The diffusion coefficients tend to be somewhat lower but not significantly.

If the diffusion coefficients measured at different temperatures are corrected for the temperature and the viscosity using eq. (4.7), they have nearly the same value. This can have three causes. Firstly, the volume fraction rather than the supersaturation can be the variable controlling the diffusion coefficient, but this is not supported by the theory outlined in chapter 2.

The second cause can be that the clusters form a different 'phase' compared to crystalline citric acid. Since the average cluster size is much larger than the value expected from the steady state cluster size distribution (fig 4.3), the molecules in the clusters experience another supersaturation than crystalline citric acid molecules. In addition, this experienced supersaturation appears not to be temperature dependent, where the supersaturation for crystalline citric acid is strongly temperature dependent. Thus, it can be concluded that these cluster citric acid molecules have different properties compared to crystal citric acid molecules and that the clus-

³⁾ The estimation for β done in our paper (*J. Crystal Growth* (1993) 134, 196) was based on the non-modified Stokes-Einstein equation. The use of the modified equation, as was done here, results in more realistic relationships between d and D , but if β would be estimated with the thus obtained value for d and the method described in the paper, it would be 0 for citric acid and even get non-physical negative values for sucrose.

ter state can therefore be called a distinct phase, which is not likely to be some intermediate state between the crystalline and dissolved phase.

The third option is that limited hydration or entrapment of water molecules are the cause of cluster formation, as has been suggested by Brown et al. (1994) (see section 4.1).

The formation of a structure that is neither crystalline nor dissolved as monomers, is also found in aggregation of orthophosphates (Ceretta and Berglund 1987) and in aggregation of proteins (Georgalis et al. 1993), where aggregates are found that do not form a precursor of a crystalline phase. Ohgaki et al. (1993) found evidence for heterogeneity in citric acid solutions by investigating rapidly frozen samples of solutions by transmission electron microscopy. This heterogeneity could have been caused by aggregation of solute molecules.

4.4.2 PCS measurements in sucrose and potassium nitrate solutions

Sucrose

The PCS experiments for sucrose (fig. 4.7) were treated in the same way as for citric acid. Thus, a plot was constructed with the relative diffusion coefficient against the volume fraction (fig. 4.8). The errors for sucrose are smaller, probably because the concentration was higher and the molecules are larger compared to citric acid molecules. This results in a higher scattered light intensity, and therefore, in less noisy autocorrelation functions.

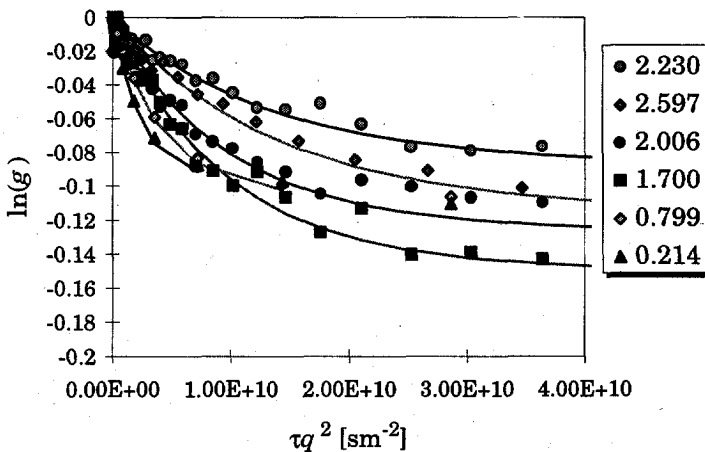


Fig. 4.7. Measured normalized autocorrelation functions for sucrose solutions, together with the cumulant fits (lines). The legend shows the sucrose concentration in gram sucrose per gram water.

Table 4.2. PCS-results of the sucrose experiments. Calculated, intensity weighted, average diffusion coefficients (D_C) and polydispersity indices (P.I.) of the sucrose particles in water at different concentrations. The sucrose density is 1.574 g/cm^3 .

C [g/g]	ϕ	H ₂ O/Suc	S	$D_C [10^{-10} \text{m}^2 \text{s}^{-1}]$	D/D_0	err (%)	P.I.
0.214	0.119	88.8	0.104	2.2	0.85	3.6	0.3
0.799	0.337	23.8	0.388	1.2	0.49	4.7	0.3
1.700	0.519	11.2	0.825	0.55	0.22	9.5	0.4
2.006	0.560	9.5	0.974	0.55	0.21	14.6	0.4
2.230	0.586	8.5	1.083	0.39	0.15	16.9	0.4
2.597	0.623	7.3	1.261	0.37	0.15	12.9	0.4

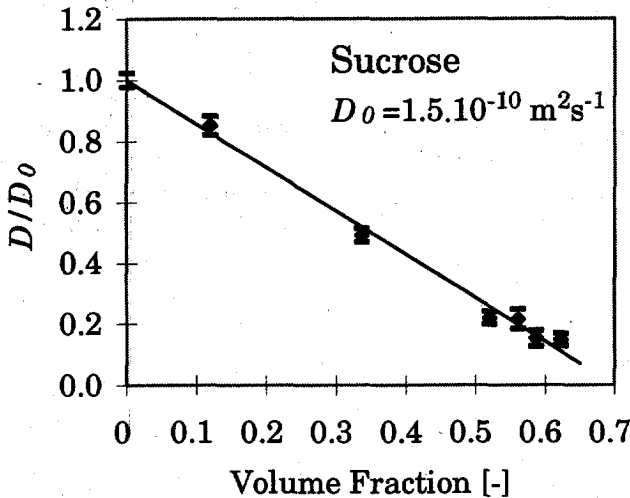


Fig. 4.8. Measured relative diffusion coefficients and calculated first order fit as function of the volume fraction for sucrose, $\alpha=5$.

For sucrose D_0 was found to be $2.5[\pm 0.1] \cdot 10^{-10} \text{ m}^2 \text{ s}^{-1}$ from the intercept, and for interaction parameter k_d $-1.43 [\pm 0.03]$ from the slope in fig 4.8. From k_d , the attraction parameter α was calculated to be 5. If the sucrose molecules are assumed to be spherical, the value for D_0 corresponds to monomers coordinated with as many as 24 water molecules, or with dimers coordinated with 12 water molecules, according to the modified Stokes Einstein equation (4.5). At the saturation concentration ($\phi=0.57$) the sucrose cluster size is about 5 molecules (eq. 4.3) which is approximately 1.7 nm.

It is remarkable that the interaction parameter k_d has about the same value for citric acid and sucrose. Although this can be a coincidence, it supports the idea of Brown et al. (1994) that not the attraction between solute molecules, but the hindrance of water molecules or the limited hydration possibilities are the driving force for cluster formation. Hence, with this assumption, not the forces between the solute molecules are responsible for the formation of clusters, but the water molecules

force the solute molecules into clusters, in order to give themselves more 'space' to diffuse freely.

Potassium nitrate

The potassium nitrate measurements revealed that the measured diffusion coefficients at $0.32 [\pm 0.01]$ g/g are the same as can be expected for nitrate ions, hydrated with two or three water molecules, i.e. $1.2 \cdot 10^{-9} \text{ m}^2\text{s}^{-1}$. The same value has been calculated by using the modified Stokes Einstein equation (4.5) and the ion radius of nitrate ($=0.189 \text{ nm}$) found by applying the method of Yatsimirskii (Huheey 1975). Potassium ions are somewhat smaller (0.151 nm) than nitrate ions and therefore they scatter less light. Therefore the total signal obtained will be dominated by the nitrate ions.

Thus, it can be concluded that no cluster formation takes place in potassium nitrate solutions at the concentrations which have been investigated. Two reasons for this are possible. The first one that, contrary to citric acid and sucrose, no hydrogen bonds are formed between the ions. The second is that potassium and nitrate ions may fit in the interstitial holes of the (dynamic) water structure, because they are much smaller than citric acid or sucrose molecules. Therefore, they do not hinder water molecules to seek their preferred structure.

4.4.3 Neutron diffraction of deuterated citric acid solutions

Several samples were prepared in volume fractions ranging from 0.42 to 0.53 and investigated according the procedure outlined in the experimental section. In the appendix it is described how the raw data are corrected for cell scattering, sample attenuation and self shielding. The results are depicted in fig. 4.9. Clearly, peaks appear at $q \approx 5$ and 12 nm^{-1} if the volume fraction increases. The overall intensity increases at higher volume fractions, and the curves do not reach a distinct baseline at high volume fractions in the q range investigated. In literature on interactions in liquids (e.g. Hansen et al. 1991) this is sometimes associated with cluster formation.

For a sample with $\phi=0.49$, which is not shown in the figure because the measuring conditions were slightly different and therefore the absolute intensities, experiments were done at temperatures between 14 and 29°C . Although the estimated supersaturation varied from $S=0.9$ to $S=1.4$, no significant difference in the measured intensities and peak positions was observed. This is consistent with the findings from the PCS experiments that the supersaturation does not influence the cluster size.

With the help of eq. (4.6) the particle diameters which correspond to the peak positions have been calculated. They are summarized in table 4.3.

Table 4.3. Diameters which correspond with peak position for $\phi=0.52$ and 0.53 , assuming hard spheres.

q [nm^{-1}]	d [nm]	type
5	$1.3 [\pm 0.1]$	Cluster
12	$0.5 [\pm 0.1]$	Citric acid
19	$0.3 [\pm 0.1]$	Water

The sizes obtained are consistent with the PCS-experiments, where the cluster size was calculated to be approximately 1.2 nm at $\phi=0.53$. The monomer value of 0.5 nm, however, seems to be somewhat low. But it is very difficult to determine where exactly the peak positions are.

The Fourier inversion was not possible, because the q -range probed was too small to get unambiguous results. Due to the large contribution of incoherent scattering, the complexity of the molecules and their interactions (not only citric acid - citric acid, but also citric acid - water and water - water) no model for the structure in the solution is currently available.

4.5 Conclusions

PCS measurements give information on the motion of citric acid, potassium nitrate and sucrose molecules or aggregates in solutions at high concentration. The collective diffusion coefficient decreases with increasing volume fraction. This gives evidence for attractive forces between the molecules, which results in the formation of small clusters, even if the solutions are not saturated. The clusters are, however, much smaller than the critical cluster size.

An estimation made from the PCS measurements gives for citric acid a cluster size of 3 to 4 molecules (1.1 nm) at the saturation concentration. Calcium ions, which strongly coordinate with citric acid, do not have a pronounced influence on cluster size at the concentration range investigated.

Potassium nitrate does not appear to form clusters. This is concluded from the fact that the diffusion coefficient measured, which is attributed to the nitrate ions, is not altered at relatively high concentration in comparison to the diffusion coefficient expected at infinite dilution.

For sucrose, the PCS measurements indicate that, at infinite dilution, sucrose molecules exist in water as dimers or with 24 hydrating water molecules. It is remarkable that, the coefficient α which describes the attraction behavior of the dissolved molecules or clusters, is the same for citric acid and sucrose. This may indicate that not the forces between the solute molecules are responsible for the formation of clusters, but that the water molecules force the solute molecules into clusters, in order to give themselves more 'space' to diffuse freely. Potassium and nitrate ions may fit in the interstitial holes of the (dynamic) water structure. At the saturation concentration, the sucrose cluster size is around 5 molecules, or 1.7 nm.

Alternatively, it is possible be that the clusters form a different 'phase' compared to crystalline citric acid. Since the average cluster size is much larger than the value expected from the steady state cluster size distribution, the molecules in the clusters experience another supersaturation than crystalline citric acid molecules.

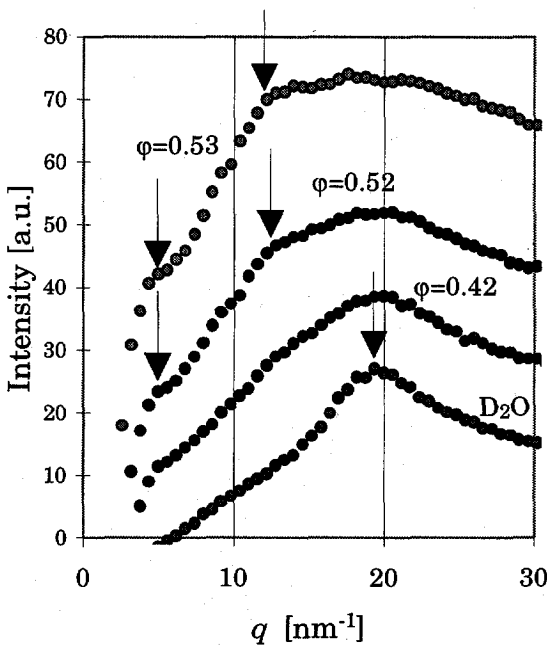
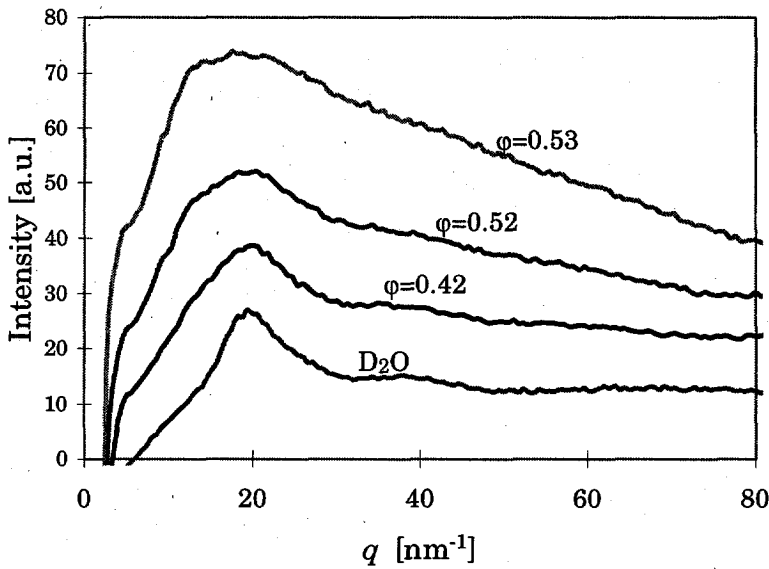


Fig. 4.9. Scattered intensity (not-normalized structure factor $S(q)$) as a function of the normalized scattering vector, of the deuterated citric acid solution in heavy water. Note the stronger overall scattering intensity and the shoulders coming up at $q \approx 5$ and 12 nm^{-1} due to citric acid clusters and monomers, respectively. The profiles did not change if the temperature, and thereby the supersaturation, changed.

In addition, this experienced supersaturation appears not to be temperature dependent, where the supersaturation for crystalline citric acid is strongly temperature dependent. Thus, it can be concluded that these cluster citric acid molecules have different properties compared to crystal citric acid molecules and that the cluster state can therefore be called a distinct phase.

Cluster formation was supported by the neutron diffraction experiments done for citric acid solutions. The scattered intensity was dependent on the volume fraction but was temperature and therefore supersaturation independent. The appearance of a peak in the spectrum at a small q -value indicates formation of clusters at high volume fractions.

Appendix

4.A Correction sample attenuation and self shielding

In order to get a geometry independent measured scattering pattern, which is comparable to $S(q)$, the measured pattern must be corrected for sample attenuation, self shielding and sample cell scattering. This has been worked out in this appendix.

It has been assumed that the sample is infinitely wide, that no multiple scattering occurs and that the incoming beam and the beam reaching the detector are parallel.

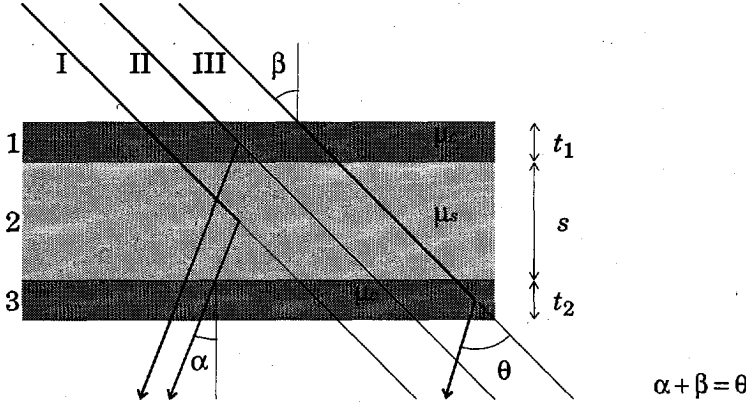


Fig. 4.A.1. Schematic view of the scattering geometry. μ is the linear attenuation [m^{-1}], θ the scattering angle, α the angle between the scattered neutrons and the normal and β the angle between the incoming neutrons and the sample ($=45^\circ$). The quartz sample plate thickness t was 1.0 mm and the sample thickness 2.0 mm.

i. Scattering by sample

The scattered neutron intensity of the sample from dx at x is,

$$dI_s(\theta) = \frac{\Sigma_s(\theta)I(x)}{\cos \beta} dx, \quad (4.11)$$

where $\Sigma_s(\theta)$ is the macroscopic scattering cross section of the sample and I the neutron intensity. Since fig. 4.A.2 shows that $l_1 = x / \cos \beta$ and $l_2 = (s-x) / \cos \alpha$, one obtains for the attenuation before and after scattering, respectively,

$$A_{b,I}(x) = \exp\left(-\frac{\mu_c t}{\cos \beta} - \frac{\mu_s x}{\cos \beta}\right)$$

$$A_{a,I}(x) = \exp\left(-\frac{\mu_s(s-x)}{\cos \alpha} - \frac{\mu_s t}{\cos \alpha}\right). \quad (4.12)$$

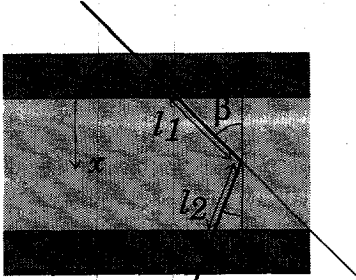


Fig. 4.A.2. Detail of the scattering geometry. l_1 and l_2 are the path lengths of the neutrons before and after the scattering event, respectively.

Hence, the total scattering becomes,

$$I_s(\theta) = I_0 \Sigma_s(\theta) \int_0^s \frac{A_b(x) A_a(x)}{\cos \beta} dx, \tag{4.13}$$

yielding,

$$I_s(\theta) = I_0 \Sigma_s(\theta) T_1(\beta) T_3(\alpha) I_s(\alpha, \beta), \tag{4.14}$$

with,

$$\begin{aligned} T_1(\beta) &= \exp\left(-\frac{\mu_c t_1}{\cos \beta}\right), \\ T_3(\alpha) &= \exp\left(-\frac{\mu_c t_3}{\cos \alpha}\right), \\ I_s(\alpha, \beta) &= \frac{1}{M_s \cos \beta} \exp\left(-\frac{\mu_s s}{\cos \alpha}\right) [\exp(M_s s) - 1], \\ \text{and } M_s(\alpha, \beta) &= \mu_s \left(\frac{\cos \beta - \cos \alpha}{\cos \alpha \cos \beta}\right). \end{aligned} \tag{4.15}$$

ii. Scattering by container

The scattered neutron intensity of the container cell from dx at x is,

$$dI_c(\theta) = \frac{\Sigma_c(\theta) I(x)}{\cos \beta} dx. \tag{4.16}$$

Thus for situation II, scattering in plate 1 (fig. 4.A.1) two cases can be distinguished, attenuation before and after scattering,

$$\begin{aligned} A_{b,1} &= \exp(-\mu_c l_1) = \exp\left(-\frac{\mu_c x}{\cos \beta}\right), \\ A_{a,1} &= \exp\left(-\mu_c l_2 - \frac{\mu_s s}{\cos \alpha} - \frac{\mu_c t_3}{\cos \alpha}\right), \\ \text{with } l_2 &= \frac{t_1 - x}{\cos \alpha}. \end{aligned} \tag{4.17}$$

For situation III (fig 4.A.1), which shows the scattering plate 3,

$$A_{b,3} = \exp\left(-\frac{\mu_c t_1}{\cos \beta} - \frac{\mu_s s}{\cos \beta} - \frac{\mu_c x}{\cos \beta}\right)$$

and $A_{a,3} = \exp\left(-\frac{\mu_c(t_3 - x)}{\cos \alpha}\right).$ (4.18)

Thus the total scattering equals,

$$I_{c,1}(\theta) = I_0 \Sigma_c(\theta) \int_0^{t_1} \frac{A_{b,1}(x) A_{a,1}(x)}{\cos \beta} dx, \quad (4.19)$$

from plate 1, and

$$I_{c,3}(\theta) = I_0 \Sigma_c(\theta) \int_0^{t_3} \frac{A_{b,3}(x) A_{a,3}(x)}{\cos \beta} dx, \quad (4.20)$$

for plate 3, which results in,

$$I_c(\theta) = I_{c,1}(\theta) + I_{c,3}(\theta) = I_0 \Sigma_c(\theta) (T_1(\beta) T_2(\beta) \mathcal{V}_{c,1}(\alpha, \beta) + T_2(\alpha) T_3(\beta) \mathcal{V}_{c,3}(\alpha, \beta)), \quad (4.21)$$

with,

$$T_2(\beta) = \exp\left(-\frac{\mu_s s}{\cos \beta}\right),$$

$$T_2(\alpha) = \exp\left(-\frac{\mu_s s}{\cos \alpha}\right),$$

$$l_{c,i}(\alpha, \beta) = \frac{1}{M_c \cos \beta} \exp\left(-\frac{\mu_c t_i}{\cos \alpha}\right) [\exp(M_c t_i) - 1], \quad i = 1, 2,$$

and $M_c(\alpha, \beta) = \mu_c \left(\frac{\cos \beta - \cos \alpha}{\cos \beta \cos \alpha} \right).$ (4.22)

iii. Correction for container scattering

In a sample measurement, the sum of the scattering by the sample and the scattering by the container is measured,

$$I_1(\theta) = I_s(\theta) + I_c^s(\theta), \quad (4.23)$$

where $I_s(\theta)$ and $I_c^s(\theta)$ are defined by eq. (4.14) and eq. (4.21), respectively. A measurement of an empty container gives,

$$I_2(\theta) = I_c^0(\theta),$$

with $I_c^0(\theta)$ according to eq. (4.21) with $\mu_s = 0$. Subtraction of the container scattering gives,

$$I_{s,corr-cs}(\theta) = I_1(\theta) - f_{saf}(\alpha, \beta) I_2(\theta), \quad (4.24)$$

with sample attenuation factors (for $t_1 = t_3$),

$$f_{saf}(\alpha, \beta) = \frac{I_2(\theta)}{I_c^0(\theta)} = \frac{T_1(\beta) T_2(\beta) + T_2(\alpha) T_3(\alpha)}{T_1(\beta) + T_3(\alpha)} \quad (4.25)$$

iv. Correction for angle dependence of self shielding

Finally, a correction needs to be made for absorption of scattered neutrons by the sample itself. If the measured intensity after correction for container scattering is $I_{s,corr-cs}$, the correction for angle dependence of self shielding is (eq. 4.14),

$$I_{s,corr-ssh}(\theta) = f_{ssh}(\alpha, \beta) I_{s,corr-cs}(\theta), \quad (4.26)$$

with self shielding factor,

$$f_{ssh}(\alpha, \beta) = \frac{1}{T_1(\beta) T_3(\alpha) \nu_s(\alpha, \beta)}. \quad (4.27)$$

Thus, the sample scattering can be calculated from the total scattering using eq. (4.26) if the scattering profile of an empty container is known and if the attenuation factors are known. These factors can be obtained from literature or by performing an absorption experiment in a container with a known thickness.

References

- M.K. Cerreta and K.A. Berglund (1987) *J. Crystal Growth* **84**, 577.
- D.J. Brown, I.M. Grimsey and T.H. Lilly (1994) The Dynamics and Thermodynamics of supersaturated Sucrose Solutions, *First International Particle Forum*, Denver, AIChE, Part I, Crystallization and Precipitation, 311.
- I.M. De Schepper (1994) Statica en Dynamica van Verdichte Gassen en Vloeistoffen, in *IRI Cursus Neutronenverstrooiing* (in Dutch), Chapter 4.
- R. Finsy, A. Devriese H. and Lekkerkerker (1980) *J. Chem. Soc. Faraday Trans. II* **76**, 767.
- R. Finsy (1990) *Part. Part. Syst. Charact.* **7**, 74.
- N.C. Ford (1983) Theory and Practice of Correlation Spectroscopy, in: *Measurement of Small Particles by Quasi Elastic Light Scattering*, Ed. B. Dahneke, Wiley, New York, 31.
- R.K. Freier (1987) *Aqueous solutions*, W. de Gruyter, New York, 443-445
- G.M. Galis and A.S. Myerson (1992) *J. Crystal Growth* **116**, 41.
- Y. Georgalis, A. Zouni, W. Eberstein and W. Saenger (1993) *J. Crystal Growth* **126**, 245.
- J.P. Hansen, D. Levesque and J. Zim-Justen (1991) *Les Houches, Session LI*, Elsevier, Amsterdam.
- J.P. Hansen, I.R. McDonald (1976) *Theory of simple liquids*, Academic Press, London.
- G.A. Hussmann, M.A. Larson and K.A. Berglund (1984) in: *Industrial Crystallization 1984*, Eds. S.J. Jancic and E.J. de Jong, Elsevier, Amsterdam, 21.
- J.E. Huheey (1975) *Inorganic Chemistry (SI units edition)*, Harper and Row, New York, 77.
- C.A. Knight (1979) *Adv. Colloid Interface Sci.* **10**, 369.
- Landolt-Bornstein (1991) *Numerical Data and Functional Relationships in Science and Technology: Volume 5: Structure Data of Organic Crystals A*, Springer-Verlag, New York, 299.
- M.A. Larson and J. Garside (1986) *Chem. Eng. Sci.* **41**, 1285.
- J.W. Mullin and C.L. Leci (1969) *Philos. Mag.* **19**, 1075.
- H. Narayanan and G.R. Youngquist (1987) Some Properties of Supersaturated Solutions, in D.M. Briedis and K.A. Ramnarayanan (eds) *Fundamental Aspects of Crystallization and Precipitation Processes*, 1.
- K. Ohgaki, N. Hirokawa and M. Ueda (1992) *Chem. Eng. Sci.* **47**, 1819.
- P.N. Pusey (1991) *Colloidal Suspensions*, in: *Les Houches, Session LI*, Eds. J.P. Hansen, D. Levesque and J. Zim-Justen Elsevier, Amsterdam, 765.
- P.W.M. Rutten (1992) *Diffusion in Liquids*, Ph.D. thesis Delft University of Technology, Delft, Chapter 5.
- L.S. Sorrell and A.S. Myerson (1982) *AIChE Journal* **28**, 772.
- R. Steiniger and J.H. Bilgram (1991) *J. Crystal Growth* **112**, 203.
- C.A.M. Vijverberg, J.A. Peters, A.P.G. Kieboom and H. van Bekkum (1980) *Recl. Trav. Chim. Pays-Bas* **99**, 403.
- H. Wiese and D. Horn (1991) Single-mode fibers in fiber-optic quasielastic light scattering: A study of the dynamics of concentrated latex dispersions, *J. Chem. Phys.* **94**, 6429.

Gas to particle conversion. Homogeneous nucleation and coagulation¹⁾

5

Abstract

This chapter discusses nucleation from the gas phase. The supersaturation is very high, while the concentration of reactants is relatively low. The critical nucleus size is one molecule and, therefore, every molecule is a critical nucleus. Thus, the nucleation takes place 'homogeneously'. The particles grow mainly by coagulation. Aerosols with a sufficiently high concentration can be monitored by photon correlation spectroscopy (PCS). A single mode optical fiber in combination with a polarization filter and an interference filter significantly reduced the strong background flame light. Hence, a good signal to noise ratio was obtained and optical alignment has become easy by using the fiber.

Standard PCS software has been used to obtain diffusion coefficients and velocities of the particles from the light scattering data. Using this, the particle size has been calculated.

In this study the growth of silicon nitride particles in an aerosol reactor is monitored using this method. The particles are formed by heating silane and ammonia in a strong infrared laser beam. The reaction causes a bright flame. Kruis et al. (1993a) developed a coagulation model, which is used to predict the development of the particle size in the flame.

The silicon nitride particles grow in less than 1 ms from 30 to 240 nm. The characteristic sintering time which has been found from matching the coagulation model from Kruis et al. (1993a) to the experimental results is $3 \cdot 10^{-12} T d_p^3 \exp(53.65/T) \{\pm 20\%$ [s], where T is the temperature [K] and d_p the primary particle diameter [nm]. The high value of the pre-exponential factor compared to boron carbide which also sinters by lattice diffusion (Greskovich and Rosolowski 1976), is attributed to the different molecular properties of silicon nitride.

5.1 Introduction

Ceramics

Ceramic materials are used more and more in technical applications, since they are generally extremely hard and resistant to wear and tear. Therefore ceramic materials are well suited for e.g. motor parts. Ceramics are inorganic materials, often oxides, but also nitrides or borides, which are synthesized by sintering their precursors at high temperatures. The composition and the particle size distribution of these precursors largely determine the product quality.

In this study, the formation of silicon nitride is studied. This material can be synthesized directly out of the gas phase, because at atmospheric pressure it has no

¹⁾ Most of this chapter has been published in *Journal of Aerosol Science*. The full reference is: M.A. van Drunen, I.L. Tuinman, J.C.M. Marijnissen, H.G. Merkus and B. Scarlett (1994) Measurement of Aerosols in a Silicon Nitride Flame by Optical Fiber Photon Correlation Spectroscopy, *J. Aerosol Sci.*, 25, 895-908.

liquid phase. The main advantage of this route is that the product can be made extremely pure, primarily because no reactor walls are involved. For the same reason, optical fibers used for telecommunications, are made via an aerosol route. Another advantage is that the resulting particles are usually several hundreds of nanometers, which are well-suited for sintering.

Growth by coagulation

The system investigated here is an aerosol reactor in which a flame develops, because a mixture of silane and ammonia is ignited by a high power infrared laser beam. Because of the high laser intensity, silane and ammonia disintegrate and, therefore, a very high supersaturation for silicon nitride formation results. A bright white flame results in which silicon nitride particles are formed. In this system the critical cluster size is approximately one 'molecule', and the nucleation rate is extremely fast. In a fraction of a millisecond, all silane and ammonia react into very small silicon nitride particles. This system is one of the relatively rare systems in which homogeneous nucleation occurs, but as a result, not nucleation, but the coagulation rate determines the overall reaction rate. From a kinetic point of view, nucleation is not important anymore, and it does not even appear in the equations anymore. Coagulation is collision of particles, followed by chemical bond formation, e.g. as with silicon nitride by sintering. Growth of the particles by addition of single molecules only takes place in the very beginning of the process, because their concentration reaches extremely fast the saturation concentration (≈ 0).

Consequently, in the system investigated here, the final particle size distribution is determined by coagulation. Generally, coagulation results in particles with very open structures, with large surface volume ratios. The 'fluffiness' of the particles is often quantified by the fractal dimension. In three dimensions, solid spheres or cubes have the highest fractal dimension possible, namely 3.

Greskovich and Rosolowski (1976) showed that silicon nitride, which has no liquid phase at normal pressure, sinters according to the relatively rare *lattice diffusion* mechanism. In our system, the very small particles which form low in the flame are amorphous, which was shown by electron diffraction (Tuinman et al. 1996). Higher in the flame the particles recrystallize into a crystalline phase. Sintering also takes place during this process, but this can hardly be observed.

Kruis et al. (1993b) extensively investigated the aerosol reactor used here, and developed several kinetic models. In addition, they took samples from the flame and investigated them off-line using transmission electron microscopy. However, since the sampling disrupts the system, there is no guarantee that the samples are representative for the particles in the flame. The objectives of the experiments described in this paper were to monitor the Si_3N_4 particles in the flame in situ, and to test the coagulation model of Kruis et al. (1993a). They tested this model for *silicon* particles in the same reactor of the present study. The model describes 'the evolution of aggregate volume and surface area by simultaneous coagulation and sintering at non-isothermal conditions, assuming a monodisperse aggregate and primary particle size distribution and accounting for the aggregate structure by a mass fractal dimension of the aggregates' (Kruis et al. 1993a).

PCS and aerosols

Although photon correlation spectroscopy (PCS) is one of the few techniques which are able to measure submicrometer particles on-line and in situ, it is rarely used in

aerosol characterization. The main limitation is that often the particle concentration is too low. Consequently, the fluctuations do not only arise from the Brownian motion, but also from the changing number of particles in the measuring volume (Weber et al. 1993). These number fluctuations occur when the number of particles in the measuring volume is less than about hundred. The measuring volume in PCS is typically 10^{-6} cm^3 , so the minimum particle concentration is about 10^8 cm^{-3} . In flames, like the ones in this system, the particle concentration usually exceeds this concentration, hence PCS can be used to monitor particle growth. Soot particles forming at high concentration in burners have been studied by Lhuissier et al. (1989) using this technique. Flower (1983) and Penner and Chang (1981) measured diffusion coefficients of soot particles in flames by probing the power spectra which are the Fourier transforms of the autocorrelation functions (chapter 3).

Unfortunately, the flame itself emits a considerable amount of constant background light, and hence not only the scattered light enters the detector, but also the light emitted by the flame, causing a very unfavorable signal to noise ratio. In our experiments the noise level has been decreased by filtering the light from the flame in three stages. The most important filter is the single mode optical fiber which replaces the pinhole lens system in classical PCS. It acts as a spatial filter, as outlined by Ricka (1993): 'Boundary conditions imposed on the electromagnetic field in a single mode wave guide are such that only one transverse structure, only one mode of the field is propagated.' See section 3.B for more detailed information. The other main advantage of this receiver is the easy alignment of the setup.

This measuring system has been applied to a silicon nitride aerosol reactor in order to monitor the evolution of the particle size in the flame. The flame is laminar and because the reactor walls do not participate, turbulence, which would disturb the measurements significantly, does not occur.

This chapter starts with a short outline of the theory of the relationship between the diffusion coefficient and the particle diameter in gases and the coagulation model used by Kruijs et al. (1993a) (section 5.2). In section 5.3 the experimental procedures are explained and this is followed by the results and discussion section 5.4. The chapter ends with the conclusions (5.5).

5.2 Theory

The theory of photon correlation spectroscopy has been outlined in chapter 3. The reader is specially referred to section 3.5, in which the effect of a laminar flow on PCS measurements has been outlined.

The diffusion coefficient obtained with this technique is evaluated somewhat differently in gases compared to liquids. This is discussed in section 5.2.1. Section 5.2.2 shows the characteristics of the model by Kruijs et al. (1993a).

5.2.1 Particle diffusion in gases

In gases, the relationship between the diameter d and the diffusion coefficient D is dependent on the ratio of the mean free path ζ of the gas molecules (Friedlander 1976),

$$\zeta = \frac{\eta}{\rho} \sqrt{\frac{\pi M}{2RT}}, \quad (5.1)$$

and the particle size. Here, η is the gas viscosity, ρ its density, M its molar weight, R the gas constant and T the temperature. In the free molecular regime, where the particle size is much smaller than the gas mean free path, the relation between the diffusion coefficient and the particle diameter is given by Fuchs (1964) as,

$$d = 2\sqrt{\frac{1154 kT\zeta}{6\pi\eta D}}, \quad (5.2)$$

where k is Boltzmann's constant.

In the continuous regime ($d \gg \zeta$), the Stokes-Einstein equation (section 3.2) is commonly used, and if $d \approx \zeta$ Cunningham's slip correction factor is used in combination with this equation (Fuchs 1964).

Many variables in the equations mentioned above, e.g. η and ζ depend on the temperature. Thus, the temperature must be measured accurately. The temperature in flames can be measured by two-color pyrometry which is based on black body radiation. This technique accounts for absorption of the flame light by the particles as outlined by Bauer et al. (1991).

The viscosity of mixtures of gases is a complex function of their volume fraction. For mixtures of the non-polar diatomic molecules hydrogen and nitrogen, used here, the method of Lucas (Reid et al. 1987) can be used to calculate the viscosity. It is calculated from a set of reduced variables and the volume fraction of the gases.

Although the silicon nitride particles investigated are not spherical, eq. (5.2) probably gives a good estimate of the equivalent spherical particle diameter, because the particles are not elongated or flat (Kruis 1993).

5.2.2 Coagulation of silicon nitride particles

In the silicon nitride system investigated here, the primary particles are formed by chemical reaction. The temperature rise is extremely fast due to the heating by the laser. Silane and ammonia decompose almost immediately, creating an enormous supersaturation. This results in an extremely high monomer production rate (Kruis 1993). Hence, the nucleation step is not very important for particle coagulation kinetics.

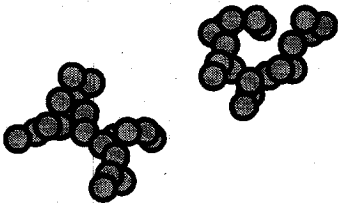


Fig. 5.1. In the model, aggregates are formed by collisions of spherical primary particles. All of them are assumed to contain the same number of these primary particles, which are 'glued' together by sintering. In the aggregation stage, no monomers are assumed to exist.

The primary particles 'grow' by successive collisions. As the particle size increases, aggregates of primary particles are formed (fig. 5.1). Postulating that all aggregates contain the same number of equally sized primary particles Kruis et al. (1993a) used the following set of equations. Fig. 5.2 shows that this postulation is a rather

crude approximation, but the resulting differential equations are already very difficult to be solved numerically in this simplified case. Nevertheless, it will be shown that the calculations are useful to characterize the process. Kruis et al. (1993a) started with the evolution of the number of aggregates,

$$\frac{dN'}{dt} = -\frac{1}{2}\beta\rho N'^2, \quad (5.3)$$

Here, N' is the number concentration of the aggregates divided by the gas density, ρ , and β is the frequency function of collisions between the aggregates. Effects of turbulence have been neglected, since the flame is laminar.

For irregularly shaped particles, the particle radius, r_p , is replaced by a collision radius, r_c , which is defined as,

$$r_c = r_p (n_p)^{\frac{1}{D_f}}, \quad (5.4)$$

where n_p is the number of primary particles in one aggregate and D_f is its mass fractal dimension. Then,

$$\beta = 8\pi D r_c \left(\frac{r_c}{2r_c + \sqrt{2}\kappa} + \frac{\sqrt{2}D}{c r_c} \right)^{-1}, \quad (5.5)$$

where D can be calculated using eq. (5.2), $d \approx 2r_c$, c is the particle mean thermal speed and κ is the transition parameter given by,

$$\kappa = \left(\frac{1}{6r_c l} \right) \cdot \left\{ (2r_c + l)^3 - (4r_c^2 + l^2)^{\frac{3}{2}} \right\} - 2r_c, \quad (5.6)$$

with the particle mean free path $l = \frac{8D}{\pi c}$.

The concentration of free molecules was assumed to be zero. The surface area of an aggregate, A , increases by coagulation and decreases by sintering,

$$\frac{dA}{dt} = -\frac{1}{N'} \frac{dN'}{dt} A - \frac{1}{\tau_s} (A - A_s), \quad (5.7)$$

with τ_s the characteristic sintering time, defined as the time needed to reduce the excess surface area of the aggregate as compared to an equivalent volume sphere by 63%. A_s is the surface area of the completely fused and thus spherical aggregate,

$$A_s = \left(\frac{V}{V_0} \right)^{\frac{2}{3}} A_0, \quad (5.8)$$

where A_0 and V_0 denote the surface area and volume of the monomer, respectively. In this work, the monomer is assumed to be the unit cell, i.e. two Si_3N_4 molecules. The aggregate volume V is only affected by coagulation,

$$\frac{dV}{dt} = -\frac{1}{N} \frac{dN'}{dt} V, \quad (5.9)$$

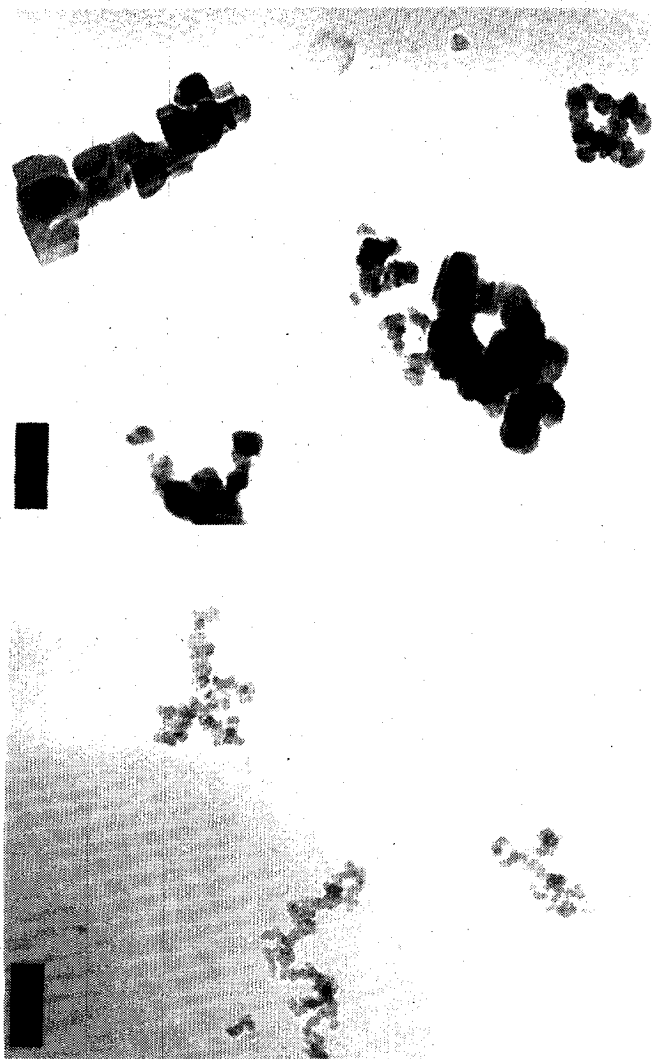


Fig. 5.2. TEM photographs of silicon nitride particles taken in an experiment where the distance between the CO₂ laser and the nozzle was 4.5 mm. The upper sample is obtained high in the flame ($h=0.6$ mm) and lower one low in the flame ($h=1.4$ mm). Note that the scale is the same and that primary particle size increases dramatically. Both sintering and recrystallization take place. The mark represents 250 nm.

The primary particle size and the number of primary particles in an aggregate are,

$$d_p = \frac{6V}{A} \text{ and} \tag{5.10}$$

$$n_p = \frac{V}{V_p}, \text{ respectively.} \tag{5.11}$$

V_p is the primary particle volume ($\pi d_p^3/6$), which is assumed to be spherical. The aggregate collision radius can be calculated using,

$$r_c = \frac{3V}{A} \left(\frac{A^3}{36\pi V^2} \right)^{\frac{1}{D_f}} \quad (5.12)$$

No literature data for the sintering time of silicon nitride have been found. Greskovich and Rosolowski (1976) qualitatively showed that sintering occurs in silicon nitride. For other covalently bonded solids which sinter by lattice diffusional processes, e.g. boron carbide and silicon carbide (Kingery et al. 1976), an empirical relationship for τ_S is given by Xiong et al. (1992),

$$\tau_S \propto \frac{kT}{D^* \Omega \gamma} d_p^3, \quad (5.13)$$

where Ω is the volume of the diffusing units, γ the surface energy and D^* the diffusion coefficient of the diffusing molecules. For boron carbide,

$$D^* = 3 \cdot 10^{-5} \exp\left(-\frac{53.65}{T}\right). \quad (5.14)$$

Combining equations (5.13) and (5.14), Xiong et al. (1992) found for boron carbide,

$$\tau_S = 3.9 \cdot 10^{-20} T d_p^3 \exp\left(-\frac{53.65}{T}\right), \quad (5.15)$$

with d_p in nm and T in K. At 3000 K and for $d_p = 10$ nm τ_S has an order of magnitude of 10^{-12} s. Since the residence time in the flame is in the order of milliseconds, sintering is a plausible mechanism. Combining the equations (5.13) and (5.14) the following expression for silicon nitride is expected,

$$\tau_S = k T d_p^3 \exp\left(-\frac{53.65}{T}\right), \quad (5.16)$$

where k is an unknown factor.

5.3 Experimental

5.3.1 The setup

The experimental set up is shown in fig. 5.3. Details of the aerosol reactor can be found in Kruis (1993). Silane (SiH_4) and ammonia are used as precursors for the synthesis of Si_3N_4 . The gases are introduced through four concentric nozzles below the laser beam. The gases from the middle and third nozzle mix by diffusion through the sheath gas coming from the second nozzle. The sheath gas separates the reactant gases as they leave the nozzle. They can react if they diffuse through the sheath of inert gas. The gas from the fourth (outer) nozzle acts as a carrier gas.

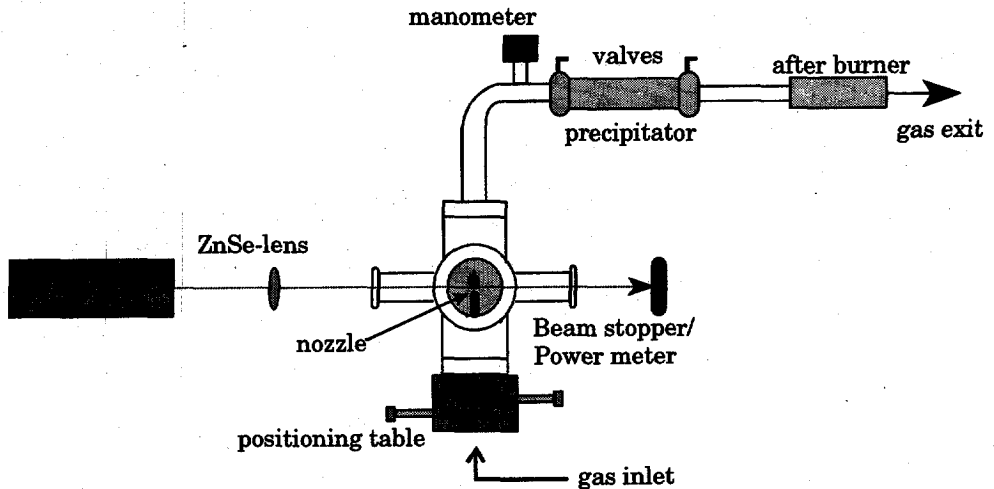


Fig. 5.3. Schematic side view of the experimental setup. The gases are fed in at the bottom of the reactor. As they reach the CO₂ laser beam an aerosol flame develops. The particles formed are separated by an electrostatic precipitator.

This laminar gas flow is heated extremely fast by the 160 W infrared (IR) carbon dioxide laser beam (Edinburgh Instruments PL6, Edinburgh, UK). The laser was operated at a wavelength of 10.6 μm (10P20 line) and its beam was focused to a diameter of about 3.5 mm. The height between the nozzles and the CO₂ laser can be varied by moving the reactor up and down. The distance between the nozzle and the center of the CO₂ laser beam, H , was varied between 2.5 and 11.5 mm. The gas flows used were: middle nozzle, silane 80 cm³/min ($P=P_0$, $T=T_0$), second nozzle, nitrogen 50 cm³/min, third nozzle, ammonia 320 cm³/min, fourth nozzle nitrogen carrier gas, 1,000 cm³/min. These flows were chosen to obtain a laminar gas flow with a flat overall profile.

In order to calculate the particle size from the diffusion coefficient using the Stokes-Einstein equation with Cunningham's slip correction factor, the gas viscosity had to be estimated. This was done to check the validity of the free molecular regime equation (5.2). It was assumed that ammonia and silane dissociated immediately when they reached the laser beam and that the conversion into silicon nitride was 100 percent. On these assumptions, the ratio nitrogen to hydrogen was 85 to 15. The influence of silicon compounds on the viscosity has been neglected.

5.3.2 The measuring system

A helium neon (HeNe) laser (Melles Griot 05-LHP-151, 5 mW, vertically polarized, $w_0=1.2$ mm, $\phi=0.1$ mrad) was mounted perpendicular to both the gas flow and to the CO₂ laser beam in a laser holder which enabled it to move both horizontally and vertically (fig. 6.4). The height of this laser was varied relative to the CO₂ laser between 1.3 mm below the focus heart and 2.0 mm above the focus heart. A lens with a focal length of 100 mm was mounted on the HeNe laser. Using eq. (3.22) one

obtains for the beam waist diameter $100 \mu\text{m}^2$). The HeNe laser probed the center of the flame, above the center nozzle (fig. 6.5).

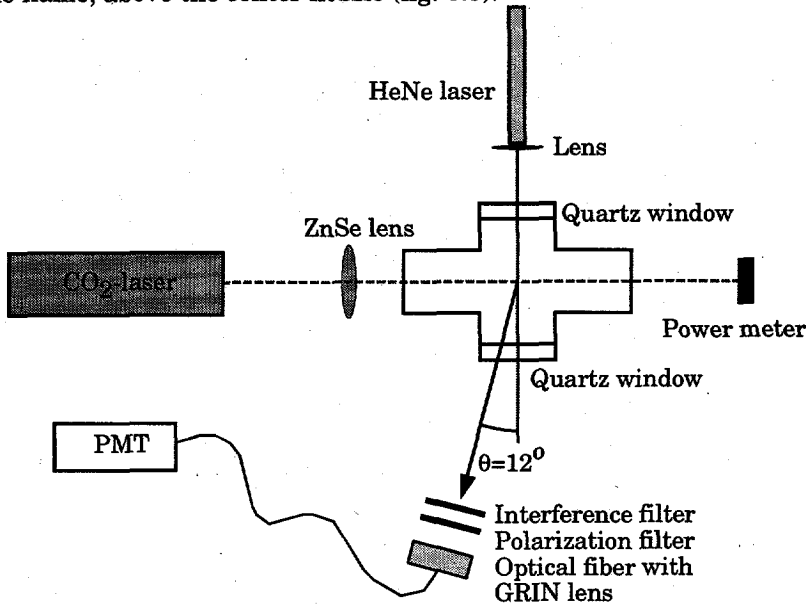


Fig. 5.4. Top view scheme of the measuring set up. PMT is the photomultiplier tube. The scattering light from the helium neon laser beam is caught by the fiber at an angle of 12° .

The detector was mounted at an angle of 12° relative to the HeNe laser beam. This small angle was chosen in order to obtain a high count rate and in order to minimize refraction by the quartz window. The detector was a single mode fiber for 488 nm with a gradient index lens mounted at its end (OZ-optics LPC-03-488-3.5/125-1.4-6.6-3-3.0-4). Of course, a single mode fiber for $\lambda_0 = 488 \text{ nm}$ is also single mode for 633 nm (HeNe). In front of the detector an interference filter (633 nm) and a polarizing filter passing only vertically polarized light were placed to prevent most of the light of the flame from entering the detector. The fiber led to a Hamamatsu R649 photo multiplier tube, which detected the scattered light signal. This signal was amplified, discriminated and finally correlated by a Brookhaven Instruments BI 8000 correlator. The delay time was $0.5 \mu\text{s}$, linearly spaced, and the number of channels used was typically 30. The count rate varied from 100,000 to 900,000 counts per second. Sometimes higher count rates occurred, mainly due to the high flame light intensity. Multiple scattering probably did not occur as could be seen from the relatively low scattering count rate. If high count rates occurred a gray filter was placed in front of the optical fiber in order to prevent saturation of the photomultiplier tube. The first data channel was omitted in the calculations because it can suffer from dead time and afterpulsing effects from the photo multiplier. The autocorrelation functions were analyzed by the Brookhaven programmed method of cumulants as given by eq. (3.16) and using eq. (3.21). The signal to noise

²⁾ Due to a wrong equation in our paper (Van Drunen et al. 1994) the beam waist diameter was estimated too small, and therefore, so were the calculated velocities.

ratio, indicated by the intercept A in eq. (3.13) is usually between 0.9 and 1.0 for a single mode fiber detector. In our experiments this value decreased due to the flame light, especially low in the flame, where the particles are very small and so is their light scattering power. The value of A varied from 0.25 low in the flame to 0.65 higher in the flame. In order to obtain sufficient accuracy, usually three or four autocorrelation functions of five minutes duration were added.

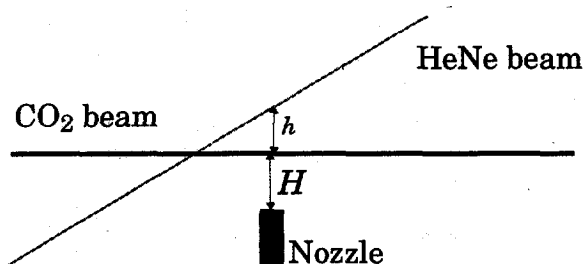


Fig. 5.5. Side view of laser beams. H is the distance between the nozzle and the heart of the infrared CO₂ laser beam ($\lambda_0=10.6 \mu\text{m}$) and h is the distance between the heart of the CO₂ laser beam and the heart of the helium neon laser beam ($\lambda_0=633 \text{ nm}$).

The temperatures were measured afterwards with two-color pyrometry, at the same conditions as the photon correlation experiments. The setup used was similar to the one Bauer et al. (1991) used. The temperature measurements are well reproducible but seem to be somewhat high for this type of flame. It may be that some systematic error occurs due to unknown origins. This error is estimated to be about 10 percent and will influence the particle sizes calculated from the measured diffusion coefficients, because this depends on the temperature through the mean free path.

5.3.3 Modeling

The computer program *RRStiff* obtained from the Delft Reactor Research Foundation has been used to calculate the collision radius r_c as a function of time, from the set of differential equations describing the coagulation. This program uses a Runge Kutta iteration to solve sets of stiff or non-stiff differential equations.

The constants A_0 and V_0 were obtained from the silicon nitride unit cell (two Si_3N_4 molecules) and N'_0 from the initial silane concentration. Hence, $V_0=0.132 \text{ nm}^3$, $A_0=1.25 \text{ nm}^2$ and $N'_0=9.41 \cdot 10^{24} \text{ kg}^{-1}$. The model is reasonably insensitive to the values for V_0 and A_0 , except in the case of extremely short times.

A parabolic function along the vertical flame axis was chosen for the temperature, which closely matched the measured values in the temperature range investigated. The viscosity and the mean free path are quite complex functions of temperature. However, it appeared that linear fitted values closely matched the exact model values in the temperature range investigated. These fitted values were then used in the model instead of the exact values. The gas density was calculated from the ideal gas law, based on the fact that all experiments were performed at atmospheric pressure. D_f was taken to be 1.8, a value often found for these agglomerated particles (Kruis 1993). k in eq. (5.16) was varied to match the experimental results. To convert the time scale to a length scale the particle velocity was needed. From the experimental data the particle velocity was taken to be 5 m/s.

5.4 Results and discussion

The results are summarized in table 5.1. On the average, the silicon nitride particles grow in less than 2 ms from 30 to 240 nm. Aggregates with a PCS diameter of 34 nm have been detected with a simple 5 mW helium neon laser, which was possible because their concentration was high enough. Probably, even smaller particles can be measured if a laser of higher power and shorter wavelength is used, since the light intensity scattered by a particle increases with the laser light wavelength to the power minus four. If a faster correlator is used, the resolution at short delay times will increase and thereby the accuracy of the derived particle sizes and velocities.

In fig. 5.6 the Y-functions, the raw data in a convenient form for one nozzle height, are shown as an example.

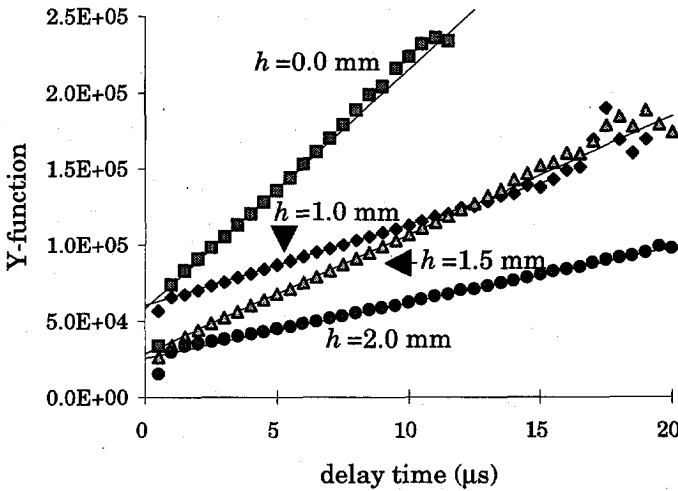


Fig. 5.6. Y-functions of some auto correlation functions obtained with the CO_2 laser beam 6.5 mm above the nozzle end. The intercept equals Dq^2 and the slope is $v^2/2w^2$. Note the afterpulsing and response time effects in the first channel ($\tau = 0.5 \mu\text{s}$).

The PCS-average particle size is drawn as a function of the height in the flame h in fig. 5.7. The experimental error in the diffusion coefficient was 5 to 15 percent, except for the experiments at $H=11.5$, where it was sometimes 25 percent. Here, the temperatures were higher because the gases were premixed and the reaction is exothermic. Probably a systematic error in the autocorrelation function analysis occurred due to rapid expansion of the gas causing the particles to move in directions other than perpendicular to the scattering plane or due to turbulence.

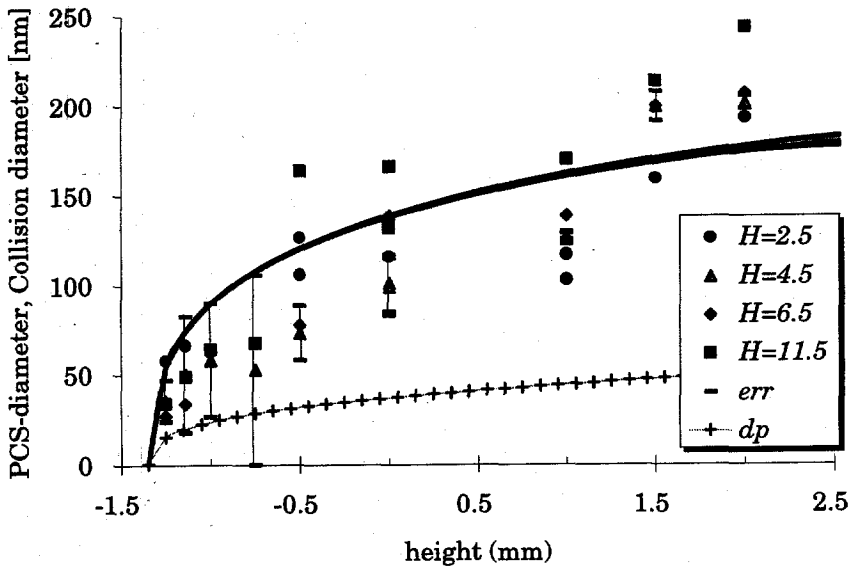


Fig. 5.7. PCS-average diameter (points) and simulated collision diameters (almost coinciding lines) using the model by Kruis et al. (1993a) as a function of the position relative to the heart of the CO_2 laser beam. H is the distance between the nozzle and the heart of the CO_2 laser beam in mm. Error bars for the $H=4.5$ points are given as an example. They are based on the correlation coefficient for the curve fit to the measured autocorrelation functions. Hence, they do not include systematic errors. In addition, the model primary particle size (line marked with +) is shown.

The particle sizes calculated are always at least seven times smaller than the mean free path of the gas molecules. In addition to the free molecular regime equation (eq. 5.2), the Stokes-Einstein equation together with Cunningham's slip correction factor was applied to calculate the particle size from the diffusion coefficient (Fuchs 1964). Both equations gave the same diameters except for the largest particles, where the differences were smaller than two percent.

The error in the measured velocities is often much higher. Low in the flame, where the particles hardly scatter any light, because they are very small, the second cumulant could often not be obtained accurately. Hence, the velocity which is derived from this cumulant could not be determined. As has been outlined before, the accuracy of the second and higher order cumulant suffers from noise influences. High in the flame, where the signals to noise ratios are higher the second cumulant error is much smaller but still of the order of 20 to 40 percent. The second cumulant values found from the experiments are much higher than can be expected from the polydispersity ($|P.I.| \gg 10$) of the aggregate size distribution. Hence, the influence of polydispersity has been neglected.

Although the particle size does not change significantly as a function of height H above the nozzle the composition of the particles changes dramatically, as could be seen from X-ray diffraction results and nitrogen amount of the particles formed. The main reason for this is the different time the gases have to mix before they

reach the CO₂ laser beam. This will be further discussed in a subsequent paper (Tuinman et al. 1996).

Comparison with the TEM photographs which Tuinman et al. (1996) obtained by sampling the silicon nitride flame in the same reactor, shows that the sizes found by PCS qualitatively match his results, as can be seen from fig. 5.2.

Until $h=2.5$ mm the particles grow rapidly by collisions as can be seen from the experiments. The model predicts that high in the flame ($h=5$ mm, not shown in the figure) the agglomerate size tends to decrease, due to sintering of the primary particles causing the agglomerates to form a denser structure. Thus, D_f increases slightly.

The agglomeration model predicted the particle 'growth' well. However, in order to match these experimental results, we had to adapt the pre-exponential factor k in the equation for the characteristic sintering time. It appears to be $3 \cdot 10^{-12} \text{ nm}^{-3} \text{ sK}^{-1}$ ($\pm 20\%$), quite different from the value for boron carbide ($3.9 \cdot 10^{-20} \text{ nm}^{-3} \text{ sK}^{-1}$). This could be due to the smaller diffusion coefficient and a larger characteristic size. In addition, boron carbide is a semi-conductor, which may lead to quite different transport mechanisms. For silicon nitride, the characteristic sintering time is of the same order of magnitude as the residence time in the flame.

The results of the simulation are shown in fig. 5.7. It has been assumed that $d_{PCS} \approx d_c$. It appears that the predicted results are almost identical. Sintering causes the agglomerates to become denser and thus smaller. The difference between the measured and calculated diameters at $H=11.5$ mm is attributed to the systematic error that occurred in the evaluation of the auto correlation function due to the gas expansion. The autocorrelation function showed a non-exponential decay component which we have seen more often as turbulence occurs.

5.5 Conclusions

Using an optical fiber detector, together with a polarizing filter and an interference filter, PCS has been applied successfully to monitor the average particle size and its increase with height in an aerosol flame. Alignment of the set up is easy and standard software can be used to analyze the autocorrelation functions to obtain the diffusion coefficient and the particle velocity. To calculate the PCS diameter from the diffusion coefficient accurately, the system must be well characterized. Particularly, the temperature is an important parameter. Particles as small as 34 nm have been detected with a simple 5 mW helium neon laser. Probably, even smaller particles can be measured if a laser of higher power and shorter wavelength is used in combination with a faster correlator. The particles were monitored until they reached the size of approximately 200 nm.

The particle sizes can be predicted by the agglomeration model derived by Kruis et al. (1993a). The characteristic sintering time of silicon nitride was found to be $3 \cdot 10^{-12} T d_p^3 \exp(53.65/T)$ ($\pm 20\%$), where the primary particle size d_p is in nm and the temperature in K.

Table 5.1. Results of the PCS measurements in the silicon nitride flame. H is the distance between the nozzle and the IR laser beam center, h is the distance between the CO_2 laser beam center (see fig. 5.4) and the HeNe laser beam heart, d the free molecular regime PCS diameter, λ the mean free path, v the particle velocity and η the gas viscosity.

h [mm]	T [K]	D [10^{-9} m/s ²]	v [m/s]	η [10^{-5} Pa.s]	λ [μm]	d [nm]
$H=2.5$						
-1.3	2216	50	-	5.1	1.1	57
-1.1	2252	39	-	5.2	1.2	66
-1.0	2289	45	-	5.3	1.2	62
-0.5	2372	14	7.7	5.4	1.2	108
0.0	2639	16	5.4	5.9	1.4	115
1.0	2776	20	4.5	6.2	1.5	109
1.5	2767	9.3	7.6	6.2	1.5	157
2.0	2692	6.1	5.7	6.0	1.5	189
$H=4.5$						
-1.3	1938	110	-	4.6	0.95	35
-1.1	1981	57	-	4.7	0.98	50
-1.0	2024	43	-	4.8	1.0	58
-0.8	2113	56	-	5.0	1.1	52
-0.5	2190	31	-	5.1	1.1	73
0.0	2496	20	6.4	5.7	1.3	99
1.0	2890	16	5.4	6.4	1.6	126
1.5	2919	6.5	6.4	6.5	1.6	196
2.0	2833	6.1	4.7	6.3	1.6	198
$H=6.5$						
-1.3	2172	220	-	5.1	1.1	27
-1.1	2239	150	-	5.2	1.1	34
-1.0	2307	45	-	5.3	1.2	62
-0.5	2580	35	-	5.8	1.4	77
0.0	2903	13	8.8	6.4	1.6	136
1.0	3024	14	5.2	6.7	1.7	137
1.5	2996	6.7	6.2	6.6	1.7	196
2.0	2910	6.0	4.2	6.5	1.6	203
$H=11.5$						
-1.3	2225	140	-	5.2	1.1	34
-1.1	2393	78	-	5.5	1.3	49
-1.0	2561	51	9.1	5.8	1.4	64
-0.8	2667	48	-	6.0	1.4	67
-0.5	2765	9	13.2	6.2	1.5	161
0.0	3148	16	10.6	6.9	1.8	148
1.0	3341	11	5.3	7.3	2.0	168
1.5	3417	7.1	5.5	7.4	2.0	210
2.0	3366	5.4	4.1	7.3	2.0	239

References

- R.C.A. Bauer, J.G.M. Becht, F.E. Kruis, B. Scarlett, J. Schoonman (1991) Laser-Chemical Vapor Precipitation of Submicrometer Silicon and Silicon Nitride Powders from Chlorinated Silanes, *J. Am. Ceram. Soc.*, **74**, 2759.
- W.L. Flower (1983) Measurement of the Diffusion Coefficient for Soot Particles in Flames, *Phys. Rev. Lett.*, **51**, 2287.

- S.K. Friedlander (1976) *Smoke, Dust and Haze*, Wiley, New York, 6.
- N.A. Fuchs (1964) *The Mechanics of Aerosols*, Dover, New York, Chapter 2.
- C. Greskovich and J.H. Rosolowski (1976) Sintering of Covalent Solids, *J. Am. Ceram. Soc.*, **59**, 336.
- W.D. Kingery, H.K. Bowen, D.R. Uhlman (1976) *Introduction to Ceramics*, Wiley, New York, Chapter 10.
- F.E. Kruis (1993) *Particle Formation in a Laser Heated Aerosol Reactor*, Thesis Delft University of Technology.
- F.E. Kruis, J.C.M. Marijnissen, J. Schoonman, B. Scarlett (1993a) A Simple Model for the Evolution of the Characteristics of Aggregate Particles Undergoing Coagulation and Sintering, *Aerosol Sci. Technol.*, **19**, 514.
- F.E. Kruis, J.C.M. Marijnissen, J. Schoonman, B. Scarlett (1993b) Particle Formation in a Laser-heated Aerosol Reactor with Application to Silicon and Silicon Nitride Synthesis, in: *Synthesis and Measurement of Ultrafine Particles*, J.C.M. Marijnissen and S. Pratsinis (eds.), Delft University Press, 91.
- N. Lhuissier, G. Gouesbet, M.E. Weill (1989) Extensive Measurements on Soot Particles in Laminar premixed Flames by QELSS, *Combust. Sci. Technol.*, **67**, 17.
- S.S. Penner and P.H.P. Chang (1981) Particle Sizing in Flames, in *Combustion in Reactive Systems, Progress in Astronautics and Aeronautics 76*, eds. J.R. Bowen, N. Manson, A.K. Oppenheim and R.I. Soloukin, 1.
- R.C. Reid, J.M. Prausnitz, B.E. Poling (1987) *The Properties of Gases and Liquids*, McGraw-Hill, New York, Chapter 9.
- I.L. Tuinman, M.A. van Drunen, J.C.M. Marijnissen, B. Scarlett (1996) submitted to *Aerosol Sci. Technol.*
- Y. Xiong, S. Pratsinis, A.W. Weimer (1992) Modeling the Formation of Boron Carbide Particles in an Aerosol Flow Reactor, *AIChE Journal* **38**, 1685.

In-line measurements of monodisperse sulfur sol formation

6

Abstract

This chapter deals with homogeneous nucleation from solution. The supersaturation was very high, where the reactant concentration was still relatively low. The system investigated was the formation of a monodisperse sulfur sol by chemical reaction, i.e. by acidifying thiosulfate solutions. The rate determining step of sol formation is the rate of dissolved sulfur formation, and not nucleation (see chapter 5) or growth. The experiments were performed as a pilot study for PCS measurements of crystallization from solution.

It is shown that it is possible to follow the particle growth in-line and with reasonable precision, and to get information on the particle number concentration as long as the size distribution is narrow. The overall growth rate obtained from the measurements together with number concentrations found from literature, $d[S]/dt = 0.44 [H^+]_0 [S_2O_3^{2-}]_0^2$ [mol l⁻¹s⁻¹], resembled the one mentioned by Johnston and McAmish (1973). The overestimation of the average particle diameter is probably due to the type of measuring technique. PCS measures the hydrodynamic particle size, which is probably larger than the size of the sulfur particle alone due to stabilizing ions and water molecules adsorbed at the surface.

Contrary to the literature data, the induction time, which is defined as a period in which nothing can be measured by PCS, was found to be several hundreds of seconds. This is to be expected since in this work, we only measured colloidal particles, while in literature all sulfur molecules were followed, dissolved or not. Probably, in the induction stage, the dissolved sulfur is formed. When the concentration of this molecular sulfur reaches a critical value the actual sol formation starts. This supports the idea of a three stage mechanism for monodisperse particle formation.

6.1 Introduction

Generally, precipitation processes result in polydisperse particles, because nucleation and growth both take place at the same time. However, for many purposes, e.g. for photographic materials, monodisperse particles are needed. One of the oldest investigated processes to make monodisperse particles is the precipitation of sulfur by adding hydrochloric acid to thiosulfate solutions (e.g. Zaiser and La Mer 1948). Monodisperse particles are formed because sulfur is slowly released into the disperse phase by chemical reaction. After the nuclei have been formed, the supersaturation drops significantly and becomes low enough to prevent further nucleation, while particle growth continues. Thus, chemical reaction is rate determining.

This chapter deals with this process in order to investigate whether it is possible to follow the kinetics of sulfur sol formation by using photon correlation spectroscopy (PCS) in-line as a monitoring system. It is used as a pilot study for the next chapter, in which barium sulfate precipitation is investigated. Sulfur was chosen, because the kinetics are well known, it forms a monodisperse sol, the particles formed are in the submicrometer range and the particle concentration is low

enough to make PCS experiments possible without diluting the samples (Zaiser and LaMer 1948, Johnston and McAmish 1973, Baraké 1994).

In the late forties, La Mer and co-workers used obscuration measurements to investigate sulfur sol formation. Since the sulfur particles are spherical, Mie theory is well suited to extract the particle size from these measurements. In 1973, Johnston and McAmish reproduced the experiments while using S-35 labeled thio-sulfate. Thus, they were able to follow the kinetics by tracing this radioactive element.

In this chapter, the growth of the sulfur particles is followed by PCS. In order to calculate the overall growth rate $d[S]/dt$, the number concentration was necessary as well as the particle size. The number concentration was obtained from literature (Kenyon and LaMer 1973, Barnes et al. 1947), but it was checked with the absolute time averaged scattering intensities found from the PCS measurements. From these intensities relative number concentrations can be deduced, if it is assumed that the number concentration does not change during the measurements.

This chapter starts with a short theoretical section which contains the kinetic expressions for sulfur precipitation (6.2). This is followed by a description of the experimental procedures (6.3) and the discussion of the results (6.4). Finally, some conclusions are drawn in 6.5.

6.2 Theory

6.2.1 Sulfur precipitation

Zaiser and La Mer (1948) distinguish three stadiums in the formation and growth of sulfur sols (fig 6.1).

- I. The first is the *homogeneous reaction*. The reaction starts as soon as the acid and thiosulfate are mixed together and results in dissolved sulfur. This stadium is stopped when the sulfur solution is supersaturated enough to form stable nuclei.
- II. The second step is *condensation*. At a certain sulfur concentration C_{nuc} , rapid condensation of the dissolved sulfur molecules results in a decrease of the molecular sulfur concentration. In other words, the supercritical clusters rapidly 'consume' the dissolved sulfur molecules. This results in a fast decrease in nucleation rate until a level at which no significant formation of new critical clusters (nuclei) takes place.
- III. The third step is the *heterogeneous stadium*. This stadium begins when the concentration has dropped below the concentration C_{nuc} at which the nucleation rate significantly differs from zero. The sulfur particles slowly grow by diffusion of dissolved sulfur to the particle surface. Monodispersity results from a slow release of solvated sulfur, which is consumed by the colloidal particles, and absence of nucleation and coagulation in this stadium.

The induction time t_{ind} is defined as the time at which some parameter determining the progress of particle formation and growth can be detected. For PCS, the induction time period is expected to be at the beginning of stage III, because at this time the particles have reached a size at which the scatter enough light to be detected (approximately 100 nm at the given angle and concentration, see section 6.2.2).

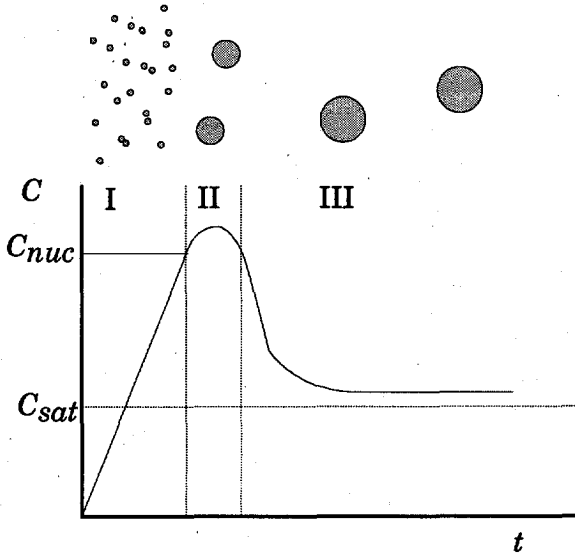
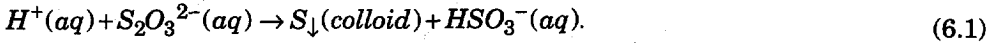


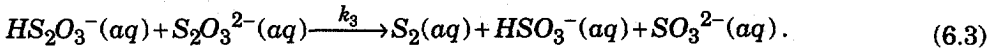
Fig 6.1. The three stages mechanism by La Mer which explains monodisperse particle size distributions (Sugimoto 1987). In stage I, dissolved sulfur is formed by chemical reaction. In stage II the colloidal critical clusters (nuclei) are formed, which grow steadily in stage III by diffusion of dissolved sulfur to the surface. The supersaturation is too low to enable formation of new particles.

Reactions

The overall reaction in sulfur sol formation is (Johnston and McAmish 1973),



Based on the mechanism proposed by Dinegar et al. (1951), Johnston and McAmish (1973) found the following mechanism to be consistent with their experimental findings,



They suggested that the S_2 units condense to form S_8 units, from which, finally, colloidal sulfur is formed. The rate determining step is attributed to reaction (6.3) and hence, the reaction rate for colloidal sulfur formation will be,

$$\frac{d[S_2]}{dt} = k_3 [HS_2O_3^-] [S_2O_3^{2-}]. \quad (6.4)$$

Since Johnston and McAmish (1973) observed a third order rate dependence, namely first order in H^+ and second order in $S_2O_3^{2-}$, they concluded that the ionization constant K for bithiosulfate ion formation must be large enough to rewrite its concentration in the following form,

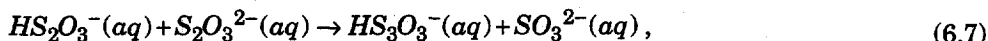
$$[HS_2O_3^-]_0 = \frac{[H^+]_0 [S_2O_3^{2-}]_0}{K}, \quad (6.5)$$

where the subscript 0 indicates starting concentration. Thus, at low conversion of thiosulfate the overall rate equation can be written as a pseudo 0th order equation, because the concentrations of thiosulfate and H^+ stay approximately the same,

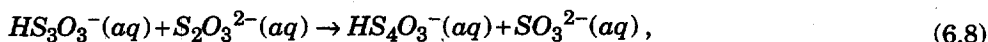
$$\left(\frac{d[S]}{dt}\right)_0 = k_{exp}[H^+]_0[S_2O_3^{2-}]_0^2. \quad (6.6)$$

Here, S has been chosen in stead of S_2 in order to avoid uncertainties about the exact molecular structure of the sols, which is not relevant for the kinetics of their formation. Hence a linear increase in time is expected for the sulfur concentration at low conversion.

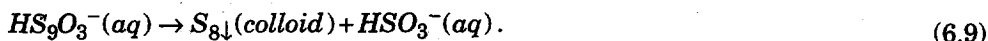
An alternative rate equation was proposed by Davis (1958) who describes a series of reactions,



followed by,



and so on, finishing with,



Both (6.3) and the rate determining step (6.7) result in eq. (6.6) for the description of the precipitation kinetics.

6.2.2 Mie profiles of single sulfur particles

The light intensity scattered by single spherical particles can be calculated with Mie theory. Since the particles we are interested in have the same size range as the incoming laser wavelength only this rigorous solution of the Maxwell equations can be used to calculate the scattered intensities as a function of scattering angle and particle size. In this work this has been done by the computer program Mie5u (Boxman et al. 1992), which is based on a software routine given by Bohren and Huffman (1983). The refractive index of sulfur is 1.51 relative to water (Kenyon and La Mer 1949). The results of the calculations for sulfur are shown in fig. 6.2. The figure shows the peaked behavior of the scattered intensity between 300 and 900 nm (linear scale) and the enormous range in scattered intensity (log scale).

6.3 Experimental

Five ml PCS sample containers were filled with sodium thiosulfate and hydrochloric acid at varying concentrations (table 6.1). The ionic strength was set at 0.035 by adding potassium chloride in order to prevent an influence of the kinetic salt effect¹⁾. Solutions of potassium chloride, sodium thiosulfate and hydrochloric acid were first filtered through 0.2 μ m Millipore Sterivex disposable filters and then shaken in the sample container. This moment was taken to be $t=0$. The samples were thermostated at 22°C.

¹⁾ The kinetic salt effect arises from shielding of reacting dissolved ions by other ions present in the solution (Atkins 1986).

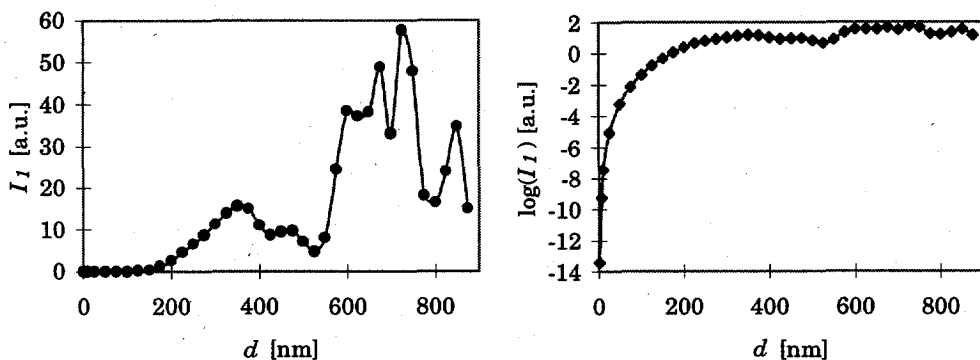


Fig. 6.2. Calculated scattered intensities for single sulfur particles in water. Wavelength: 488 nm, scattering angle 45° . Note that the intensity differs 14 orders of magnitude between 1 and 300 nm as can be seen on the plot with the log scale (right).

They were measured by the Brookhaven setup described in chapter 4, with the Argon ion laser set at 100 mW on 488 nm and the scattering angle at 45° . The sample time was 5 μ s and the delay time ratio 1:1.3. Every minute a measurement was made, yielding an autocorrelation function. Five autocorrelation functions were added in order to obtain a sufficient signal to noise ratio. The ones that suffered notably from dust particles, as could be determined from the ratio measured to calculated baseline, were discarded. The first measurements could be done once the measured scattered light intensity exceeded about 800 counts per second (Hz). Of course, the samples were not stirred during the measurements, but between some of the measurements they were gently shaken to prevent settling.

The thus obtained autocorrelation functions were evaluated using the cumulant fit method implemented in the correlator software (see section 2.3.1). The experiments were stopped when the particle size did not change notably anymore, which happened after about 2 hours.

6.4 Results and discussion

In table 6.1, the initial concentrations and some of the results are shown. The values for the polydispersity index $P.I.$ are relatively small, about 0.09, which means that the relative standard deviation of the particle size distribution is smaller than 0.3. Hence, the particles formed are almost monodisperse. In fig. 6.3, the intensity weighted average diameter found from the second cumulant fit is shown against the reaction time t . The appendix shows more details of the measurements. It should be noted that at low intensities, the error in the diameter obtained and especially in the polydispersity index $P.I.$ is relatively large. Generally, the $P.I.$ is overestimated in such cases. Fig 6.2 shows a fast increase of d in time at short reaction times, which levels off at longer times. All four experiments give about the same results for the average particle size, but experiment B2 results in notably smaller particles than B5.

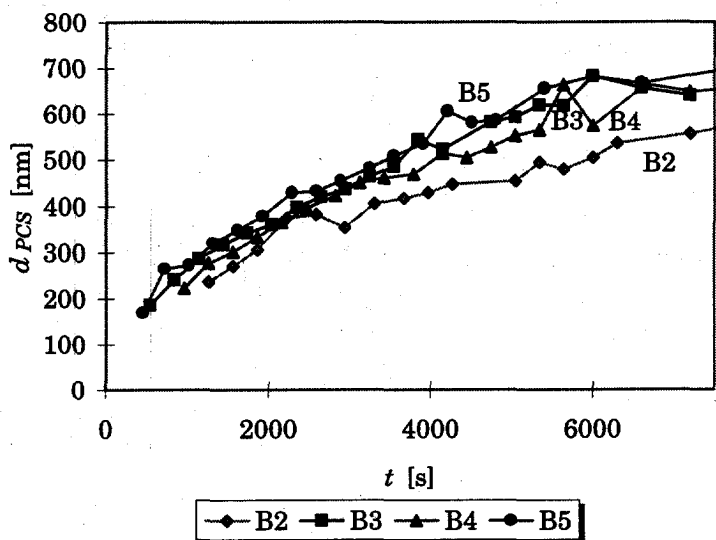


Fig. 6.3. Average diameters found by PCS for the precipitated sulfur particles in experiments B2 -B5.

Concentration profiles

The number concentration of particles, which is necessary to convert the experimental diameters into concentrations of precipitated sulfur $[S]$, has been extrapolated or interpolated from literature data obtained from experiments performed at the same reaction conditions (Kenyon and La Mer 1949, Barnes et al. 1947). The diameter is related to the sulfur concentration via,

$$c = \frac{\pi N \rho d^3}{6 M}, \quad (6.10)$$

where N is the number concentration of the sulfur particles, ρ the density and M the molar mass. Thus, the concentration is proportional to the third power of the diameter.

As shown in fig. 6.3, the particle size profile as a function of time is about the same for each experiment. However, the concentration of precipitated sulfur $[S]$ differs largely. In order to calculate $[S]$ from the diameters, the particle number concentration was assumed to remain constant in each experiment. Thus, agglomeration, Ostwald ripening and nucleation in the growth stage were ignored. The average scattered intensity, obtained from the PCS measurements is a good indication of the concentration.

Using Mie theory it is possible to convert this intensity into a (relative) concentration. The scattered intensity as a function of reaction time t and diameter d are shown in the figures 6.3 and 6.5. It is, unfortunately, not possible to directly calculate $d[S]/dt$ from the intensity data, because no absolute values for $d[S]$ can be calculated from the intensity units measured. In fig. 6.4, it is shown that the averaged intensities indeed are proportional to the number concentrations mentioned in literature.

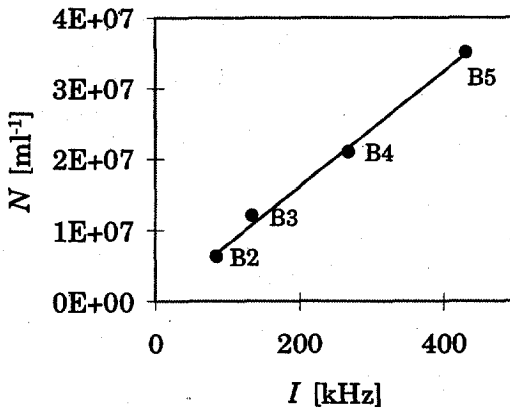


Fig. 6.4. Literature (Kenyon and La Mer 1949, Barnes et al. 1947) number concentrations as function of the measured averaged intensity of the particles between 200 and 550 nm.

Table 6.1. Experimental conditions for the experiments B2 - B5. The ionic strength was set to 0.035 by adding sufficient potassium chloride. The induction time is found from the linear fits to the concentration profiles (fig. 7.7) and P.I. is the polydispersity index (section 2.3.1) averaged for all experiments. Errors are based on 95% confidence intervals.

Exp.	[Na ₂ S ₂ O ₃] [mol l ⁻¹]	[HCl] [mol l ⁻¹]	<i>t</i> _{ind} [·10 ² s]	P.I.-avg	d[S]/dt [mol l ⁻¹ s ⁻¹]	<i>k</i> _{exn} [l ² mol ⁻² s ⁻¹]
B2	0.0025	0.0025	7.3 [±3.7]	0.07	5.1 [±0.58]·10 ⁻⁹	0.33 [±0.04]
B3	0.0050	0.0025	6.5 [±2.7]	0.09	2.8 [±0.43]·10 ⁻⁸	0.44 [±0.07]
B4	0.0025	0.0050	7.1 [±1.5]	0.11	1.4 [±0.13]·10 ⁻⁸	0.43 [±0.04]
B5	0.0050	0.0050	4.8 [±1.7]	0.08	4.7 [±0.45]·10 ⁻⁸	0.37 [±0.04]

Table 6.2 shows the average scattered intensity of sulfur particles between 200 and 550 nm. The average was obtained by adding the intensity obtained for the experiments at diameters between 200 and 550 nm and dividing by the number of measurements. For the experiments B2-B4, the average intensity relative to that of B5 (*I*_{rel}) is almost equal to the number concentration relative to that of B5 (*N*_{rel}). Therefore, *I*/*N* has approximately the same value for all experiments. This suggests that in this size range the number concentration is constant and indeed the same as given by Kenyon and La Mer (1949) and Barnes et al. (1947) who gave the number concentration *N* as a function of the starting concentration. Additionally, the fact that the profiles in fig. 6.6 qualitatively follow the Mie profile, indicates that all measurements were performed in stage III (section 6.2), because the number concentration is constant.

Fig 6.5 shows the scattered average intensity monitored by the photomultiplier used for PCS as function of the measured PCS diameter. The experimental profiles qualitatively follow the Mie profile in the size range 200 to 550 nm. When the particle size exceeds about 550 nm, the number concentration decreases, may be

due to Ostwald ripening or agglomeration. This can be observed in fig. 6.6. Beyond this size, the measured intensities deviate strongly from the Mie profile.

Table 6.2. The average scattered intensity of sulfur particles between 200 and 550 nm. The intensity relative to B5 is almost equal to the number concentration relative to that of B5. Therefore, I/N has about the same value for all experiments.

	I_{avg} [kHz] 200-550 nm	N [ml ⁻¹]	I_{rel} (relative to B5)	N_{rel} (relative to B5)	I/N ($\cdot 10^{-5}$)
B2	85	$6.3 \cdot 10^6$	0.20	0.18	1.35
B3	268	$2.1 \cdot 10^7$	0.62	0.60	1.28
B4	134	$1.2 \cdot 10^7$	0.31	0.34	1.12
B5	431	$3.5 \cdot 10^7$	1.00	1.00	1.23

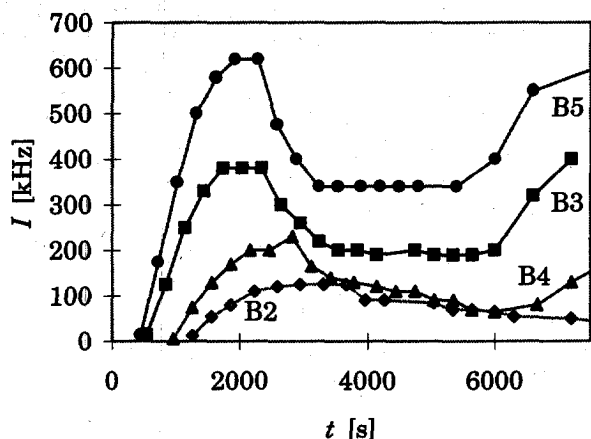


Fig 6.5. Scattered average intensity monitored by the photomultiplier used for PCS as function of the measuring time. Scattering angle was 45°.

The qualitative resemblance increases if one realizes that PCS probes the hydrodynamic diameters. Since the particles are stabilized by ions and water molecules which are adsorbed at their surfaces, their sizes increase and, therefore, they are expected to diffuse somewhat slower than the 'pure' sulfur particles would do. The Mie profile does not account for it, because the optical particle size is determined by the interface at which the refractive index changes. Thus, the measured curves in fig. 6.6 should be shifted somewhat to the left.

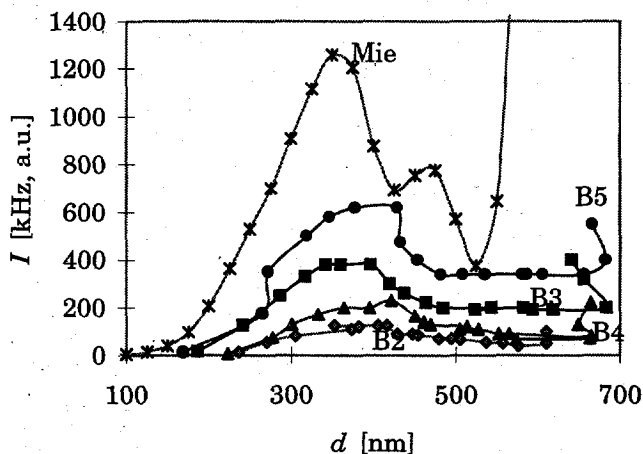


Fig 6.6. Scattered average intensity (in thousands of counts per second) monitored by the photomultiplier used for PCS as function of the measured PCS diameter. The Mie profile, which is calculated for single particles, is given in units chosen such that it fits in the same plot. Beyond 550 nm, the measured profiles deviate from the theoretical one.

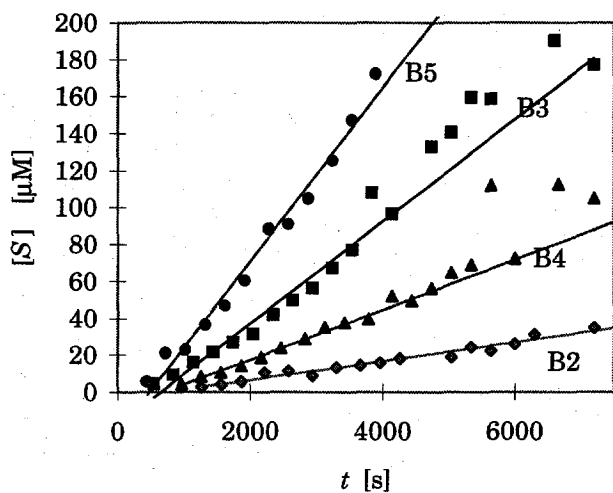


Fig. 6.7. Concentration of precipitated sulfur in $\mu\text{mol l}^{-1}$ as function of the reaction time. The slope $d[S]/dt$ equals $k_{exp}[H^+]_0[S_2O_3^{2-}]_0^2$.

From the slopes of fig. 6.7, the kinetic constant k_{exp} was calculated. As shown in table 6.1, the values for B2-B5 at 22°C are 0.33, 0.44, 0.43 and 0.37 $\text{l}^2\text{mol}^{-2}\text{s}^{-1}$, respectively. In order to combine all the data obtained from the four experiments a plot was constructed of $[S]/[S_2O_3^{2-}]_0^2[H^+]_0$ minus the calculated intercepts obtained from the fits shown in fig. 6.7, against time. Thus, a straight line through the origin with slope k_{exp} is expected. This is shown in fig. 6.8. The resulting k_{exp} is 0.44

$[\pm 0.02] \text{ l}^2 \text{ mol}^{-2} \text{ s}^{-1}$, where the uncertainty is obtained from the 95% confidence interval. Johnston and McAmish (1973) found $0.336 \pm 0.018 \text{ l}^2 \text{ mol}^{-2} \text{ s}^{-1}$ at 25°C .

Without the use of the literature number concentrations, but with the help of the average measured intensities, the relative values for k_{exp} obtained from curves comparable to 6.6 were for the experiments B2-B5, 0.83, 1.06, 1.14 and 1.00, respectively. These can be compared to the relative values found from using literature number concentrations for B2-B5: 0.87, 1.18, 1.16 and 1.00. Thus, roughly, the same results are obtained.

Thus, with the PCS-experiments, for the rate constant, a value which is approximately 24% larger than the literature is found. This overestimation can be expected because PCS probes the hydrodynamic diameter. Hence, the size is overestimated and thus the precipitated sulfur concentration even more, since it is related to the size with the third power (eq. 6.10).

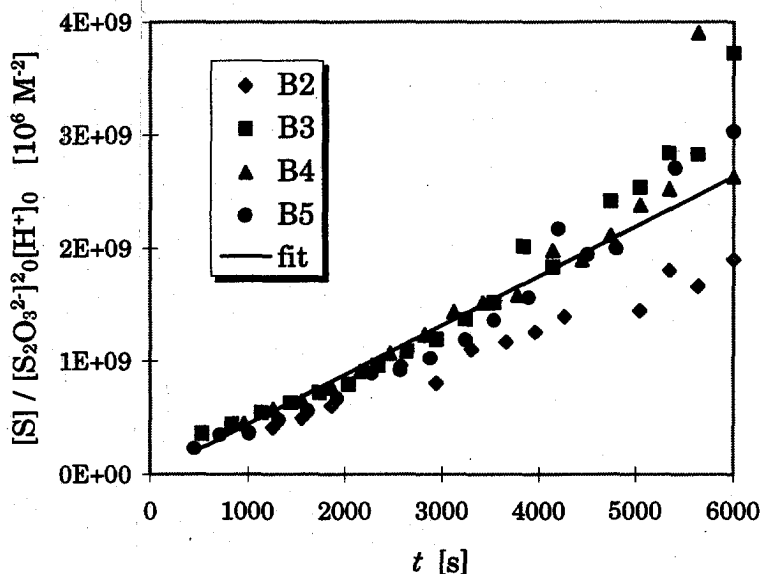


Fig 6.8. Combined analysis of all four experiments. The slope equals the reaction rate constant k_{exp} .

Contrary to Johnston and McAmish (1973), who found plots comparable to those in fig. 6.7 by measuring the actual concentration changes, but with lines through the origin, we found induction times of several hundreds of seconds. The difference between the two types of experiments is that we only measured colloidal particles, where they followed all sulfur formed, irrespective of whether it was dissolved or not. A logical explanation seems that, in the induction time stage, only molecular dissolved sulfur is formed.

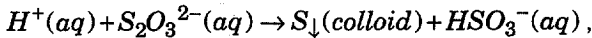
It was chosen to use the fits in fig. 6.7 to find the induction time, because with this technique, the induction time was not determined by one single measurement. However, fig. 6.5 qualitatively supports the findings of the induction times found from the fits.

PCS is not able to follow dissolved sulfur molecules, and is therefore not able to monitor anything until stage II or III starts. Probably only events in stage III are

monitored, since the particle number concentration stays constant, as has been found from fig. 6.6, and the particles measured are already over 150 nm. The induction time decreases at increasing reaction rate, but is not inverse proportional to it. When the concentration of the molecular sulfur reaches a critical value the actual sol formation starts and PCS measurements can be made. This supports the three stage mechanism, shown in fig. 6.1, proposed by Zaiser and La Mer (1948).

6.5 Conclusions

PCS measurements are well suited for in-line measurement of sulfur sol formation from thiosulfate in acid. Particle size and kinetics can be followed accurately. The reaction rate constant for the reaction,



was found to be 0.44 ± 0.02 (95% confidence) $l^2 \text{mol}^{-2} \text{s}^{-1}$ at 22°C and an ionic strength of 0.035, while literature (Johnston and McAmish 1973) gives 0.336 ± 0.018 $l^2 \text{mol}^{-2} \text{s}^{-1}$ at 25°C . The higher value obtained here, is attributed to the fact that not the diameter of pure sulfur particles is probed but their hydrodynamic diameter, which is larger due to adsorption of ions and water molecules at the particle surface.

When the particle size exceeds about 550 nm, the number concentration decreases, may be due to Ostwald ripening or agglomeration.

Contrary to Johnston and McAmish (1973) we found an induction time of several hundreds of seconds. This is to be expected since we only measured colloidal particles, where they followed all sulfur molecules, dissolved or not. Probably, in the induction time stage, the molecular dissolved sulfur is formed. When the concentration of this molecular sulfur reaches a critical value the actual sol formation starts. This supports the three stage mechanism proposed by Zaiser and La Mer (1948).

6.A Appendix*Table 6.A.1. Measured intensities, PCS-diameters, polydispersity indexes and the calculated sulfur concentrations for the experiments B2 - B5. Note that at low intensities the P.I. is generally overestimated.*

B2					B3				
<i>t</i> [s]	<i>I</i> [kHz]	<i>d</i> [nm]	<i>P.I.</i>	[<i>S</i>] [μM]	<i>t</i> [s]	<i>I</i> [kHz]	<i>d</i> [nm]	<i>P.I.</i>	[<i>S</i>] [μM]
1260	13	236	0.13	2.6	540	16	186	0.13	4.3
1560	55	270	0.14	4.0	840	125	241	0.00	9.4
1860	80	305	0.03	5.7	1140	250	286	0.00	15.8
2220	110	373	0.15	10.5	1440	330	317	0.00	21.4
2580	120	382	0.00	11.2	1740	380	342	0.14	26.8
2940	125	352	0.18	8.8	2040	380	360	0.20	31.4
3300	125	405	0.00	13.4	2340	380	397	0.10	42.0
3660	125	416	0.00	14.5	2640	300	420	0.00	49.7
3960	90	429	0.15	15.9	2940	260	437	0.15	56.3
4260	90	447	0.11	18.0	3240	220	464	0.18	67.2
5040	85	454	0.23	18.9	3540	200	485	0.00	76.8
5340	70	494	0.02	24.4	3840	200	544	0.00	108.0
5640	70	480	0.00	22.2	4140	190	523	0.16	96.3
6000	65	505	0.11	26.0	4740	200	583	0.19	133.0
6300	55	537	0.00	31.2	5040	190	594	0.03	140.7
7200	50	557	0.05	34.8	5340	190	619	0.05	159.6
7800	40	576	0.05	38.6	5640	190	618	0.00	158.8
8520	50	610	0.00	45.8	6000	200	684	0.05	214.8
9120	100	610	0.05	45.9	6600	320	657	0.18	190.3
					7200	400	641	0.16	177.1
B4					B5				
<i>t</i> [s]	<i>I</i> [kHz]	<i>d</i> [nm]	<i>P.I.</i>	[<i>S</i>] [μM]	<i>t</i> [s]	<i>I</i> [kHz]	<i>d</i> [nm]	<i>P.I.</i>	[<i>S</i>] [μM]
960	6	223	0.25	4.2	450	14	169	0.07	5.4
1260	75	277	0.22	8.2	720	175	265	0.09	20.8
1560	130	300	0.15	10.4	1020	350	272	0.20	22.5
1860	170	333	0.17	14.1	1320	500	319	0.04	36.3
2160	200	365	0.11	18.6	1620	580	347	0.02	46.7
2460	200	395	0.13	23.7	1920	620	378	0.00	60.4
2820	230	422	0.09	28.8	2280	620	429	0.12	88.3
3120	165	450	0.00	35.1	2580	475	433	0.18	90.8
3420	140	461	0.20	37.7	2880	400	454	0.01	104.6
3780	130	469	0.00	39.7	3240	340	482	0.10	125.4
4140	120	514	0.17	52.1	3540	340	508	0.00	147.1
4440	110	505	0.00	49.4	3900	340	536	0.16	172.0
4740	110	527	0.10	56.3	4200	340	606	0.12	249.0
5040	90	552	0.11	64.7	4500	340	581	0.22	220.1
5340	90	565	0.15	69.1	4800	340	587	0.05	226.7
5640	70	663	0.19	112.1	5400	340	656	0.00	315.6
6000	65	574	0.00	72.5	6000	400	682	0.00	356.2
6660	80	664	0.03	112.7	6600	550	667	0.00	332.1
7200	130	649	0.06	105.0	8580	650	726	0.14	428.0
8400	220	664	0.19	112.7	9000	700	711	0.01	402.8

References

- P.W. Atkins (1986) *Physical Chemistry*, third edition, Oxford University Press, Oxford.
- M. Baraké (1994) *In Situ Meting van Dynamische Submicrometer Systemen met Behulp van Quasi-Elastische Lichtverstrooiing* (in Dutch), chapter 7.
- M.D. Barnes, A.S. Kenyon, E.M. Zaiser, V.K. La Mer (1947) *J. Coll. Sci.* **2** 349-359.
- C.F. Bohren and D.R. Huffman (1983) *Absorption and Scattering of Light by Small Particles*, John Wiley and Sons, New York, Appendix A.
- A. Boxman, A. Haket and P.J.T Verheijen (1992) *Mie5u* computer program (test routine for *Roma*, see A. Boxman (1992) *Particle Size Measurement for the Control of Industrial Crystallizers*, Ph.D. thesis Delft University of Technology).
- R.H. Dinegar, R.H. Smellie, V.K. La Mer (1951) Kinetics of the Acid Decomposition of Sodium Thiosulfate in Dilute Solutions, *J. Am. Chem. Soc.* **73**, 2050-2054.
- F. Johnston, L. McAmish (1973) A Study of the Rates of Sulfur Production in Acid Thiosulfate Solutions Using S-35, *J. Coll. Int. Sci.* **42**, 112-119.
- A.S. Kenyon, V.K. La Mer (1949) Light Scattering Properties of Monodispersed Sulphur Sols, *J. Coll. Sci.* **4**, 163-184.
- T. Sugimoto (1987) Preparation of Monodispersed Colloidal Particles, *Adv. Coll. Int. Sci.* **28**, 65-108.
- E.M. Zaiser, V.K. La Mer (1948) The Kinetics of the Formation and Growth of Monodispersed Sulfur Hydrosols, *J. Coll. Sci.* **3**, 571.

Barium sulfate precipitation: Crystallization kinetics and the role of the additive PMA-PVS¹⁾

7

Abstract

Barium sulfate has a low solubility and a very high specific interfacial energy. Therefore, at the relatively low supersaturation of 25, nucleation takes place exclusively heterogeneously. The precipitation of barium sulfate was investigated by photon correlation spectroscopy (PCS) measurements of the growing crystals combined with electrical conductivity measurements of the mother solution. The crystal size could be studied because many small silica seeds (36 nm) were added to the solution. Therefore, heterogeneous nucleation did not take place on the walls and on the stirrer, which is usually the case, but on the seeds. Hence, the growth of the crystals which had nucleated on the seeds could be studied by PCS.

In order to avoid the ill-conditioned inversion of the measured raw data, the autocorrelation functions, a population balance model was used to calculate these functions with the help of a kinetic model taken from literature (Van der Leeden 1991). The measured and the calculated autocorrelation functions should coincide and adjustable parameters were found from a least square fit. Thus, the model acted as an *observer* for the precipitation process.

The measurements revealed that nucleation is strongly enhanced by PMA-PVS (polymaleic acid - polyvinyl sulfonic acid). Thus, more crystals are formed, resulting in a smaller average crystal size of the end product. But once the crystals are formed, their growth rate is retarded. The mechanism for this is adsorption of the polymer molecules on the crystal surface. However, a simple model which assumes Langmuir adsorption did not describe the kinetics very well.

From the measured data, the nucleation rate was found to be, $J = 1.3 \cdot 10^{10} \exp(-27 / \ln^2 S)$ [$\text{m}^{-3}\text{s}^{-1}$], while the growth rate was $G = 2.6 \cdot 10^{-8} (S-1)^{2/3} S^{1/3} \exp(-29 / 3 \ln S)$ [m s^{-1}]. These results match results taken from the literature quite well.

7.1 Introduction

Barium sulfate precipitation is a process often investigated, primarily because it causes scaling in off-shore drilling operations. Additionally, it has a rich morphology and it is known as an important biomineral (Van der Leeden 1991). It has an extremely low solubility and its growth and nucleation kinetics are well-investigated (Van der Leeden 1991, Angerhöfer 1993), but the nucleation results are often dependent on the particular circumstances due to its heterogeneous character at supersaturations below approximately 400. Earlier attempts to study the size of barium sulfate crystals in the submicrometer-range and on-line have failed (Van der Leeden 1994).

¹⁾ Submitted to *Particle and Particle Systems Characterization*.

PCS and conductivity

Light scattering methods are in principle suited to perform on-line measurements because they do not require extensive sample preparation and because they are relatively fast. The goal of this chapter is to find out whether photon correlation spectroscopy (PCS) measurements of the growing tiny crystals combined with electrical conductivity measurements of the mother solution give enough information to reveal the kinetics of barium sulfate precipitation, at an early stage, from aqueous solutions and the influence of the polyelectrolyte PMA-PVS (polymaleic acid - polyvinyl sulfonic acid) on its kinetics. The measuring techniques will be discussed in sections 7.2.1 and 7.2.2. PMA-PVS at concentrations below 0.05 ppm already influences the crystallization kinetics, probably due to its interaction with the crystal surface. This was shown by Van der Leeden (1991) and explained further in the sections 7.2.3-4.

Model

In addition to the measurements, a numerical model which describes the evolution of the crystal size distribution (CSD) and the supersaturation as a function of time, has been developed. The population balance was solved by the method of moments (De Wolf 1990, Randolph and Larson 1971). The calculated moments of the distribution are used to construct calculated autocorrelation functions which are compared to the measured ones. The model is outlined in section 7.2.5.

Aim

The ultimate goal of the work presented in this chapter is to investigate whether PCS can be used as an in-line measuring system which provides input parameters for a control unit. The raw PCS data, the autocorrelation functions (see chapter 3), can act as signals for control purposes. Hence, the ill-conditioned inversion is avoided. This is discussed in section 7.2.6. The experiments are described in section 7.3 and results are given and discussed in the section 7.4, 7.5 and 7.6. Section 7.7 contains the conclusions.

7.2 Theory**7.2.1 Photon correlation spectroscopy**

The theory of PCS is outlined in chapter 3. As explained, it is difficult to obtain more than two parameters from measured autocorrelation functions if no prior information on the samples is available. In the experiments described in this chapter two modals of the particle size distribution are expected: one from the fraction of silica seeds on which no heterogeneous nucleation has taken place, and one from the growing crystals. Assuming that the seed modal is monodisperse, the autocorrelation function has the form,

$$g(\tau) = F \exp(-D_{seeds} q^2 \tau) + (1 - F) \sum_i f_i \exp(-D_{i,crystals} q^2 \tau), \quad (7.1)$$

where F is the scattered light intensity weighted fraction of seeds and f_i is the scattered light intensity weighted fraction of crystals with diffusion coefficient $D_{i,crystals}$. Since the barium sulfate particles grow on the seeds from nanometer sized critical clusters to several crystals of micrometers, it is very difficult to convert the fraction F into a weight fraction. The reason for this is that the particle size is of

the order of magnitude of the wavelength of the incoming laser light. Therefore only the Mie theory can be used to obtain the scattered light intensity as a function of the scattering angle. This theory, which is valid for spherical particles, shows that the intensity is dependent on particle size, refractive index and scattering angle.

In fig 7.1 it is shown that the dependence of the scattered light intensity on the particle size is very complicated. The scattered intensity of single particles between 100 and 3000 nm covers 4 orders of magnitude and shows an irregularly peaked behavior. It has been calculated by the computer program *Mie5u* (Boxman et al. 1992). Thus, although F contains concentration information, this is difficult to extract.

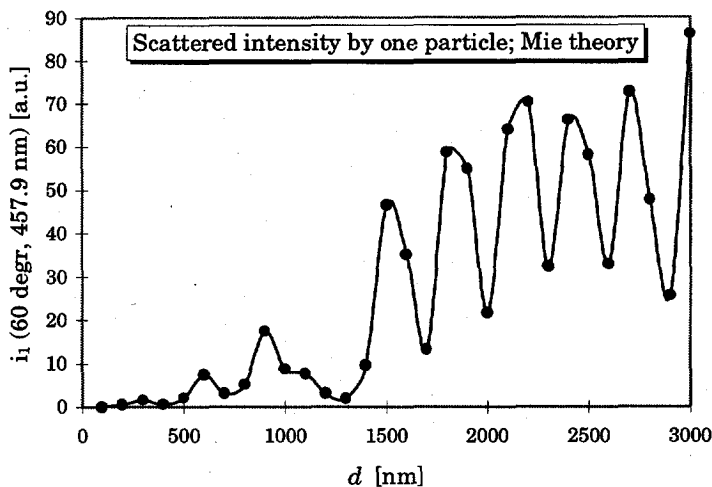


Fig. 7.1. Scattered light intensity of single spherical barium sulfate particles ($m=1.641$) in water as a function of particle diameter for vertically polarized incoming laser light. The wavelength is 457.9 nm and the scattering angle 60°.

7.2.2 Electric conductivity in ionic solutions

The conductivity of solutions depends on the number of ions present, the nature of these ions and their charge. Conductivity, κ_e , and concentration, c , are related via (Atkins 1986, Robinson and Stokes 1959),

$$\kappa_e = \Lambda_m c. \quad (7.2)$$

At low concentrations, the molar conductivity Λ_m equals,

$$\Lambda_m = \Lambda_m^0 - K\sqrt{c}. \quad (7.3)$$

This equation is known as *Kohlrausch's Law*. The constant K can be found from the *Debye-Hückel-Onsager Theory*,

$$K = A + B\Lambda_m^0,$$

$$\text{with } A = \left(\frac{z^2 e F_e^2}{3\pi\eta} \right) \sqrt{\frac{2}{\epsilon RT}}$$

$$\text{and } B = \left(\frac{qz^3 e F_e^2}{24\pi\epsilon RT} \right) \sqrt{\frac{2}{\pi\epsilon RT}}, \quad (7.4)^2$$

where z is the ion charge, e the elementary charge unit, F_e Faraday's constant, η the viscosity, R the gas constant and q equals $\frac{1}{2}$ for a symmetrical electrolyte. Hence the relationship between concentration and conductivity is,

$$\kappa_e(c) = c\Lambda_m^0 - (A + B\Lambda_m^0)c^{\frac{3}{2}}. \quad (7.5)$$

Expressing c in terms of κ requires solution of this cubic equation. The result is,

$$c(\kappa_e) = \left\{ \frac{\Lambda_m^0}{X + Y\Lambda_m^0} \left(1 + 2 \cos \left[\frac{1}{3} \arccos \left(1 - \frac{27\kappa_e (A + B\Lambda_m^0)^2}{2(\Lambda_m^0)^3} + \frac{4\pi}{3} \right) \right] \right) \right\}^2. \quad (7.6)$$

Several assumptions are made in the derivation of this equation. The most important one is that the solution is sufficiently dilute. Hence, the ions do not interact and the concentration of ion pairs is very low compared to the ion concentration. In the experiments described here, the concentrations of barium and sulfate ions were always below $2.5 \cdot 10^{-4}$ M and the concentrations of other ions were much lower. Hence this condition was satisfied.

7.2.3 Precipitation from solution

Precipitation from solution is a two step process. As has been discussed in chapter 2, the first step is the formation of critical clusters, clusters of molecules which have reached a certain critical size. The second step is the growth of these clusters into crystals, which can take place through various mechanisms, such as spiral growth or by two dimensional nucleation on the crystal surfaces. The growth rate G , which is given in meters per second, is also dependent on S but not as strongly as the nucleation rate.

Van der Leeden (1991) gave expressions for the nucleation and growth of barium sulfate from solution. The supersaturation is defined as,

$$S = \sqrt{\frac{[Ba^{2+}][SO_4^{2-}]}{[Ba^{2+}]_{eq}[SO_4^{2-}]_{eq}}}. \quad (7.7)$$

The classical expression for the homogeneous nucleation rate has the following dependence on S (see section 2.3.5),

$$J(S) = k_J S \exp\left(-\frac{B_{3D}}{\ln^2 S}\right), \text{ with } B_{3D} = \frac{\beta_{3D}\sigma^3 V_m}{(kT)^3 \delta^2}. \quad (7.8)$$

²⁾ The value for B given in Atkins' Table 27.3 (p. 672) must be multiplied by q in order to get the right value.

Here, k_J is the pre-exponential factor, β_{3D} a shape factor, σ the specific surface free energy, V_m the molecular volume, k Boltzmann's constant, T the temperature and δ the number of atoms in the molecular formula. However, at the low supersaturations investigated in this work, barium sulfate precipitates mainly on foreign surfaces. For this *heterogeneous* nucleation the interfacial tension is lowered, resulting in a lower value for B_{3D} , while the pre-exponential term decreases and is dependent on the number of nucleation sites available. Nevertheless, heterogeneous nucleation is always faster than homogeneous nucleation, because the exponential term strongly dominates.

The growth rate is determined by two the dimensional nucleation mediated growth mechanism,

$$G(S) = k_G (S-1)^{\frac{2}{3}} S^{\frac{1}{3}} \exp\left(-\frac{B_{2D}}{3 \ln S}\right), \text{ where } B_{2D} = \frac{\beta_{2D} \kappa^2 A_m}{(kT)^2 \delta} \quad (7.9)$$

Here, k_G is the pre-exponential factor, β_{2D} is the two dimensional shape factor, κ the specific edge free energy and A_m the molecular surface.

7.2.4 Effect of PMA-PVS on crystallization kinetics

Experiments (Van der Leeden 1991) showed that PMA-PVS (fig. 7.2) adsorbs on crystal surfaces. Hence, it can decrease the crystal growth rate by sterical interactions. In principle, it can enhance nucleation if it acts as a template for nucleation. Under this assumption, the sulfonic acid groups provide an especially good starting point for nucleus formation because chemically they resemble sulfate ions.

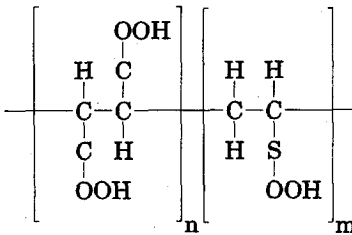


Fig. 7.2. Structure formula of the polyelectrolyte PMA-PVS, a co-polymer of maleic acid and vinyl sulfonic acid, in its uncharged state.

Van der Leeden (1991) found expressions for the growth and nucleation rates for barium sulfate in the presence of additives. The nucleation rate is a sum of the 'normal' rate on heterogeneous nuclei and the nucleation rate on additive molecules, because the additive provides new active centers. Hence, the overall nucleation rate (eq. 7.8) in the presence of an additive becomes,

$$J_a(S,c) = k_J S \left[\exp\left(\frac{B_{3D}}{\ln^2 S}\right) + \frac{c}{N_{3D}} \exp\left(\frac{B_{a,3D}}{\ln^2 S}\right) \right], \quad (7.10)$$

where the subscript a refers to the presence of an additive, c is the additive concentration and N_{3D} the number density of the active centers.

The derivation of the two dimensional nucleation mediated growth rate expression in the presence of an additive is rather elaborate is explained further by Van

der Leeden (1991). She assumed Langmuir adsorption of the additive on the crystal surface, given by,

$$\theta = \frac{kc}{1+kc}, \quad (7.11)$$

where θ is the fractional coverage and k is the Langmuir surface coverage constant. With this expression Van der Leeden (1991) found for the following expression for the growth rate,

$$G_a(S,c) = G(S) \frac{[1+k_{2D}(S)c]^{\frac{1}{3}}}{[1+k_0c]^{\frac{1}{3}} [1+k_s c]^{\frac{2}{3}}}, \quad (7.12)$$

where $G(S)$ can be found from eq. (7.9), k_0 and k_s are the Langmuir surface coverage and step coverage constants, respectively. Furthermore,

$$k_{2D}(S) = k_0 \left(1 + \frac{N_s}{N_{a,2D}} \exp \left[\frac{B_{2D} - B_{a,2D}}{\ln S} \right] \right), \quad (7.13)$$

where $N_{a,2D}$ and N_s are the number concentrations of the active sites on the crystals with and without adsorbed additive molecules, respectively.

For $k_{2D}c \gg 1 \wedge k_0c \gg 1 \wedge k_s c \gg 1$ the growth rate tends to zero as $c^{-\frac{2}{3}}$,

$$G_a(S,c) = G(S) \left[\frac{k_{2D}(S)}{k_0 k_s^2} \right]^{\frac{1}{3}} c^{-\frac{2}{3}}. \quad (7.14)$$

Since the factor k_0 appears both in the numerator and in the denominator, $G_a(S,c)$ is independent of it.

7.2.5 The population balance equation

In order to find the development in the crystal size distribution (CSD) and the supersaturation as a function of time the population balance must be solved. For a batch crystallization process, as in the experiments described in this chapter, this population balance has the following form,

$$\frac{\partial n(L,t)}{\partial t} + \frac{\partial [G(t)n(L,t)]}{\partial L} = 0, \quad (7.15)$$

where L is the characteristic crystal length and n the population density. It has been assumed that the growth rate is independent of the crystal length. Since the particle size was monitored by PCS, which gives only low resolution information, it was not necessary to calculate the total CSD as a function of time. Instead, only the total precipitated mass, which gives the supersaturation, the average PCS diameter and the standard deviation of the size distribution were needed. These parameters follow automatically by solving the population balance equation by the *method of moments* (De Wolf 1990, Randolph and Larson 1971). The moments m_j of the distribution are defined as,

$$m_j(t) \equiv \int_0^{\infty} n(L,t) L^j dL, \quad (7.16)$$

and from this, it is clear that m_0 is the total number of particles per volume, m_1/m_0 the number weighted average crystal size and $\rho k_v m_3$ the total crystal mass per volume unit, where ρ is the crystal density and k_v a shape factor.

Multiplying the population balance equation (7.15) by L^j , integrating over L and using the definition of the moments (eq. 7.16) results in,

$$\frac{dm_j}{dt} = - \int_0^\infty \frac{\partial [G(t)n(L,t)]}{\partial L} L^j dL \quad (7.17)$$

Partial integration of the right hand side of this equation yields,

$$\begin{aligned} \int_{L_0}^\infty \frac{\partial [G(t)n(L,t)]}{\partial L} L^j dL &= [G(t)n(L,t)L^j]_{L=L_0}^{L=\infty} - j \int_{L_0}^\infty G(t)n(L,t)L^{j-1} dL \\ &= -J(t)L_0^j - j \int_{L_0}^\infty G(t)n(L,t)L^{j-1} dL. \end{aligned} \quad (7.18)$$

Substitution of this result in eq. (7.17) gives the moment equations,

$$\begin{aligned} \frac{dm_j(t)}{dt} &= J(t)L_0^j + j \int_{L_0}^\infty G(t)n(L,t)L^{j-1} dL \\ &= J(t)L_0^j + jG(t)m_{j-1}(t). \end{aligned} \quad (7.19)$$

In sum, the method of moments is a technique to transform the population balance equation into a set of ordinary differential equations which describe the dynamics of the moments of the population density.

7.2.6 The forward approach

Because the inversion of the autocorrelation function is very sensitive to noise (chapter 3), extra information is required in order to obtain the crystal size distribution from the measured autocorrelation functions. Here, the conductivity measurements and the kinetic model provide this information. This method avoids the ill-conditioned inversion of the ACFs to crystal size distributions, because the calculation of the ACF from the particle size distribution or the moment distribution is a noise-insensitive forward approach. Therefore, it provides a higher resolution of the crystal size distribution.

A model describing the development of the CSD is an *observer*³⁾ for the precipitation process, as is depicted in fig. 7.3. The ACFs and the measured conductivities act signals which feed the observer system.

7.3 Experimental

7.3.1 Precipitation experiments

Aqueous solutions with a barium sulfate supersaturation of 24.5 were prepared by adding solutions of barium chloride and sodium sulfate to a glass 200 ml reactor containing filtered milli-Q (Millipore) water at pH=8.0. The solubility product at

³⁾ The term *observer* is in this text used for a model in which raw data can be fed. Control engineers reserve the term for process control systems with a state estimator which uses Kalman filtering techniques (Eek 1995, chapter 7). Basically, such an estimator is a dynamic model, which runs on a computer and operates sequentially on the raw measured process input and output data.

25°C is $1.02 \cdot 10^{-10} \text{ M}^2$. The reactor was thermostated at 25.0 °C and stirred at 400 rpm with a glass, L-shaped rod. In order to ensure that in every experiment the same quantity of surface was present for heterogeneous nucleation, Ludox TM 40 (Dupont) silica spheres, which have a PCS-average diameter (see chapter 3) of 36 nm, were added in every experiment at a concentration of 50 µg/ml solution. Hence, the number concentration of these spheres was about 10^{12} per ml. The total volume was 200 ml in each experiment. A schematic view of the set up is shown in fig. 7.4.

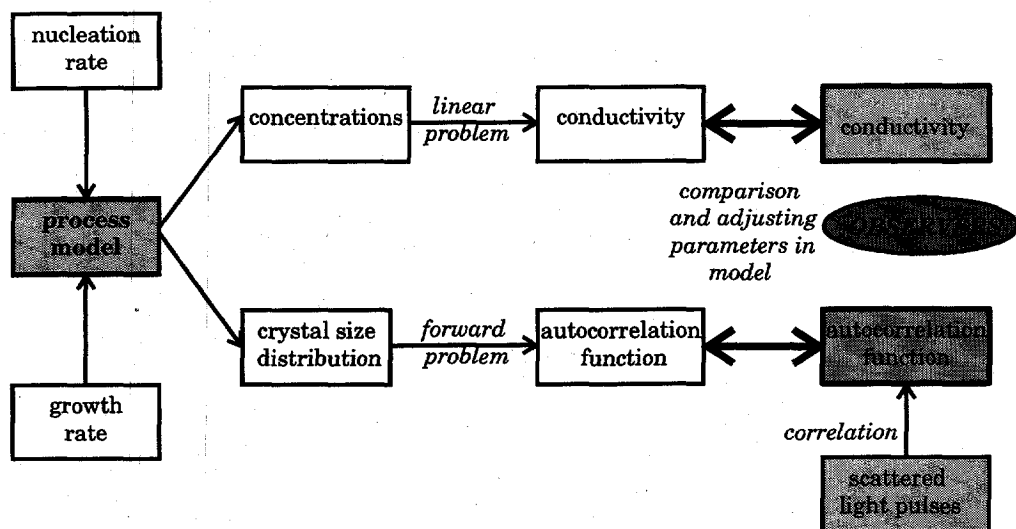


Fig. 7.3. Schematic view of the procedure followed in the forward approach. The process model provides additional information, which results in more information about the crystal size distribution.

The conductivity of the solution during the precipitation process was measured by a Metrohm conductivity cell (Immersion type 6.0901.110, with protective head sawed off in order to enhance response time) and a Metrohm E518 conductometer that was connected to a recorder. The cell was calibrated with known *KCl* solutions. The sequence of adding the solutions was: water, sodium sulfate, silica, [PMA-PVS] and finally barium chloride.

The PCS measurements were done in a BI-200 SM spectrometer and a BI-8000 correlator. The 457.9 nm argon ion laser line (100 mW) was used and the scattering angle was 60°. Samples were measured off-line which was allowed because they were quenched in 1% solutions of PMA-PVS. Experiments showed that the crystal size distribution does not change notably for several hours at this high additive concentration. The samples could be measured on-line, but in order get very accurate measurements a longer measuring time was required than was allowed by the process kinetics. On-line measurements decrease the signal to noise ratio, and, therefore, result in less precise data. Typically 8 repetitive measurements were made of 30 s duration. Those suffering significantly from dust were discarded and the others were summed.

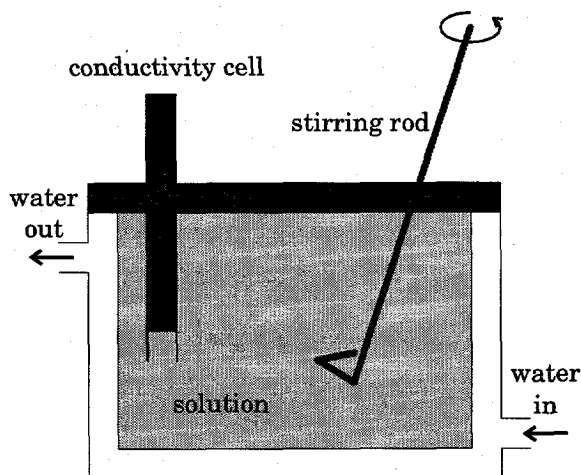


Fig. 7.4. Schematic view of the set up for the precipitation experiments.

The PMA-PVS solutions were freshly made, because the activity decreases appreciably after about 12 hours, probably due to adsorption on the glass walls of the receiver. The molecular weight of the PMA-PVS used was 1500-3000 g/mol, the functional groups were randomly distributed along the polymer backbone and had a 1:1 ratio. The concentrations investigated were 0.02, 0.03, 0.04 and 0.05 ppm ($\mu\text{g/ml}$). The active group ($-\text{COOH}$ and $-\text{SO}_3\text{H}$) concentration is then about $4 \cdot 10^{-7}$ M, much smaller than the Ba^{2+} concentration of $2.5 \cdot 10^{-4}$ M. About two hours after the start of the precipitation, the reactor contents were filtered using a Gelman $0.45 \mu\text{m}$ membrane filter in order to make scanning electron microscope photographs of the residues.

7.3.2 Modeling of the population balance

The population balance equation was written in terms of the moments of the distribution and was calculated in the spreadsheet program Microsoft Excel™ 5.0. The integration of the equations (7.19) was done numerically by multiplying $dm_j(t)/dt$ by time increment Δt and by adding it to $m_j(t-\Delta t)$. Δt was taken as 5 or 10 s and decreasing it to 1 s did not change the result. The supersaturation S was calculated by subtracting the precipitated moles per volume, calculated from m_3 , from the value for S at $t = 0$. The solver option in Excel was used to obtain the pre-exponential factors k_J and k_G (in blank experiment), and the number density of active centers N_{3D} and $N_s/N_{\alpha,2D}$ (in the experiments with PMA-PVS) by using least square fitting procedures.

7.4 Results

Fig. 7.5 shows the results of the conductivity measurements. The conductivities have been converted into concentrations with eq. (7.6) and these were used to obtain the supersaturation (eq. 7.7). Fig. 7.5 shows that the supersaturation decreases according to a reversed S-curve. In the first 100 seconds, the supersaturation decreases slowly. Although nucleation is rapid at this stage (high supersaturation), hardly any surface is available for crystal growth. After approximately 100 seconds,

more crystal surface has been formed, and the supersaturation decreases rapidly because barium and sulfate ions are consumed due to the growth of the crystals. The curves become flatter after about 600 seconds, because at this point the supersaturation has dropped too much for rapid growth and nucleation. PMA-PVS at concentrations above 0.02 ppm slows down the decrease of the supersaturation.

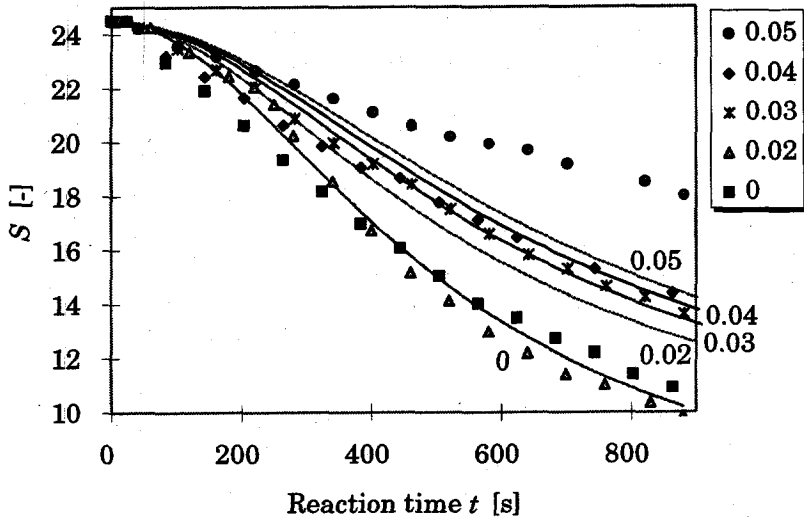


Fig. 7.5. Supersaturation as function of the reaction time. The legend shows the PMA-PVS concentration in ppm. The initial supersaturation was 24.5 in each case. The lines are fits, which reveal that the model describing the influence of PMA-PVS is not very good.

Fig. 7.6 gives the measured autocorrelation functions for two of the five experiments, together with the calculated ACFs. Already after 20 seconds significant particle growth has taken place. The line through the silica ACF is a forced bimodal fit. It deviates from a straight line due to dust and polydispersity.

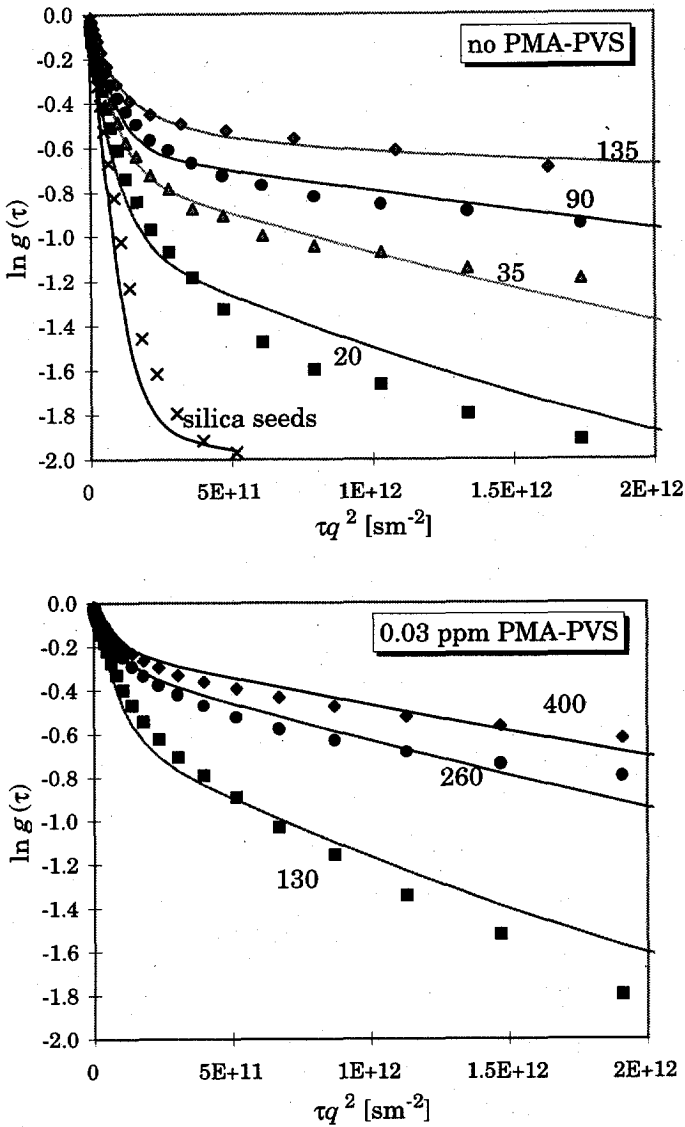


Fig 7.6. Measured (points) and calculated (lines) autocorrelation functions using the population balance model, against τq^2 . The numbers denote the reaction time in seconds.

At zero and very low PMA-PVS concentration, most particles have the form of platelets, as can be seen in fig. 7.7. The particles are not monodisperse. Their length is approximately 3 to 6 μm , their width 2 to 4 μm and their thickness only several hundreds of nm.



Fig. 7.7. SEM photograph of the crystals which have been filtered with a 0.45 μm membrane filter, about 1 hour after the start of the reaction. On the upper photograph, the PMA-PVS concentration was 0.02 ppm and on the lower one 0.04 ppm. For both, the starting supersaturation was 24.5. The particles with no or very small amounts of PMA-PVS have the form of platelets.

7.5 Discussion

In table 7.1, the parameters are given which have been used in the model, together with the results obtained from this work. Because the pH in the experiments described here was 8.0⁴⁾, whereas the pH was only 3.6 in the experiments of Van der Leeden (1991), it was expected that some parameters would differ in the kinetic

⁴⁾ The silica colloid dispersion agglomerates in acidic conditions.

model used here. It was assumed that this was not the case for the interfacial energies and the Langmuir coverage constants, since - in a first approximation - PMA-PVS does not change very much in nature as a function of pH. However, since more groups on the chains of PMA-PVS become deprotonated if the pH is increased, its number of active centers increases.

Furthermore, it was assumed that for heterogeneous nucleation on silica seeds, the same value for the interfacial tension holds as on glass or on inorganic (quartz) dust particles. Heterogeneous nucleation on such surfaces probably occurred in the experiments of Van der Leeden (1991). Therefore, the same value for the interfacial energy as she found was used in the model described here.

Table 7.1. Parameters used for the model calculations for barium sulfate precipitation. Data are obtained from Van der Leeden (1991) except for the data which are marked with an asterisk. These have been found by fitting the model to the measured conductivity data and the autocorrelation functions using a least square model. Between the brackets () the values found by Van der Leeden (1991) are given for comparison.

σ [mJ m ⁻²]	40	k_J [m ⁻³ s ⁻¹]	1.3·10 ⁹ * (7·10 ⁷ -8·10 ¹²)
κ [pJ m ⁻²]	40	k_G [ms ⁻¹]	2.6·10 ⁻⁸ * (4·10 ⁻¹¹ -3·10 ⁻⁹)
σ_a [mJ m ⁻²]	50	N_{3D} [ppm]	3.5·10 ⁻⁵ * (4.4·10 ⁻⁵)
κ_a [pJ m ⁻²]	49	$N_s/N_{a,2D}$	1.1·10 ⁴ * (3.2·10 ⁴)
k_0 [ppm ⁻¹]	550	k_s [ppm ⁻¹]	4500
B_{3D} [-]	28	β_{2D} [-]	π
B_{2D} [-]	29	β_{3D} [-]	16 $\pi/3$
$B_{a,3D}$ [-]	56	T [K]	298
$B_{a,2D}$ [-]	43	K_{eq} [M ²]	1.02·10 ⁻¹⁰
V_m [m ³]	8.61·10 ⁻²⁹	A [cm ² S mol ⁻¹ M ^{-1/2}]	242.2
A_m [m ²]	9.43·10 ⁻¹⁹	B [M ^{-1/2}]	3.53
ρ [kg m ⁻³]	4500	Λ_0 [cm ² Smol ⁻¹]	287.2
L_0 [m]	5·10 ⁻¹⁰	η [Pa s]	8.904·10 ⁻⁴

The data obtained at a PMA-PVS concentration of 0.03 ppm were used to fit the saturation curves and the diameter data to the model in order to find the values of N_{3D} and $N_s/N_{a,2D}$. In principle, the model calculations with the values thus obtained for N_{3D} and $N_s/N_{a,2D}$ should follow the experimental curves for the other concentrations.

In order to compare the model crystal size with the PCS diameter the intensity weighted average particle size should be calculated from the moments in the kinetic model. As has been previously explained, it is extremely difficult to do this exactly. Thus the PCS average diameter was estimated by dividing the fourth moment of the distribution by its third moment. In the Mie regime (approximately 100-10000 nm) this appears to be plausible, as was shown by Finsy and De Jaeger (1991). The alternative, the fifth moment over the fourth, results in about 10 percent higher values for the estimated PCS diameters. The peaks in the scattered intensity as function of the diameter (fig. 7.1) are less profound if a polydisperse size distribution is considered, as was the case here.

The moments of the model calculations were used to calculate the autocorrelation functions. The equation used for this is Koppel's cumulant method equation (eq. 3.16). The first cumulant was obtained from the fourth moment over the third

moment $\frac{m_4}{m_3}$, and the second cumulant from $\sqrt{\frac{m_5 m_3}{m_4^2 - 1}}$.

The values for the seed fraction F were found by adding the seed contribution to the crystal autocorrelation function,

$$g(\tau) = F \exp(-\Gamma_{seeds}\tau) + (1-F) \exp(-\bar{\Gamma}_{crystals}\tau) \exp\left(\frac{\mu_{2,crystals}}{2} \tau^2\right). \quad (7.20)$$

See subsection 3.3.1 for further explanation of this equation.

The pre-exponential factors k_J and k_G (in blank experiment), and the number density of active centers N_{3D} and $N_s/N_{a,2D}$ (in the experiments with PMA-PVS) were found by a combined least square fitting procedure of the model ACFs and model conductivities to the measured ACFs and measured conductivities. The parameter which describes the intensity weighted fraction of seeds F was also obtained by using the least square fitting procedure. The results are shown in the tables 7.1 and 7.2. The seed fraction F decreases at increasing reaction time because the number of crystals increase, but, more important, because large crystals generally scatter more light than smaller ones (fig. 7.1).

Table 7.2. Intensity weighted fraction of seeds F as function of the reaction time.

time [s]	F	time [s]	F
no additive		0.03 ppm	
20	0.64	130	0.45
35	0.51	260	0.25
90	0.46	400	0.19
115	0.36		

Fig 7.8 reveals that particle formation and growth takes place almost immediately after mixing the reactants. If PMA-PVS is added, the particles reach smaller maximum sizes, which is an indication that more critical clusters are formed. The order of magnitude of the PCS-sizes is reasonably good, as can be seen from the SEM photographs (fig. 7.7), if one realizes that in a PCS experiment the sizes in the three directions are averaged. At higher additive concentration, more compact particles are formed, probably due to a change in the growth mechanism. This was not taken into account in the model, and although the subject is very interesting, it lies beyond the scope of this project. However, the change of crystal shape can implicitly be hidden in the value for the interfacial energy.

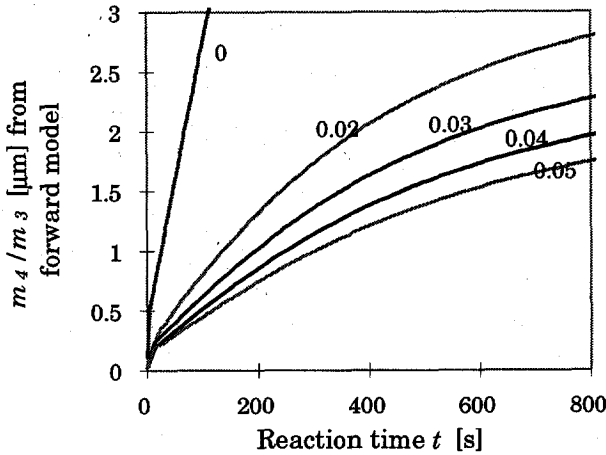


Fig. 7.8. Fourth moment over third moment of the crystal size distribution, obtained by the model shown in fig. 7.3.

After 135 (no PMA-PVS) to 300 (0.03 ppm PMA-PVS) seconds, no reliable PCS measurements can be made anymore. This can be understood from the particle sizes which are found from the model. At that point the crystals exceed the size at which the theory behind PCS is still valid, which is approximately $1.5 \mu\text{m}$ (De Jaeger et al. 1991). In addition, settling of the crystals, which have a high density (4500 kg m^{-3}), influences the autocorrelation function more and more at increasing size.

Fig. 7.9 shows the nucleation rate and the growth rate calculated with the data found from the least square fits, shown in table 7.1. At the concentrations investigated, the additive enhances nucleation, but it retards the growth of the crystals which have formed, as can be seen from fig. 7.9. Therefore, in principle, the crystal size distribution can be controlled by adding the right amount of PMA-PVS. However, at concentrations of approximately 0.05 ppm and higher, the crystallization process takes place rather slowly due to the growth retardation.

The process model predicts the particle size and the supersaturation relatively well. However, the effect of PMA-PVS is stronger than predicted by the model. This can be explained by the fact that in all four experiments the fractional surface and step coverage constant θ with PMA-PVS exceeds 0.85, as can be found from filling in the values for k_s and k_0 in eq. (7.11). Thus, according to the model, a small increase in PMA-PVS concentration does not affect the surface coverage considerably. This suggests that either the values for k_s and k_0 are inaccurate, or that the Langmuir model is insufficient to describe the additive adsorption.

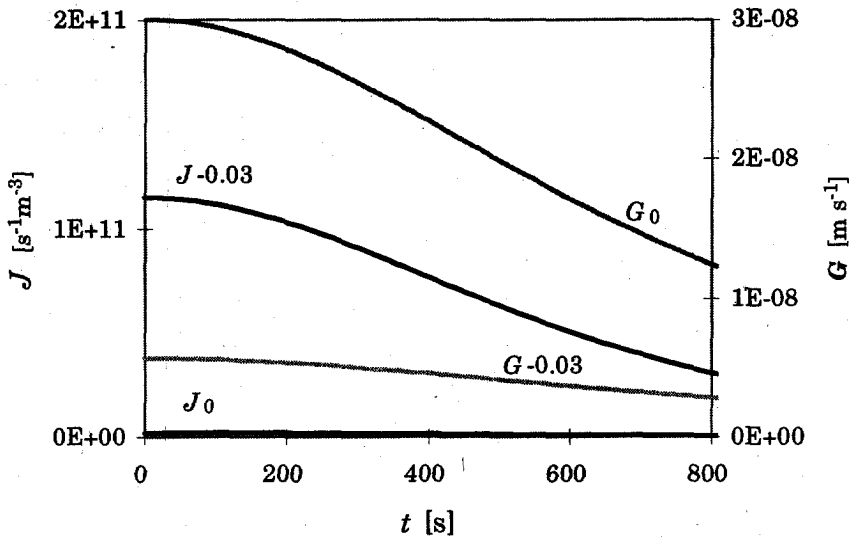


Fig 7.9. Nucleation rates J (left axis) and growth rates G (right axis) for the precipitation experiments with S_0 is 24.5, without PMA-PVS and with 0.03 ppm PMA-PVS, according to the model calculations. Clearly, the nucleation rate is increased and the growth rate is decreased by the presence of the additive.

In absence of additives, the nucleation rate was found to be, $J = 1.3 \cdot 10^{10} \exp(-27/\ln^2 S) [\text{m}^{-3}\text{s}^{-1}]$, while the growth rate was $G = 2.6 \cdot 10^{-8} (S-1)^{2/3} S^{1/3} \exp(-29/3 \ln S) [\text{m s}^{-1}]$. This is in good agreement with the expressions found from induction time measurements by Van der Leeden (1991).

7.6 Conventional analysis methods

In order to compare the alternative analysis method described above with standard procedures, three options were investigated. The first was CONTIN, the method which performs a least square fit in combination with the parsimony principle, as has been discussed in section 3.3.2. It was found that for the bimodal samples, no reproducible and consistent results were obtained. Sometimes, only one modal was resolved, and often the crystal size appeared to decrease, while it should increase.

The second method was a forced bimodal fit. With this method the autocorrelation functions were analyzed by fitting them to,

$$g(\tau) = F \exp(-D_1 q^2 \tau) + (1 - F) \exp(-D_2 q^2 \tau). \quad (7.21)$$

The result was that often only one modal resulted and that the position of the fraction of small particles is closely related to the seed fraction F . Hence, if a small seed diameter was found, its fraction appeared relatively small as well. Therefore, a third option was tried, namely a forced fit to,

$$g(\tau) = F \exp(-D_{seeds} q^2 \tau) + (1 - F) \exp(-D_{crystals} q^2 \tau). \quad (7.22)$$

Since the seed diffusion coefficient was known, only F and the average crystal diffusion coefficient $D_{crystal}$ were needed to be fitted, resulting in more consistent and

reliable results. The results are shown in fig. 7.10. The lines in the figure are obtained by feeding the from $D_{crystal}$ derived crystal diameters into the kinetic model together with the conductivity results. Clearly, particle growth can be observed, but the particle size does not appear to increase monotonously, as is expected. The kinetic parameters obtained (k_J , k_G , N_{3D} and $N_s/N_{a,2D}$) were of the same order of magnitude as found from the 'observer' method, but the resulting particle sizes are larger, as can be seen from comparing fig. 7.10 with fig. 7.8. The fit quality, which can be quantified by calculating the residuals from the measured and calculated autocorrelation functions, was worse for the bimodal fit procedure.

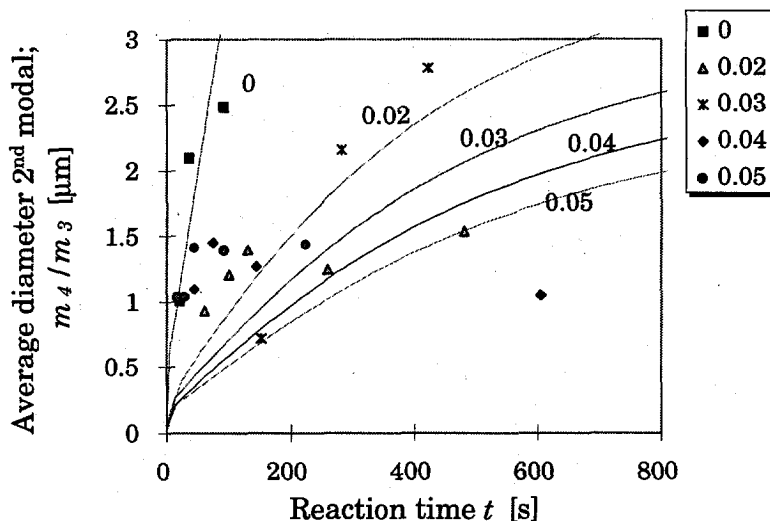


Fig. 7.10. Diameters of the precipitated crystals as found from the bimodal fits to the autocorrelation functions (eq. 7.22) (points) and the model calculations obtained by using these diameters (lines).

The forward approach has the advantage that more reliable results are obtained compared to standard PCS analysis techniques, because extra information is used. In addition, more data are available to perform a least square fit, i.e. the number of channels chosen in the correlator instead of the few parameters found from alternative analysis methods.

The drawbacks of the forward approach is that a reliable model which accurately describes the kinetics of the process is needed and that the calculations to find the required parameters, i.e. reaction rate constants, are rather elaborate since many data points are involved. Typically, every two minutes one autocorrelation function can be obtained from a process, which contains 25 to 200 data points (channels).

7.7 Conclusions

Batch crystallization experiments of barium sulfate with the addition of the polyelectrolyte PMA-PVS were followed by photon correlation spectroscopy in combination with conductivity measurements. The ill-conditioned and (therefore) noise-sensitive inversion of the ACF was not required, because the autocorrelation functions were directly fed into a process model and not the from the inversion ob-

tained derived particle sizes. By adding foreign seeds, reproducible results were guaranteed.

Analysis of the measured raw data in combination with the relatively simple population balance process model revealed the kinetics of barium sulfate precipitation quite well. It was found that the precipitation can be described by a (heterogeneous) nucleation / growth model, where the growth rate is determined by two dimensional surface nucleation. The nucleation rate was found to be, $J = 1.3 \cdot 10^{10} \exp(-27/\ln^2 S) [\text{m}^{-3}\text{s}^{-1}]$, while the growth rate was $G = 2.6 \cdot 10^{-8} (S-1)^{2/3} S^{1/3} \exp(-29/3\ln S) [\text{ms}^{-1}]$. This is in good agreement with the expressions found from induction time measurements by Van der Leeden (1991).

At 0.02 ppm PMA-PVS has already a large influence on the crystallization kinetics, probably due to interactions with the crystal surface. However, a Langmuir adsorption model to quantify these interactions does not appear to describe the kinetics in the presence of PMA-PVS very accurately. This is attributed to changes in the crystal shape as a result of interactions with the additive. At the concentrations investigated, the additive enhances nucleation, but it retards the growth of the crystals that have formed. Therefore, in principle, the crystal size distribution can be controlled by adding the right amount of PMA-PVS.

References

- M. Angerhöfer (1993) *Untersuchungen zur Kinetik der Fällungskristallisation von Bariumsulfat*, Ph.D. thesis, Technische Universität München, München.
- P.W. Atkins (1986) *Physical chemistry*, Oxford University Press, Oxford.
- A. Boxman, A. Haket and P.J.T. Verheijen (1992) *MieSu* computer program (test routine for Roma, see A. Boxman (1992) *Particle Size Measurement for the Control of Industrial Crystallizers*, Ph.D. thesis Delft University of Technology).
- R. Eek (1995) *Control and Dynamic Modeling of Industrial Suspension Crystallizers*, Ph.D. thesis Delft University of Technology.
- N. de Jaeger, H. Demeyere, R. Finsy, R. Sneyers, J. Vanderdeelen, P. van der Meer, M. van Laethem (1991) Particle sizing by Photon Correlation Spectroscopy. Part I: Monodisperse Lattices: Influence of Scattering Angle and Concentration of Dispersed Material, *Part. Part. Syst. Charact.* **8** 179-186.
- R. Finsy and N. de Jaeger (1991) Particle Sizing by Photon Correlation Spectroscopy. Part II: Average Values, *Part. Part. Syst. Charact.*, **8**, 187-193.
- M.C. van der Leeden (1991) *The Role of Polyelectrolytes in Barium Sulphate Precipitation*, Ph.D. thesis, Delft University of Technology, Delft. Relevant chapters have been published as: M.C. van der Leeden, D. Kashchiev, G.M. van Rosmalen (1992) Precipitation of Barium Sulphate: Induction Time and the Effect of an Additive on Nucleation and Growth. *J. Coll. Interface Sci.* **152**, 338-350, and M.C. van der Leeden, D. Kashchiev, G.M. van Rosmalen (1993) Effect of Additives on Nucleation Rate, Crystal Growth Rate and Induction Time in Precipitation, *J. Crystal Growth* **130** (1993) 221-232.
- M.C. van der Leeden (1994) Personal communication.
- A.D. Randolph and M.A. Larson (1971) *Theory of Particulate Processes*, Academic Press, New York.
- R.A. Robinson and R.H. Stokes (1959) *Electrolyte Solutions; The Measurement and Interpretation of Conductance, Chemical Potential and Diffusion in Solutions of Simple Electrolytes*, 2nd ed., Butterworths, London, 136-143.
- S. de Wolf (1990) Modelling, System Identification and Control of an Evaporative Continuous Crystallizer, Ph.D. thesis, Delft University of Technology, Delft.

Symbol list

<i>a</i>	activity	[mol m ⁻³]
<i>a</i>	acceleration	[m s ⁻²]
<i>A</i>	constant in DHO equation (Ch. 7)	[S m ^{-5.5} mol ^{0.5}]
<i>A</i>	surface area	[m ²]
<i>A</i>	optical constant (Ch. 3)	[-]
<i>A₀</i>	monomer surface area	[m ²]
<i>A_m</i>	monomer surface	m ²
<i>A_s</i>	fused spherical aggregate surface	[m ²]
<i>b</i>	scattering amplitude (Ch. 3)	[a.u.]
<i>b</i>	backward transition frequency	[s ⁻¹]
<i>B</i>	constant in DHO equation	[m ^{-1.5} mol ^{0.5}]
<i>B_{nD}</i>	exponential term in rate expression	-
<i>c</i>	concentration	[ppm (=mg kg ⁻¹), mol m ⁻³]
<i>c</i>	particle mean thermal velocity	[m s ⁻¹]
<i>C</i>	concentration	[mol m ⁻³ , g g ⁻¹]
<i>d</i>	diameter	[m, nm]
<i>d_p</i>	primary particle size	[m]
<i>D</i>	diffusion coefficient	[m ² s ⁻¹]
<i>D_f</i>	mass fractal dimension	[-]
<i>e</i>	elementary charge unit	[C]
<i>E</i>	electric field	[a.u.]
<i>f</i>	forward transition frequency	[s ⁻¹]
<i>F</i>	Faraday constant (Ch. 7)	[C mol ⁻¹]
<i>g</i>	normalized field autocorrelation function	[-]
<i>G</i>	measured autocorrelation function	[-]
<i>G</i>	Gibbs free energy (Ch. 2)	[J]
<i>G</i>	growth rate	[m s ⁻¹]
<i>h</i>	distance from heart of IR laser	[mm]
<i>H</i>	distance from nozzle	[mm]
<i>I</i>	intensity	[a.u.]
<i>J</i>	nucleation rate	[s ⁻¹ m ⁻³ or mol m ⁻³ s ⁻¹]
<i>k</i>	Boltzmann's constant	[J K ⁻¹]
<i>k_i</i>	reaction rate constant	
<i>k_d</i>	slope in <i>D</i> vs ϕ plot	[-]
<i>k_G</i>	growth rate constant	[m s ⁻¹]
<i>k_J</i>	nucleation rate constant	[s ⁻¹ m ⁻³]
<i>K</i>	equilibrium constant	
<i>K</i>	Kohlrausch's constant (Ch. 7)	[S m ^{-5.5} mol ^{0.5}]
<i>l</i>	number of ions in molecule	[-]
<i>l</i>	particle mean free path (Ch. 5)	[m]
<i>m_j</i>	<i>j</i> th moment of the size distribution	[m ^j m ⁻³]
<i>M</i>	molar mass	[kg mol ⁻¹]
<i>n</i>	number of units	[-]
<i>n</i>	refractive index (Ch. 3)	[-]
<i>N</i>	total number of units, vacancies	[-]
<i>N'</i>	number concentration	[kg ⁻¹]
<i>P</i>	probability density function	[-]

116 *Measurement and modeling of cluster formation*

<i>P.I.</i>	polydispersity index	[-]
<i>q</i>	constant (Ch. 7)	[-]
<i>q</i>	length of scattering vector	[m ⁻¹]
<i>r</i>	space coordinate (Ch. 3)	[m]
<i>r</i>	radius	[m]
<i>r_c</i>	collision radius	[m]
<i>r_p</i>	particle radius	[m]
<i>R</i>	radius in Young equation (Ch. 2)	[m]
<i>R</i>	gas constant	[J mol ⁻¹ K ⁻¹]
<i>S</i>	dynamic structure factor (Ch. 3)	[-]
<i>S</i>	supersaturation (=C/C _{eq})	[-]
<i>t</i>	time	[s]
<i>T</i>	temperature	[K, °C]
<i>v</i>	velocity	[m s ⁻¹]
<i>V</i>	volume	[m ³]
<i>V₀</i>	monomer volume	[m ³]
<i>w</i>	beam waist radius	[m]
<i>x</i>	average distance between particles	[m]
<i>Y</i>	flow autocorrelation function (Ch. 3,4)	[-]
<i>Y</i>	normalized number distribution	[-]
<i>z</i>	charge on ion	[-]
<i>Z</i>	number distribution function	[-]

Greek

α	degree of dissociation	[-]
α	attraction parameter (Ch. 4)	[-]
β	collision frequency function (Ch. 5)	[m ³ s ⁻¹]
β	repulsion parameter (Ch. 4)	[-]
β	shape factor	[-]
δ	number of ions in formula unit	[-]
ϵ	electrical permeability (Ch. 7)	[F m ⁻¹]
ϕ	interfacial energy	[J]
Φ	diffusing unit volume	[m ³]
γ	surface Energy	[J m ⁻²]
Γ	decay constant	[s ⁻¹]
η	viscosity	[Pa s]
φ	divergence angle	[rad]
φ	volume fraction (Ch. 4)	[-]
κ	specific edge free energy	[J m ⁻¹]
κ	transition parameter	[m ⁻¹]
κ_e	conductivity	[S m ⁻¹]
λ	wavelength	[m]
Λ	molar conductivity	[S m ⁻⁴ mol]
μ	chemical potential	[J]
μ	cumulant (Ch. 3)	[s ⁻¹]
μ	linear attenuation factor (Ch. 4)	[m ⁻¹]

Π	ion activity product	$[\text{mol}^{\delta}\text{m}^{-3\delta}]$
θ	contact angle (Ch. 2)	[rad]
θ	fractional surface coverage (Ch. 7)	[-]
θ	scattering angle	[rad]
ρ	density	$[\text{kg m}^{-3}]$
σ	specific surface free energy	$[\text{J m}^{-2}]$
Σ	macroscopic scattering cross section	[m]
τ	delay time	[s]
τ_s	characteristic sintering time	[s]
Ω	solid angle	[rad]
ψ	Young function	[-]
ζ	gas mean free path	[m]

subscript

0	infinite dilution, in vacuum
<i>ads</i>	adsorbed on surface
<i>c</i>	crystal
<i>eq</i>	equilibrium
<i>f</i>	final
<i>i</i>	initial, number label
<i>k</i>	crystal face
<i>m</i>	molecular or monomer
<i>s</i>	solvated

superscript

<i>crit</i>	critical
*	reference state

Samenvatting

Het meten en modelleren van clustervorming

Michiel van Drunen

Inleiding

Dit proefschrift behandelt de vorming van clusters (min of meer geordende groeperingen) van moleculen die ontstaan in waterige oplossingen. Deze clusters kunnen voorstadië zijn van kristallen, en worden dan ook wel kiemen of nucleï genoemd. Ook is gekeken naar de vorming van een keramisch materiaal, siliciumnitride, direct uit de gasfase. Deze verschijnselen, die niet alleen interessante natuurlijke verschijnselen zijn, maar ook van groot belang zijn in veel chemische industriële processen, zoals de produktie van kunstmest en fotografische materialen, zijn bestudeerd vanuit het vakgebied van deeltjestehnologie. Hierin speelt de karakterisering van een deeltjes een belangrijke rol. De deeltjes die zijn bestudeerd zijn tussen ongeveer een miljardste (enkele moleculen) en een miljoenste meter groot.

Het doel van dit werk was tweeledig. Ten eerste wilde ik meer te weten komen over het verschijnsel kiemvorming zelf. Ten tweede is het voor het regelen en controleren van industriële processen van groot belang dat er betrouwbare en nuttige gegevens over dit proces worden gemeten. In dit proefschrift is gekeken of dit mogelijk is bij de zeer kleine deeltjes die karakteristiek zijn in kiemvormingsprocessen.

Kiemvormingstheorie

Na de introductie opent dit proefschrift met een theoretische verhandeling over de vorming van clusters (*hoofdstuk 2*). Kristalvorming gebeurt in twee stappen. In de eerste stap worden kiemen gevormd die in de tweede stap kunnen uitgroeien tot kristallen. De kiemvormingsnelheid wordt uitgedrukt in aantallen kiemen die per volume per tijdseenheid ontstaan. De theorieën die de kiemvormingsnelheid voorspellen zijn al in het begin van deze eeuw ontwikkeld en sindsdien op slechts kleine punten verbeterd. Het hoofdstuk laat zien dat de behandelde theorieën voor het getoonde voorbeeld slechts kleine verschillen opleveren. Helaas is het zeer moeilijk de grootheden die verschillen experimenteel te bepalen, waardoor het niet goed mogelijk is aan te wijzen welke theorie de beste is. Het ligt dan ook voor de hand in de praktijk de eenvoudigste theorie te gebruiken.

Metten met lichtverstrooiing

Hoofdstuk 3 behandelt de meettechniek die is gebruikt in vrijwel alle andere hoofdstukken. Met deze techniek, fotoncorrelatiespectroscopie (PCS), worden de fluctuaties gemeten in de verstrooide lichtintensiteit van een monster met daarin zwevende deeltjes. Deze fluctuaties ontstaan doordat kleine deeltjes in gassen of vloeistoffen niet stil staan, maar voortdurend in willekeurige richtingen bewegen ten gevolge van botsingen met omringende gas- of vloeistofmoleculen. Grofweg komt het erop neer dat de lichtintensiteit verstrooid door kleine deeltjes sneller fluctueert in de tijd dan dat van grote deeltjes. Een PCS meetopstelling is geen zwarte doos waar absolute deeltjesgrootteverdelingen uit komen na een meting, maar vereist nogal

wat kennis van de natuurkunde achter de meettechniek én van de eigenschappen van het monster. Gelukkig is bij de meeste te meten monsters vrij veel bekend over de concentratie, de vorm van de deeltjes en dergelijke. In hoofdstuk 3 wordt de natuurkunde achter PCS beschreven. Grote voordelen van PCS zijn dat een uitgebreide monstervoorbereiding niet nodig is, dat geen ijking nodig is, dat het monster niet wordt vernietigd, dat een meting in goede omstandigheden maar een minuut hoeft te duren en dat het mogelijk is direct te meten in een proces (in-line) of in een aftakking uit een proces (on-line).

Clusters in geconcentreerde oplossingen

Hoofdstuk 4 is gewijd aan de vorming van clusters in geconcentreerde oplossingen. Door metingen met PCS te doen in oplossingen van citroenzuur, sucrose (bietsuiker) en kaliumnitraat (een component in kunstmest) bij verschillende concentraties is aangetoond dat bij de eerste twee stoffen er zeer waarschijnlijk clusters worden gevormd die enkele moleculen groot zijn. Ze worden groter bij toenemende concentratie. Waarschijnlijk vormen deze clusters geen voorstadia van kristallen, maar een toestand tussen de opgeloste en de kristallijne fase in. Opvallend is dat de cluster grootte van sucrose en citroenzuur ongeveer gelijk is. De oorzaak hiervoor kan zijn dat clusters niet ontstaan door aantrekkingskrachten tussen de opgeloste moleculen, maar doordat het water de opgeloste moleculen als het ware op elkaar drukt teneinde zoveel mogelijk contacten met ander watermoleculen te kunnen blijven onderhouden. Kalium- en nitraationen zijn zo klein dat het water daar niet zoveel last van heeft. Met neutronenverstrooiingsexperimenten die zijn gedaan bij de kernreactor van de TU Delft (IRI) zijn de resultaten van de PCS-metingen kwalitatief bevestigd.

Homogene nucleatie

In *hoofdstuk 5* is de agglomeratie (samenklontering) van deeltjes in een aërosolreactor gevolgd met PCS. Een aërosol is een suspensie van deeltjes of druppeltjes in een gas en in een aërosolreactor worden dus deeltjes gemaakt uit ingevoerde gasstromen. Het proces is een voorbeeld van homogene nucleatie, kiemvorming direct uit de bulk zonder tussenkomst van andere oppervlakken. In de reactor werd het keramische materiaal siliciumnitride gemaakt door twee gassen, ammoniak en silaan, te verhitten met een sterke laserstraal. Hierdoor vallen ze uit elkaar en er ontstaan deeltjes direct uit de gasfase, die groeien doordat ze met elkaar botsen en een verbinding maken. Met PCS werden de deeltjesgrootte en de snelheid waarmee de vlam de deeltjes mee naar boven sleurt, bepaald en vergeleken met modelwaarden. Het bleek dat het goed mogelijk is met een relatief eenvoudige opstelling in-line het proces te volgen.

Hoofdstuk 6 is een voorstudie voor hoofdstuk 7. Beide hoofdstukken beschrijven nucleatie uit oplossingen, maar het proces in hoofdstuk 6 is beter controleerbaar en preciezer te meten met PCS, vooral omdat het langzamer verloopt. Het betreft neerslag van zwavel uit een aangezuurde thiosulfaatoplossing. Ook hier vindt de kiemvorming homogeen plaats. De groeisnelheid wordt, net als in hoofdstuk 5, niet bepaald door de nucleatie of de groei, maar door de snelheid waarmee de monomeren, zwavelmoleculen, worden gevormd. De gemeten reactiesnelheid komt goed overeen met de literatuurwaarde, die is verkregen met een totaal andere meettechniek. De waargenomen inductietijd, een tijdsduur waarin geen deeltjes

kunnen worden gemeten terwijl de reactie al wel is gestart, strookt met het in de literatuur gesuggereerde reactiemechanisme.

Heterogene nucleatie

In *hoofdstuk 7* zijn metingen en modelberekeningen van neerslag van bariumsulfaat uit waterige oplossingen beschreven. Bariumsulfaat is slecht oplosbaar en bij de bestudeerde, relatief lage, concentraties was ook de oververzadiging nog zo laag dat de kiemvorming uitsluitend plaats vindt op bestaande oppervlakken. Om dit proces te sturen zijn zeer kleine silica- (een soort zand) deeltjes toegevoegd aan het reactievatje. De nucleatie- en groeisnelheden van bariumsulfaat zijn goed bekend en ook het gedrag van enkele additieven is goed beschreven in de literatuur. Het was mogelijk om met PCS de kristalgroei te volgen. Met het nucleatie/groeimodel zijn de ruwe data verkregen met PCS, de autocorrelatiefuncties, te berekenen. Door nu deze berekende functies te vergelijken met de gemeten functies en de modelparameters zo aan te passen dat de functies zo goed mogelijk samenvallen was het mogelijk de groei- en kiemvormingsnelheidsconstanten te bepalen. Het voordeel van deze methode is dat de conversie van de autocorrelatiefuncties naar deeltjesgrootteverdelingen, die extreem gevoelig is voor altijd aanwezige ruis, wordt omzeild.

Nawoord

Niets vindt plaats in een vacuum, en het bedrijven van wetenschap is daarop zeker geen uitzondering. Daarom wil ik allereerst alle mensen bedanken die mij wegwijs hebben gemaakt in de werelden van de deeltjestechnologie en van de kristallisatie, vooral Brian Scarlett, Gerda van Rosmalen, Henk Merkus, Robert Finsy, Sotiris Pratsinis, Bruce Weiner, het Uniak-team en met name Ruari en Camiel, Dimo Kashchiev, Mieke van der Leeden en Kevin Roberts.

Mijn promotoren bedank ik voor hun vertrouwen in mij, voor hun ideeën voor voortgang en voor hun altijd bruikbare lijst met mensen die nog meer deskundigheid hebben. Henk stond altijd klaar met adviezen als ik hem daarom vroeg. Ik bedank hem en Gerda voor hun analytische visie en hun nauwkeurige leeswerk.

Mariëlle en Nils hebben als afstudeerders belangrijke bijdragen geleverd aan de hoofdstukken 2 en 7, en 3. Helaas was Nils' programmeerwerk nog niet goed bruikbaar. Ik bedank Mariëlle voor haar nauwkeurigheid en vasthoudendheid waarmee ze haar experimenten heeft uitgevoerd en voor haar positieve bijdrage aan de sfeer in de groep. Researchpracticanten Jolanda en Marco hebben een voorzet gegeven voor de geleidbaarheidsmetingen van hoofdstuk 7. Verder dank ik Jan Marijnissen voor zijn bijdragen aan hoofdstuk 5 en zijn niet-aflatende enthousiasme voor aerosoltechnologie. Met Ilse heb ik de experimenten die staan beschreven in hoofdstuk 5, uitgevoerd. We waren een prima team. Ad van Well heeft mij wegwijs gemaakt op het gebied van neutronenverstrooiing en de metingen in hoofdstuk 4 gedaan. Bedankt daarvoor. Ik dank ook Peter Verheijen, Arthur Boxman en Arno Haket voor het geven van hun uitstekende Mieprogramma.

Jeff Grace, Helen O'Keane, Brian Scarlett en vooral Sjef Schoorl hebben ervoor gezorgd dat het Engels in dit proefschrift van een aanvaardbaar niveau is geworden. Yvette bedank ik, omdat ze mij heeft leren schrijven op een manier die toegankelijk en aangenaam is voor een groot publiek. Hopelijk is de Nederlandse samenvatting hiervan een voorbeeld.

De 'oude garde' van Deeltjestechnologie, voor mij waren dat met name Olaf, Gabriele, Paul en Lex, wil ik bedanken, omdat ze mij inzicht gaven in de bureaucratie van de vakgroep en in de chemische technologie in het algemeen, maar vooral voor de gezelligheid en de sfeer binnen de groep. Vooral aan de koffietafelsessies, de (vele) conferenties, de deeltjesdiners en -borrels heb ik veel plezierige herinneringen. Marcel, Damien, Martin, Frank, Alexander, Arief, Rob, Wim, Ilse, Krijn-Jan, Hans en de andere deeltjes-Aio's nemen nu de fakkel over.

Het Aio-schap omvat meer dan alleen wetenschappelijk onderzoek. Door Yvette heb ik mijn schrijftalent kunnen ontwikkelen en Saul heeft mijn interesse voor het milieu uitgebreid richting duurzaamheid en techniekfilosofie. Door mee te doen aan 'zijn' Chemie en Samenleving heb ik veel inzicht gekregen in hoe De Wereld in elkaar steekt.

Met Hans heb ik vele aangename uren filosoferend boven glazen Belgisch bier doorgebracht. Helaas waren de aldus verkregen wijsheden de volgende ochtend niet altijd bruikbaar. Jan Remmert dank ik voor de omslagfoto, het lezen van stukken proefschrift en voor zijn vriendschap.

Ten slotte dank ik Stephanie voor haar interesse, geduld, vertrouwen, verraagzaamheid, begrip, maar vooral voor haar liefde.

Curriculum vitae

Michiel van Drunen is geboren op 7 oktober 1967 in Zwijndrecht.

- 1980-1986 Atheneum Openbare Scholengemeenschap Walburg in Zwijndrecht
- 1986-1990 Studie Scheikunde aan de Rijksuniversiteit Leiden, afstudeerrichting Milieuchemie
- 1991-1995 Als Assistent in Opleiding werkzaam bij de sectie Deeltjestechnologie van de vakgroep Chemische Procestechologie, Faculteit Scheikundige Technologie en Materiaalkunde van de Technische Universiteit Delft. Tevens in deeltijd werkzaam als redacteur en verslaggever van het faculteitsblad en als free-lance journalist
- 1996- Projectonderzoeker bij het Instituut voor Milieuvraagstukken van de Vrije Universiteit in Amsterdam

Als das Kind ein Kind war
Wusste es nicht,
Dass es ein Kind war
Alles war ihm beseelt

(uit *Der Himmel über Berlin*, regie Wim Wenders)

